Computational Modeling of Environmentally Relevant Reactions

A DISSERTATION
SUBMITTED TO THE FACULTY OF
UNIVERSITY OF MINNESOTA
BY

STUART WINIKOFF

IN PARTIAL FULFILLMENT OF THE REQUIREMENTS
FOR THE DEGREE OF
DOCTOR OF PHILOSOPHY

Professor Christopher J. Cramer

July 2014

Acknowledgements

There are so many people that have helped me reach this point that I can only begin to thank them all here for their efforts. First of which is the important role that my advisor Chris Cramer has played in providing guidance, encouragement and understanding, and for helping me to develop as an independent researcher. I would also like to thank Laura Gagliardi for allowing me to spend time as part of her research lab, for teaching me so much, and for her continued support the last five years.

Furthermore, I owe a great deal to the chemistry faculty at the University of Minnesota-Twin Cities for all that I have been able to learn and take away from graduate school. I would also like to thank the chemistry faculty and staff at the University of Minnesota-Morris, specifically Jim Togeas, Nancy Carpenter, Ted Pappenfus, Joe Alia, and Julie Kill for laying the foundation of knowledge that has aided me so much, for offering me the opportunity to work with them in the past, and for their continued support after my graduation.

A great deal of thanks also goes to the external collaborators who helped make all of this work possible. Especially to Prof. Jim Mayer and Shoshanna Barnett whose work and correspondence helped lead me through many difficult problems and also to Frances Hill and Manoj Shukla at ERDC, both of whom helped propose interesting research topics and offered guidance along the way.

I cannot forget the role that everyone in the Cramer group, past and present, has played and their help and support, in addition to their willingness to sit down and talk out problems. Thank you Aaron League, Adam Scheidecker, Agnieszka Dybala-Defratyka,

Alek Marenich, Ashley Garr, Busra Dereli, Danny Sadowsky, David Semrouni, Hugo Vazquez, Kelly Daniels, Patrick Donoghue, Pere Miro, Samat Tussupbayev, Soumen Ghosh, Robert Molt, Will Isley, Yunju Zhang, and Zahid Ertem for being there. Specifically I would like to thank Ashley Garr for helping me get started at Minnesota and to Zahid Ertem, Kelly Daniels, Adam Scheidecker and Yunju Zhang for working closely with me on research projects. A great deal of thanks also goes out to everyone I have worked with in the Gagliardi group over the years, as they have provided endless help and been there when I needed them, especially Allison Dzubak, Abdul Shahai, Bess Vlaisavljevich, Chad Hoyer, Drew Koballa, Dongxia Ma, Dylan Evans, Giovanni Li Manni, Ivan Infante, Josh Borycz, Laura Largo, and Nora Planas. A large debt of gratitude is also due to the graduate students in my year who were willing to stay up late and help keep each other sane, especially Allison Dzubak, Drew Koballa, Dylan Evans, and Mackenzie Provorse.

Finally, I would not have made it this far without the support of my family, particularly my parents and grandparents who always encouraged a good work ethic, taught me the art of talking tough problems through, and helped foster a deep love of the sciences. A heartfelt thank you also goes out to my in-laws, Gale and Arlan Winikoff, who have gone above and beyond in offering me help and support during the last few years. Most importantly, I would like to thank my wife Winnie for being my best friend, sounding board, and dearest companion.

Dedication

For

Sarah Winikoff

Abstract

Computational chemistry is a flexible tool that can quantitatively describe the reactivity of a wide variety of systems, ranging from simple organic molecules to complex heterogenous surfaces. In this thesis, quantum chemical methods are employed in both a diagnostic and predictive capacity to gain insight into the reactions of a number of environmentally relevant chemical systems. Chapter 2 outlines the use of multiple theoretical models for the characterization of the dominant conformers of nerve agents found in aqueous solution and for the understanding of their subsequent inactivation via triethylamine-catalyzed hydrolysis. This computational analysis informed the development of a procedure used to assess the ability of several organic complexes to more efficiently catalyze the decomposition of toxic organophosphates into non-toxic products. Chapter 3 describes the use of Density Functional Theory (DFT) to reveal a complete mechanistic pathway for the oxidation of water by a homogenous copper-bicarbonate catalyst. The proposed mechanistic steps were evaluated by the calculation of redox potentials, pK_a values and free energy barriers, which were validated by comparison to experiment. Chapter 4 presents the use of plane-wave periodic DFT to evaluate the details of nitrogen-rich aromatic groups binding to both an aluminum metal surface and two environmentally relevant alumina surfaces. The role that nitrogen substitution on the aromatic ring plays in adsorption on these surfaces was assessed through the analysis of both optimal geometries and computed binding energies.

Table of Contents

List of Tables

List of Figures

List of Abbreviations

CV: Cyclic Voltammetry

DFT: Density Functional Theory

DMMP: O,S-dimethyl methyl phophonethiolate

FCC: Face-Centered Cubic

GGA: Generalized Gradient Approximation

HEC: High-Energy Compound

HF: Hartree-Fock

IRC: Intrinsic Reaction Coordinate

NHE: Normal Hydrogen Electrode

PAW: Projected Augmented Wave

PBE: Perdew-Burke-Ernzhof

PCET: Proton-Coupled Electron Transfer

PES: Potential Energy Surface

PW-DFT: Plane-Wave Density Functional Theory

SCS-MP2: Spin-Component-Scaled Second Order Perturbation Theory

S.P.: Single-Point

TD: Time-Dependent

TEA: Triethylamine

TS: Transition-State

VASP: Vienne *Ab Initio* Simulation Package

Preface

Citations from previously published work in this thesis are as follows:

Chapter 3

Reproduced with permission from:

Winikoff, S. G.; Cramer, C. J. *Catal. Sci. Technol*. **2014**, 4, 2484-2489.

Link: http://xlink.rsc.org/?doi=C4CY00500G

Chapter 1. Introduction

1.1. Overview

Chemists continue to focus on ameliorating the detrimental impacts that the chemical industry can sometimes place on the environment. Thus, much current research has included a focus on reducing the environmental footprint of a wide range of chemical processes through such activities as improving the disposal and remediation of dangerous chemicals, increasing the production of "green" fuels and evaluating the environmental fate of proposed new chemical compounds. Complicating these undertakings, there are often limitations imposed on their experimental realization, including the difficulty of working with dangerous substances or in characterizing chemical reactions that take place under extreme conditions. In an effort to supplement these gaps in chemical understanding, this work focuses on the use of computational chemistry to provide insights into the behavior of a number of poorly understood but environmentally important chemical systems.

1.2. Computational Methods

Computational chemistry contains a wide range of theoretical techniques that are each individually suited to providing certain types of chemical information.[1] The work in this thesis focuses on the use of quantum mechanical methods to provide detailed mechanistic information about chemical reaction pathways through the identification of key stationary points on the Potential Energy Surface (PES), which correspond to local

minima and transition state structures. By analyzing the electronic gradients at each of these points, it is possible to evaluate relative Gibb's free energies, which allows for easy comparison to the experimentally observable equilibrium constants and reaction rates.

1.2.1. Molecular Orbital Theory

A straightforward quantum mechanical computational protocol involves the optimization of the molecular wavefunction, which, for a closed-shell singlet electronic state, for example, is treated as a Slater determinant of the doubly-occupied molecular orbitals. The simplest of these methods is Hartree-Fock (HF) theory, which treats the electron-electron interactions using a mean-field and neglects all electron correlation, resulting in inaccurate results for many chemical systems.[2-6] However, this formalism allows for the inclusion of electron correlation through the use of perturbative methods and provides for a systematic approach to the improvement of the electronic energies through the use of complete basis set methods.[7-10] Unfortunately, these accurate methodologies are accompanied with a significant computational cost and as such are used in this thesis solely to provide a benchmark for the accuracy of the other computational methods.

1.2.2. Density Functional Theory

Density functional theory (DFT) provides an alternative model in which instead of using the molecular orbitals, the electron density of the system is optimized and used to calculate chemical properties, such as Gibb's free energies.[11,12] This formalism has the

benefit of including in the functional itself a term that directly accounts for electron correlation in a manner that allows for greater computational efficiency than is currently available for molecular orbital based methods, since the correlation term is part of the self-consistent-field procedure itself. This combination of accuracy and computational efficiency helped inform the choice to use DFT methods for the majority of the calculations performed in this work.

However, the exact functional form of those terms describing electron correlation and exchange with respect to the electron density of the system remains unknown. As a consequence there is a wide range of density functionals available with each designed under a different set of approximations, the most common of which are the generalized gradient approximation (GGA) and meta-GGA functionals which introduce a dependence upon the first and second derivatives of the electron density into the exchange-correlation functional.[13-20] In addition, the electron exchange term from HF theory can be included into DFT to produce a "hybrid" functional that possesses reduced self-interaction errors, though these methods suffer a penalty in computational efficiency due to the need to calculate four-index electron repulsion integrals and experience suggests that they can moreover lead to inaccurate results for transition-metal containing systems.[21-25] A final class of density functional methods endeavors to improve the description of electron exchange and correlation present in long range interactions through the use of a flexible exchange functional that possesses a dependence on electronic distances or through the addition of empirical terms that depend upon internuclear distances and are designed to account for non-bonded attractive interactions.[26-31] With such a wide range of

approximations available for DFT, comparison to experimental results or high level *ab initio* calculations is important for establishing that a chemical system is well described by a given density functional.

1.2.2.1. Orbital Based Formulism

For molecular systems, it is often useful to construct the electron density of the system from a set of atom-centered basis functions. In chapters 2 and 3, sets of gaussian-type basis functions were used to construct the electron density of the system, with close attention paid to the size of the basis set, in order to balance accuracy and computational cost.[34] To further improve the computational efficiency for these systems, a pseudo-potential was used to describe the core electrons of the metal atoms, which can provide an accurate description of these large atomic centers—including potential relativistic effects—at a reduced cost.[35,36] These atom-centered basis sets allow for a chemically intuitive description of molecular systems in addition to enabling the easy generation of Kohn-Sham orbitals, which are used for hybrid DFT and serve as useful proxies for the real molecular orbitals.

1.2.2.2. Plane-Wave Formalism

However, for large bulk systems with periodic boundary conditions, the computational cost of using atom-centered basis sets can quickly become prohibitive. A more natural choice is to construct the electron density from a basis set composed of plane waves, with an energy cut-off employed to help determine the size of the basis

set.[37,38] The computational cost can be further lowered by describing the atomic core electrons through the use of pseudo-potentials designed for plane-wave based calculations.[39,40] Unfortunately, this formalism can only be applied to periodic systems, but a vacuum space can be introduced into the unit cell to prevent artefactual interactions of the system with its periodic images, allowing for the accurate treatment of heterogeneous surfaces such as those examined in chapter 4.

1.2.3. Solvation Models

As reaction energies and structures can be sensitive to the choice of solvent, special attention needs to be paid to solvation effects. In chapter 4, we assume all reactions take place in the gas phase in an effort to describe the most general case of reactivity. In contrast, chapters 2 and 3 examine reaction pathways that occur in aqueous conditions, which were accounted for through the use of an implicit solvent model. This method allows for the treatment of interactions with a bulk solvent through the formation of a cavity in a dielectric continuum into which the solute is placed without the need to explicitly model the solvation shell.[41,42] In this work, the SMD implicit solvent model was employed to describe the aqueous media.[43]

1.3. General Organization

The work in this thesis focuses on the use of computational methods to elucidate the thermodynamic properties of three different chemical processes with important environmental relevance. Chapter 2 describes a computational evaluation of the behavior

of both the nerve agent VX and the simulant molecule DMMP in aqueous solution. Special attention was paid to describing the inactivation of DMMP through the use of base catalyzed hydrolysis and a computational protocol was developed to assess catalytic activity through the calculation of the free energy barrier associated with the rate limiting step. The free energy of these catalytic barriers was then used to predict the activity of two new classes of organic catalysts, including the effects of several different R-groups, without the need to either synthesize the organic systems or work with toxic organophosphates.

In chapter 3 the catalytic pathway of a copper-based water oxidation catalyst using environmentally friendly bicarbonate ligands was examined.[44] The labile nature of the ligands, in addition to the high external potential applied to this system, prevented a conclusive *experimental* description of the structural identity of the catalyst. This work used DFT to propose a complete catalytic cycle for this homogenous mononuclear catalyst through the calculation of a free energy surface consistent with the existing experimental information. Special attention was paid to the sensitivity of the system to pH, which results in the availability of multiple reaction pathways, and to the redox non-innocent nature of the ligands, which allows for the formation of a novel peroxycarbonate containing intermediate.

Chapter 4 outlines a computational survey of the ability of ten nitrogen-rich aromatic molecules to bind both to an aluminum metal surface and to the two most common terminations of the environmentally prevalent α-alumina surface. This work describes the most stable binding modes of these nitrogen-rich adsorbates to each of the aluminum

containing surfaces. Special attention was paid to the impact that nitrogen substitution on the aromatic ring and the identity of the aluminum containing surface have upon both the nature of the surface coordination and the electronic binding energies in an effort to identify the adsorbate-surface interactions that result in strong adsorption.

Chapter 2. Modeling Phosphonate Nerve Agent Interactions with Organocatalysts

2.1. Introduction

The global desire to reduce the use of chemical warfare agents has many nations looking for improved methods to reduce current weapons stockpiles. Remediation of nerve agent stockpiles poses a particular challenge due to the enormous toxicity of these compounds.[45-47] Current large-scale remediation strategies generally rely on incineration of nerve agents or chemical degradation via hydrolysis using sodium hydroxide as a base.[48-50] Base hydrolysis proceeds by nucleophilic hydroxide attack on the phosphorus center concomitant with or followed by the elimination of an original ligand, where the latter may be a halide, an alkoxide, or a thiolate.[50-53] Hydroxide-based hydrolysis proves critically insufficient in the case of VX nerve agent, since while hydrolysis generates a non-toxic product, EMPA, in 87% yield, it also produces a toxic product, EA2192, with a 13% yield (Figure 2.1), and EA2192 is persistent under typical reaction conditions.[54-57]

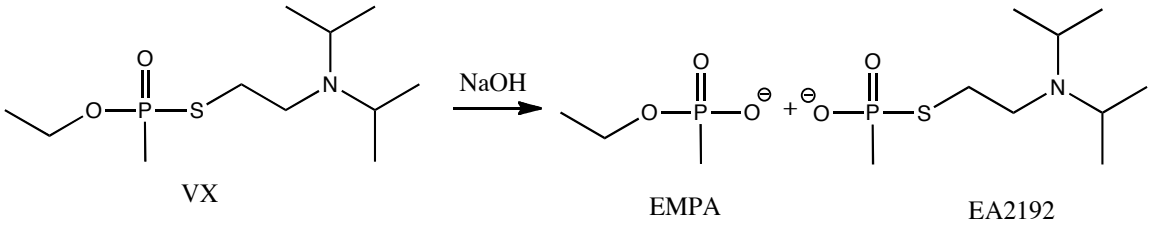

Figure 2.1. Hydrolysis of VX nerve agent yielding both non-toxic (EMPA) and toxic (EA2192) products.

Given the inadequacy of simple basic aqueous hydrolysis, there has been substantial research activity devoted to indentifying alternative procedures for the large-scale destruction of VX that results in exclusively non-toxic products under practical conditions. A variety of inorganic catalysts,[58-61] oxidation agents,[53,62-64] heterogenous catalysts,[65-70] and biological approaches[71-75] have been examined. We have focused on investigating the utility of various organic catalysts for the selective hydrolysis of VX nerve agent. The catalyst structures were chosen based on consultation with TDA Research Inc., which pursues experimental work in this area. Catalysts presented in this report were identified as potential candidates by TDA and we undertook the task of theoretical characterization of their catalytic activity.

We focused our efforts on two classes of organic catalysts, built on either thiourea or benzimidazole backbones (Figure 2.2). These compounds have been found to exhibit enzyme like multisite catalytic activity by activating crucial oxo-groups through hydrogen bonding using the two backbone NH substituents, with a single remaining amine group possessing the ability to act as a catalytic base or nucleophile.[76-78] Further tuning of the reactivity can be accomplished through adjustment of the R-groups on the exocyclic amine.

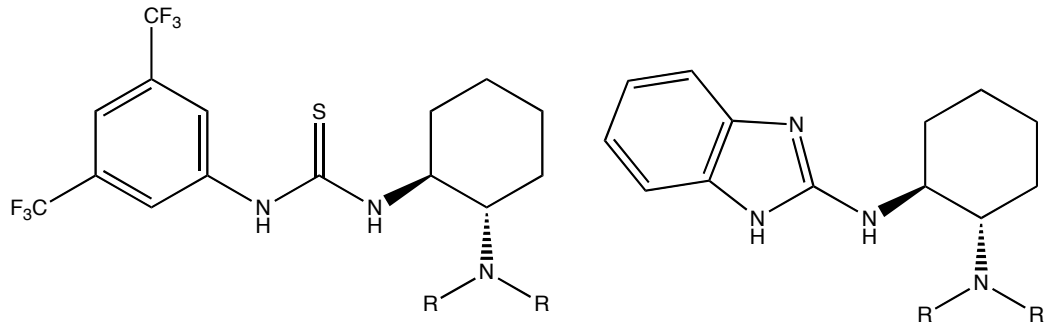

Figure 2.2. Thiourea- (left) and benzimidazole-based (right) potential catalyst families.

In order to assess the possible catalytic activity of these compounds, computational methods were employed to evaluate the free energies of activation for various catalyzed and uncatalyzed hydrolytic nucleophilic substitution reactions of a simple VX analog, especially for those reactions leading to corresponding analogs of EMPA and EA2192. In particular, the truncated model O,S-dimethyl methylphosphonothiolate (DMMP) was chosen as it has been previously shown to predict results in good agreement with experiment for the simple hydrolysis and hydro*peroxido*lysis of VX.[48,51-53] As a first step, a thorough conformational analysis of DMMP was undertaken employing a variety of computational methods, this was done to assist in choosing an appropriate theoretical protocol that can optimally combine accuracy and efficiency, and to correctly identify the lowest energy conformer, which defines the zero of energy structure for possible catalytic pathways. These DMMP conformers were then compared to a survey of the lowest energy conformers for VX, to assess the accuracy of using the truncated model system.

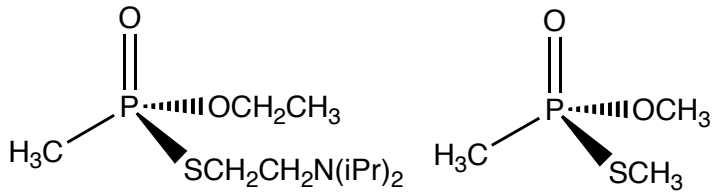

VX DMMP

Figure 2.3. Structures of VX and DMMP.

2.2. Computational Methodology

Optimized geometries and frequencies were calculated using the M06 family of density functionals; M06-L, M06, and M06-2X, which include 0, 28, and 56% Hartree-Fock exchange, respectively, allowing for an effective comparison of local and hybrid

functionals using either the 6-31G(d) or the 6-31+G(d,p) basis sets.[19,79,80] Evaluation of vibrational frequencies at these levels was performed in order to compute thermodynamic partition functions and to correctly identify the character of stationary points as minima or transition-state structures. Aqueous solvation effects were included through use of the SMD continuum solvent model with free energies reported for an aqueous solution with a standard-state concentration of 1 M for solutes, and 55.5 M for water.[81]

In order to assess the accuracy of the density functional methods, comparison was made to two post-Hartree-Fock wave function theories for the conformational analysis of DMMP. In particular, we examined spin-component-scaled second order perturbation theory, SCS-MP2, and the highly correlated compound method CBS-QB3.[82,83] We considered both gas-phase optimizations followed by aqueous single points, and the optimization of structures including SMD solvation effects. All calculations were performed using *Gaussian 09* and an initial database of surveyed VX and DMMP conformers was generated using PCModel.[84]

2.3. Results

2.3.1. Conformational Analysis

2.3.1.1. DMMP

In order to characterize the potential energy surface of the VX simulant DMMP in aqueous solution, a conformational analysis was undertaken. Initial calculations were performed at the M06-L, M06, and M06-2X levels using the 6-31+G(d,p) basis set with gas-phase optimizations, aqueous single point calculations on the gas phase minima

structures, and structures optimized in aqueous solvent. A conformational search identified five unique minima (Figure 2.4) for which relative Gibbs free energies are provided in Tables 2.1 and 2.2.

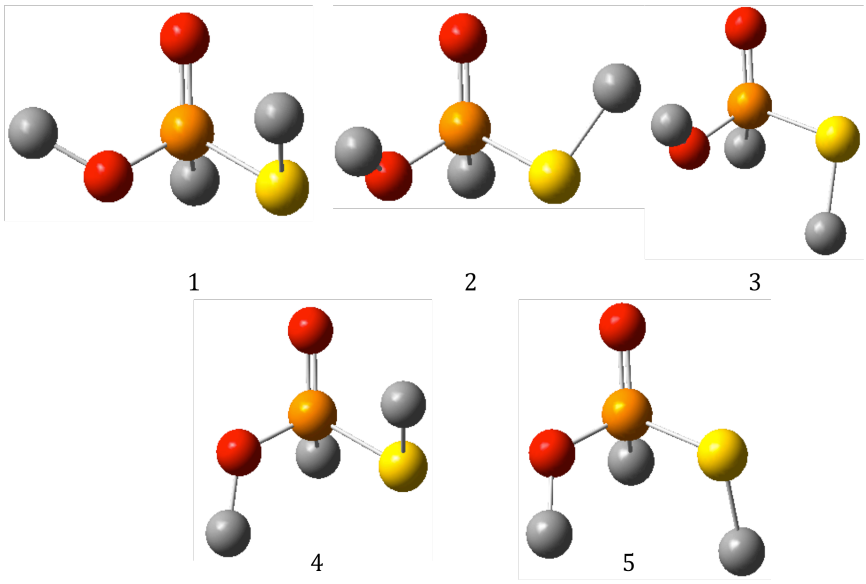

Figure 2.4. Optimized DMMP minima structures. Hydrogen atoms are not shown for clarity. Phosphorus atoms are pumpkin, sulfur atoms are lemon, oxygen atoms are cherry, and carbon atoms are ash.

Table 2.1. Relative free energies (kcal/mol) of DMMP minima, calculated at various DFT levels of theory.

	Gas Phase Optimization			SMD Single Points			SMD Optimizations		
Complex	M06-L	M06	M06-2X	M06-L	M06	M06-2X	M06-L	M06	M06-2X
1	2.55	2.53	1.97	2.08	2.45	1.86	2.09	1.74	1.29
2	0.00	0.00	0.00	0.94	1.42	1.46	1.09	0.34	0.35
3	1.33	0.98	1.06	0.00	0.00	0.00	0.00	0.00	0.00
4	3.22	3.33	3.53	1.45	1.48	1.73	0.71	1.00	0.42
5	8.00	8.40	8.92	3.03	3.26	3.44	2.50	2.16	2.54

Table 2.2. Relative free energies (kcal/mol) of DMMP minima calculated using various levels of wave-function theory.

	Gas Phase Opt		SMD S.P.	SMD Opt
Complex	CBS-QB3	SCS-MP2	SCS-MP2	CBS-QB3
1	2.52	2.59	2.16	2.44
2	0.00	0.00	1.16	1.34
3	0.83	0.95	0.00	0.00
4	3.35	3.51	2.39	1.70
5	7.73	8.06	3.78	2.94

In the gas phase, all levels of theory predict conformer **2** to be the most stable, likely due to the favorable anomeric effects associated with its gauche C-O-P-O and C-S-P-O dihedrals.[18] However, when aqueous solvation effects are included, all conformers are stabilized by ~2 kcal/mol for each methyl group oriented *s-trans* relative to the P=O bond. This stabilization likely derives from a combination of the greater ability of the implicit solvent model to interact with the polar P=O unit coupled with the localization of the negative lone pair density into a small region of solvent accessible space when the ester groups are *s-trans*. These solvation effects render conformer **3** the dominant species in aqueous media.

When energies from aqueous single points are compared to those calculated from structures optimized using SMD, we find that the single-point (S.P.) energies agree qualitatively with those from the optimized geometries, but are in quantitative disagreement. For example, the change in the relative M06-L energies upon inclusion of SMD into the optimization protocol can vary between 0.0 to 0.7 kcal/mol, while a much

greater variance can be seen for the hybrid M06 and M06-2X functionals. This trend indicates that the use of single-point solvation energies reveals rough trends in the relative energies, but that structures should be optimized in aqueous media in order to ensure quantitatively accurate energetic values.

The DFT energies can also be compared to those calculated with correlated wave function theories. Considering SCS-MP2 and CBS-QB3 gas-phase energies, we see that the two methods agree reasonably well with each other, enhancing confidence in their quantitative accuracy. Of the M06 functional family, it is M06-L that predicts the best agreement in gas-phase energies compared to the wave function theories. In addition, all methods predict similar energetic stabilizations upon the inclusion of implicit solvent. However, all DFT methods appear to predict structure 4 to possess a somewhat lower relative free energy than calculated by CBS-QB3, indicating a possible discrepancy for this structure and method. However, the general agreement with higher-level theoretical methods indicates that M06-L is an accurate functional to use for further studies.

2.3.1.2. VX

A similar conformational analysis was also performed for the full VX molecule. A stochastic PCModel search was performed and the 97 lowest energy conformers were selected. Gas phase optimizations were then performed using M06-L/6-31G(d). Solvation corrections were then included by performing single point SMD continuum solvent model calculations, allowing for the identification of the lowest energy solution phase conformers. Further aqueous phase SMD optimizations were then performed for

the 20 lowest energy conformers. By ignoring iso-propyl rotations, the resulting structures could be separated into five classes that contain at least one conformer with a relative free energy below 1 kcal/mol (Figure 2.5, Table 2.3).

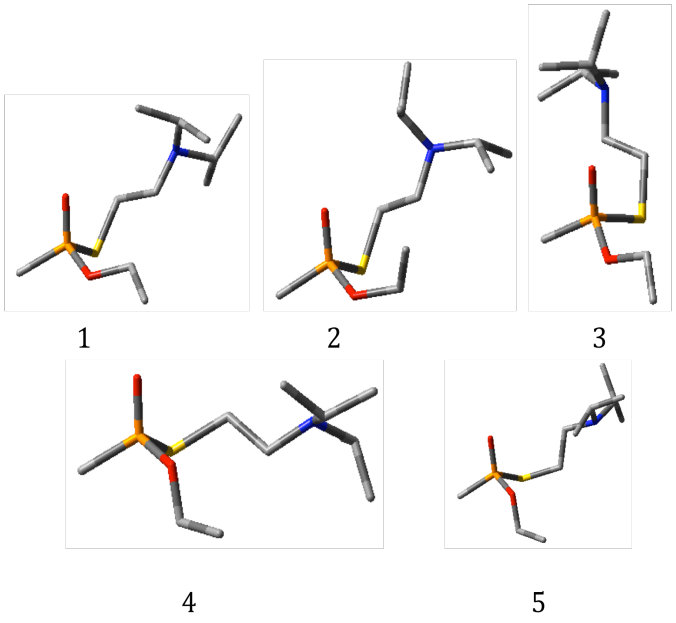

Figure 2.5. VX conformer classes having members with relative free energies below a 1 kcal/mol energy cutoff.

Table 2.3. Relative free energies (kcal/mol) of VX minima at the SMD/M06-L/6-31G(d) level.

Classes	Free Energies
1	0.00
2	0.38
3	0.39
4	0.81
5	0.88

Classes one, two and three possess ester rotations analogous to those of DMMP conformer **2**. Classes four and five contain ester rotations analogous to those of conformer **4**, as they include an ethoxy ligand rotated anti to the central P=O group. Comparing these conformers to the smaller DMMP analog we can make some insights about the nature of the differences between these two systems. We find the most stable classes of VX conformers place both ester-units syn-relative to the central P=O group in a similar fashion to the gas-phase DMMP conformer, indicating that the bulky VX substituents likely shield the central core from solvent effects. Additionally, while DMMP favors the rotation of the thiol substituents, for the full VX system, rotation of the smaller ethoxy ligand becomes favorable. These conformer differences help illustrate that while the small DMMP analog serves well to model hydrolysis, it will experience slightly different interactions with an external environment.

2.3.2. Reaction Pathways

Analysis of the catalytic hydrolysis of DMMP was undertaken by performing optimizations using M06-L/6-31+G(d,p)/SMD. Focus was placed on the hydrolysis of DMMP through the use of a catalytically activated water molecule and the subsequent formation of the possible products, EA2192 and MMPA, with particular attention paid to the initial attack step. Cases of direct attack by catalytic nitrogen and oxygen nucleophiles at the phosphorus center were also considered. These systems were compared to activation by triethyl amine (TEA), which serves to represent the uncatalyzed system, where activation of a water molecule occurs through deprotonation by the tertiary amine.

2.3.2.1. TEA

Two competing pathways making use of TEA as a general base were considered in which deprotonation of the chemically active water molecule occurs in a concerted manner with nucleophilic attack on the central phosphorus atom of DMMP (Figure 2.6). Pathway 1 involves the recruitment of TEA and a water molecule by DMMP to form a slightly exothermic pre-reactive complex where the water molecule can attack the phosphorus center opposite the methanethiolate group and proceed through a trigonal bipyramidal transition-state (TS) structure with a free energy barrier of 22.3 kcal/mol to generate an intermediate product 19.7 kcal/mol above separated reactants. This pathway involves a lengthening of the P-S bond from 2.09 to 2.42 Å, with a TS distance of 2.20 Å; a marginal lengthening of the P-O bond to the methoxy group, from 1.62 to 1.67 Å, is also observed (Table 2.4). The high-energy intermediate can then dissociate the methanethiolate group with a predicted barrier of 0.7 kcal/mol, leading to separated products which are predicted to be 1 kcal/mol lower in energy than the original starting materials. The product triethylammonium can then be deprotonated by the ejected thiolate molecule, resulting in a highly exergonic reaction with products 22.7 kcal/mol more stable than the original reactants.

To evaluate the impact of the choice of computational protocol, energies for pathway 1 were calculated using M06-2x, which predicts a complexation energy 3.4 kcal/mol downhill, and a transition state energy of 14.3 kcal/mol, which translate into an energetic barrier of 17.7 kcal/mol. This is a lowering of the energy barrier by ~4 kcal/mol, despite a similar geometry to the M06-L structure. In addition, M06-2x predicts a low energy

endpoint to the reaction coordinate of 2.6 kcal/mol, though the large P-S distance of 3.9 Å indicates that the bond has been completely cleaved and that M06-2x predicts no intermediate structure for this case. This lack of an intermediate complex casts doubt on the accuracy of the M06-2x functional.

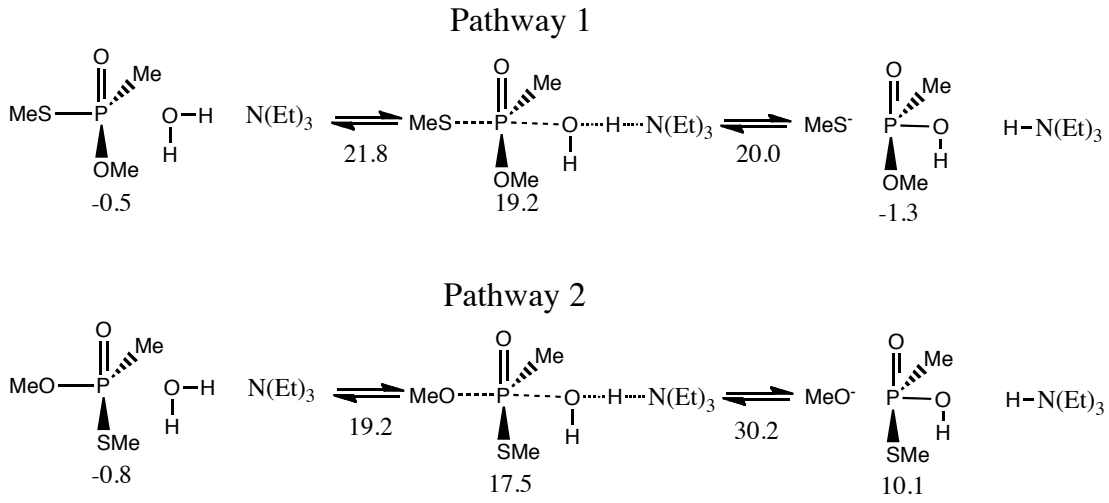

Figure 2.6. Two TEA catalyzed pathways for the hydrolysis of DMMP with energies in kcal/mol. The hydrolysis can occur opposite the methanethiolate substituent (pathway 1) or the methoxy group (pathway 2).

Table 2.4 Geometric data for the catalytic DMMP subunit for the TEA catalyzed pathway 1, reporting all phosphorus containing bond lengths in addition to the relative position of the proton being transferred to the TEA nitrogen atom.

Tea Pathway 1	P-SMe	P-OH	P-OMe	P=O	O-H	N-H
Complex	2.09 Å	3.87 Å	1.62 Å	1.50 Å	0.99 Å	1.86 Å
TS	2.20 Å	2.24 Å	1.65 Å	1.51 Å	1.54 Å	1.09 Å
Intermediate	2.42 Å	1.78 Å	1.67 Å	1.53 Å	1.75 Å	1.05 Å

The geometric data for the M06-L intermediate and both TS structures agrees well with a previous computational study of Seckute et al.,[51] which investigated the reaction of hydroxide with DMMP. They described a hydroxide catalyzed pathway, which possessed an activation free energy of 18.8 kcal/mol, an intermediate with a P-S distance of 2.3 Å and an energy of -3.7 kcal/mol with a negative free energy barrier for disassociation using MP2 single point energies. The lower energies calculated for this system are likely due to the more nucleophilic character of hydroxide compared to a TEA activated water molecule. Comparison to this work also helps support the choice of the M06-L functional, as M06-2X does not predict an intermediate structure, and predicts an unphysical lower free energy barrier for the TEA catalyzed system than previously calculated for the strong-base catalyzed system.

The alternative pathway 2 mechanism involves the attack of the activated water molecule opposite the methoxy group. This mechanism also goes through a trigonal bipyramidal TS structure with an activation free energy of 20.0 kcal/mol and a subsequent intermediate of 18.3 kcal/mol compared to the starting complex. At the TS, this pathway involves a lengthening of the P-S bond from 2.09 to 2.17 Å and the P-O bond from 1.62 to 1.76 Å (Figure 2.5). Subsequent elimination of the methoxy group occurs with an energetic barrier of 12.7 kcal/mol, so that the TS structure is 30.2 kcal/mol above separated reactants. This observation is likely a computational artifact, as the final products are 10.1 kcal/mol higher in energy than the separated reactants, and the elevated energy is likely due to the newly generated negative charge. If the methoxide molecule is permitted to deprotonate the product triethylammonium, the reaction yields methanol and

the toxic EA2192, with the new products 18.2 kcal/mol lower in energy than the starting complex, demonstrating that the exothermic nature of the reaction pathway is preserved.

Table 2.5 Geometric data for the catalytic DMMP subunit during TEA catalyzed pathway 2, which reports all phosphorus containing bond lengths in addition to the relative position of the proton being transferred to TEA.

Tea Pathway 2	P-SMe	P-OH	P-OMe	P=O	O-H	N-H
Complex	2.09 Å	3.67 Å	1.62 Å	1.50 Å	0.99 Å	1.85 Å
TS	2.12 Å	2.40 Å	1.67 Å	1.52 Å	1.57 Å	1.10 Å
Intermediate	2.17 Å	1.84 Å	1.76 Å	1.54 Å	1.73 Å	1.05 Å

Again comparison can be made to the previous study of Seckute et al. for which similar geometric data was obtained.[51] The hydroxide catalyzed pathway 2 possessed an energetic barrier of 14.6 kcal/mol, an intermediate energy of -2.7 kcal/mol, and barrier for disassociation of 15.4 kcal/mol. Again, energetic differences are likely due to the higher nucleophilicity of hydroxide. Additionally, Seckute et al. also proposed a pseudo rotation pathway linking the intermediates of pathway 1 and 2 with an energetic barrier of 14.4 kcal/mol, allowing for methanethiolate release, though this pseudo-rotation was not studied for the TEA catalyzed pathway as we focused our attention on the rate controlling nucleophilic attack step.

By examining the pathway energetics, it can be seen that attack opposite the methoxy ligand is preferred by roughly 4.8 kcal/mol, which is similar to the simple hydroxide case. This illustrates that formation of EA2192 is the kinetically favored reaction. When completely separated products are considered, we see that formation of

EMPA is favored by roughly 4.5 kcal/mol over the formation of the toxic EA2192 in agreement with the hydroxide catalyzed pathway, showing that even though the greater nucleophilic character of hydroxide results in lower energies, both systems possess similar relative energies between the two pathways, illustrating that M06-L accurately describes the catalytic behavior of TEA. This baseline indicates that a successful catalyst should possess an activation free energy of less than 22.3 kcal/mol in order to be catalytically competitive with TEA, and have an even lower energy barrier to offer a reliable alternative to hydroxide based hydrolysis. Additionally, the preference of kinetic elimination of methanethiolate compared to methoxide, to ensure the lack of formation of toxic byproducts, is a property desired in a commercial catalytic system.

2.3.2.2. Thiourea Backbone

The thiourea-based catalyst (Figure 2.2) was tested for several R-groups, with the energetic barriers associated with the attack steps for both pathways 1 and 2 serving as indicators of commercial viability. The R-groups tested were methyl, 2-pyridyl, and 2-phenol. In addition, the methyl R-group was tested for a backbone from which the CF_3 groups had been removed in order to examine the effects of backbone electron-withdrawing groups on reactivity. As only one enantiomer of the optically active catalyst was examined, reaction pathways were investigated for both the *R* and *S* enantiomers of DMMP to evaluate the extent of energetic differences amongst the diastereomers of the reactive bimolecular complexes.

The first case examined was pathway 1 for R=methyl and the *R* isomer of DMMP (Figure 2.7). DMMP and one water molecule undergo favorable binding with the catalyst to form a complex 4.9 kcal/mol downhill in energy, as compared to the completely separated reactants. This favorable binding likely stems from hydrogen bonding of DMMP with the catalytic backbone, with hydrogen bonds of 2.28 and 1.81 Å. In addition, the nucleophilic nitrogen was found to hydrogen bond to the explicit water molecule. This binding is followed by deprotonation of the water molecule with concerted nucleophilic attack of the incipient hydroxide on the phosphorus center, proceeding with a free energy of activation of 23.9 kcal/mol. During this process the hydrogen bonds adjust to 2.01 and 1.86 Å. We see that the DMMP internal geometry is similar to the TEA pathway 1, with the P-S bond lengthening from 2.09 to 2.18 Å showing migration of the methanethiolate away from the central unit. The transition state is followed by a high energy intermediate in which the methanethiolate group is weakly associated with the phosphorus center at a distance of 2.40 Å and only minor changes are observed in the hydrogen bonding network. From this intermediate species, easy elimination of methanethiolate can be expected.

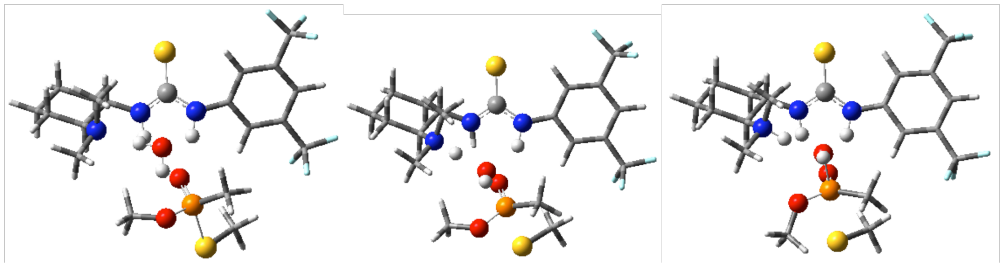

Figure 2.7. Pathway 1 reaction mechanism of the thiourea-methyl catalyst with *R*-DMMP; energies are reported relative to the completely separated products.

The analogous pathway 1 reaction with *S*-DMMP is shown in Figure 2.8, and is structurally very similar to that seen for the *R*-isomer. The most substantial difference is that the methanethiolate subunit is oriented towards the benzyl subsistuent. This change in orientation decreases the interaction of the sulfur atom with the bulk solvent, and as a result the energy of the whole pathway increases, specifically this rotation destabilizes the transition state and leads to a free energy of activation of 25.1 kcal/mol. This indicates that faster hydrolysis should be expected for DMMP when the leaving thiolate group is stabilized by polar interactions, such as those found with the bulk solvent.

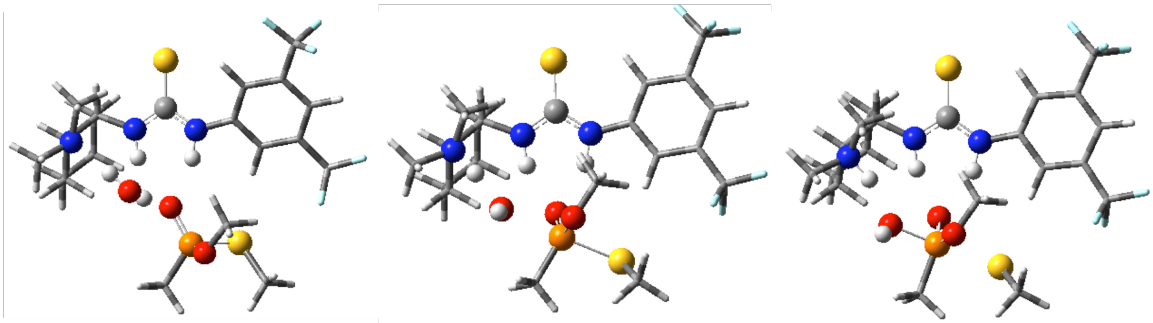

Figure 2.8. Pathway 1 reaction of the thiourea-methyl catalyst with *S*-DMMP with energies relative to the completely separated reactants.

The mechanism for pathway 2 was also examined for *S*-DMMP and showed analogous structures to those available for pathway 1. However, the binding energy is predicted to be exothermeic by 3.6 kcal/mol, which is slightly weaker than for pathway 1 due to steric clashes with the catalyst backbone, as hydrogen bonding appears to be unaffected. The complex can then undergoe nucleophilic water attack with an energetic

barrier of 20.4 kcal/mol followed by an intermediate 17.4 kcal/mol higher in energy than the starting complex. These energies indicate a preference for the formation of the toxic thioester product, casting further doubt on the efficacy of this thiourea catalyst.

In order to test the influence of the electron withdrawing CF_3 groups, the catalytic pathway 1 of thiourea-methyl was tested after substituting in -H groups, which we will henceforth refer to as the unfluorinated-thiourea catalyst (Figure 2.9). The first major difference between these catalysts is found in the hydrogen-bonding network. The unfluorinated complex contains only one strong hydrogen bond with an O-H distance of 1.94 Å. The other backbone amine hydrogen has no clear hydrogen bonding character with an O-H distance of 3.14 Å, leading to a complexation energy 1.6 kcal/mol higher than for the fluorinated system. Upon concomitant deprotonation and attack by the bound water molecule, the unfluorinated transition state possesses the same energy relative to separated reactants as the fluorinated complex; however, due to the destabilization of the starting complex, the unfluorinated system has a free energy of activation of 22.3 kcal/mol, with a value 1.6 kcal/mol lower than for the fluorinated catalyst. After the formation of the starting complex we see geometries and hydrogen bonding character similar to those found in the fluorinated case.

Pathway 2 was also investigated for the unfluorinated-thiourea catalyst. The starting complex for this binding motif also contains only one hydrogen bond to the oxy-group with O-H distances of 3.18 and 2.00 Å and a binding energy comparable to that calculated for pathway 1. Attack of the bound water molecule results in increased hydrogen bonding, with shortening of the O-H distances to 1.86 and 1.92 Å. The

favorable binding differential also appears to decrease the free energy of activation of nucleophilic attack opposite the electronegative methoxy group to 19.0 kcal/mol. A high-energy intermediate is then formed with P-S and P-O distances of 2.15 Å and 1.81 Å respectively, indicating that both methanethiolate and methoxy-groups remain attached and that further reactivity will be required to ensure ligand elimination.

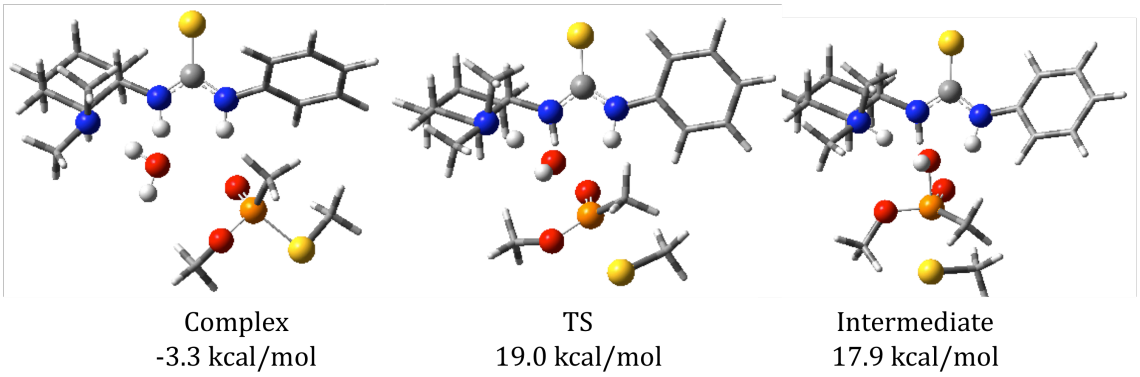

Figure 2.9. Pathway 1 reaction mechanism of the unfluorinated-thiourea catalyst with *R*-DMMP with energies reported relative to the completely separated reactants.

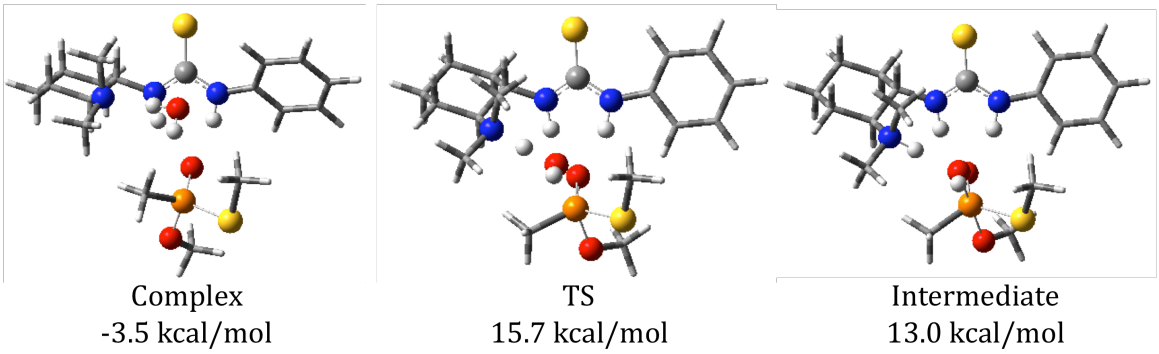

Figure 2.10. Pathway 2 reaction of the unfluorinated-thiourea catalyst with *R*-DMMP, with energies relative to completely separated reactants.

Other R-group substituents were analyzed, including a 2-pyridyl unit (Figure 2.11), which was selected to assess the propensity of the catalyst substituents to act as a general base or nucleophile. For pathway 1, the bound water molecule in the starting complex was predicted to hydrogen bond to both the exocylic and pyridyl amines with additional hydrogen bonding of the DMMP oxo-group to the thiourea backbone with O-H distances of 2.06 Å and 1.91 Å. Despite backbone hydrogen bonding comparable to that found for R=methyl, the bound complex is predicted have an endothermic binding energy of 1.5 kcal/mol compared to separated reactants, indicating unfavorable DMMP capture. Additionally, the nucleophilic attack of the bound water molecule possesses a free energy of activation of 25.8 kcal/mol with a transition state P-S distance of 2.26 Å. The subsequent intermediate complex is found to be 23.2 kcal/mol uphill with a P-S distance of 2.46 Å. The steering of the hydrogen bonding associated with the inclusion of pyridyl substituents appears to decrease the nucleophilicity of the reactive water, whether from a steric constraint placed on the activated water molecule, or via reduced basicity of the aliphatic amine upon R-group substitution remains undetermined.

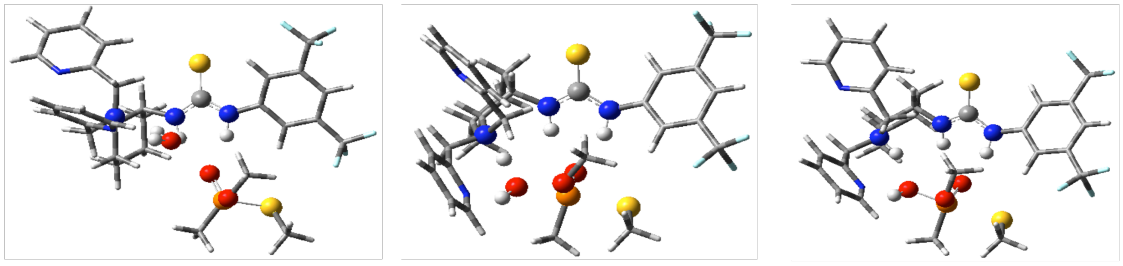

Figure 2.11. Pathway 1 reaction of the thiourea-2pyridyl catalyst with *S*-DMMP, with energies reported relative to the completely separated reactants.

Pathway 2 was also considered for the thiourea-2-pyridyl system (Figure 2.12). A similar structure and endothermic binding energy was seen for the catalytic complex as was predicted for pathway 1, though shorter P-S and P-O distances were predicted with bond lengths of 2.16 and 1.76 Å, respectively. The subsequent water nucleophilic attack possesses a free energy of activation of 20.9 kcal/mol, which like pathway 1 is also more energetically demanding than expected for the methyl R-group. It is worth noting that the kinetic barrier for pathway 2 remains 4.7 kcal/mol more favorable than is predicted for attack opposite the methanethiolate group, illustrating a continued kinetic preference for pathway 2.

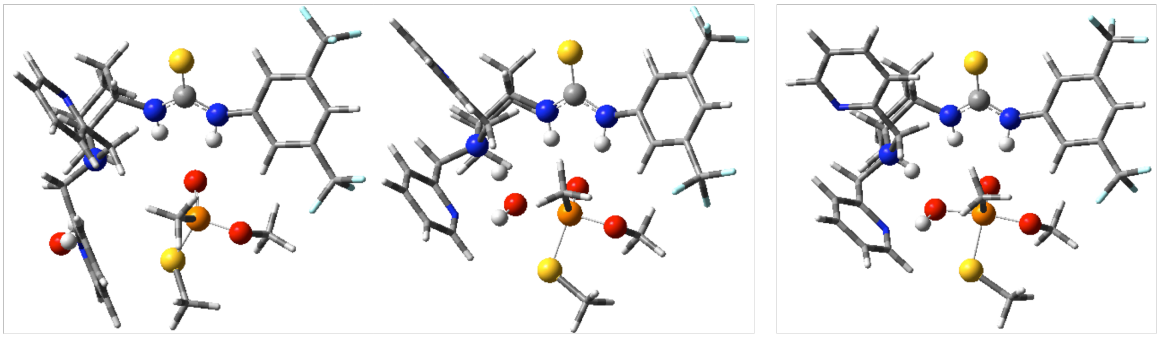

Figure 2.12. Pathway 2 reaction mechanism of thiourea-2-pyridyl with *S*-DMMP, with energies reported relative to completely separated reactants.

An alternative version of pathway 1 involving the thiourea-2-pyridyl system examined the nucleophilic attack by the pyridyl amine at the phosphorus center directly opposite the methanethiolate group (Figure 2.13). The catalyst was predicted to bind

DMMP directly with an endothermic energy of 6.0 kcal/mol with weak hydrogen bonds to the oxo-group exhibiting O-H distances of 2.11 and 2.18 Å and a P-N distance of 4.07 Å. The subsequent nucleophilic attack was found to occur with a strong dissociation of the P-S bond to a transition state length of 3.08 Å, while the P-N distance shortens to 1.97 Å. In addition, the formation of a second hydrogen bond is unstable due to steric limitations, resulting in O-H distances of 1.93 and 2.93 Å, and combined with the energetic nature of the newly formed P-N bond is likely responsible for the high free energy of activation barrier of 40.5 kcal/mol. A high-energy intermediate is subsequently formed with a P-S distance of 3.63 Å, indicating complete cleavage of the bond to the methanethiolate group. The energetic nature of this pathway illustrates that nucleophilic attack by a water molecule is preferred over the direct attack of an aromatic amine, though the use of a flexible catalyst backbone that can stabilize the transition state complex may allow for competitive energetics.

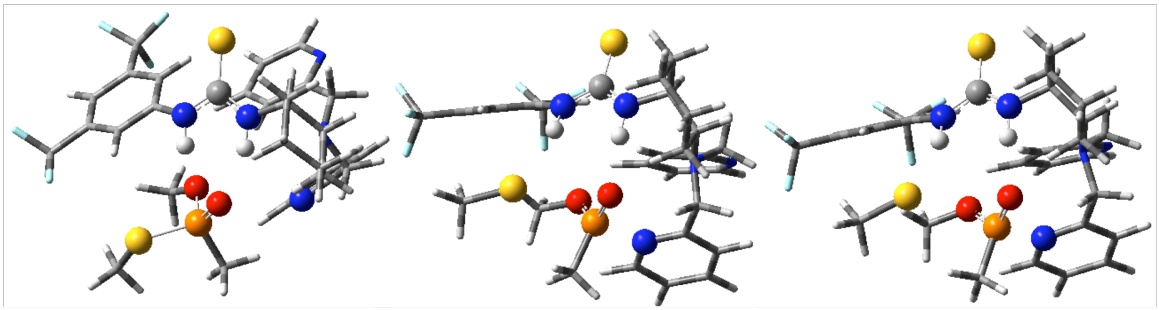

Figure 2.13. Pathway 1 reaction of the thiourea-2-pyridyl catalyst with *S*-DMMP through the direct attack by the nucleophilic amine, with energies reported relative to the completely separated reactants.

Pathway 1 was also examined for a 2-phenol R-group substituent (Figure 2.14). This pathway was optimized at the M06-2X level of theory due to difficulties in the optimizations performed at the M06-L level for reasons that will not be pursued here. It is important to note that the thiourea-2-phenol catalyst possesses two phenol groups in solution but one of the phenol alcohol groups can be deprotonated by the nucleophilic amine with a low free energy barrier to produce a single phenolate R-group that is predicted to be 3 kcal/mol endothermic in energy, with destabilization of this zwitterion form likely due to local solvation effects stemming from the bulky non-polar nature of the catalyst. This phenolate form of the catalyst can bind DMMP, producing a complex 7.4 kcal/mol higher in energy than separated reactants. This complex possesses hydrogen bonds similar to the thiourea-methyl system with O-H distances of 2.28 and 1.92 Å, with the elevated complexation energy likely stemming from the lack of hydrogen bonds to a bound water molecule. The pathway then proceeds through a TS structure with a free energy of activation of 19.1 kcal/mol and similar hydrogen bonding and internal DMMP bond distances as those seen for the methyl R-groups. A high-energy intermediate is then produced with similar internal geometries as seen in the thiourea-methyl case. While the free energy barrier is fairly low, the tendency for M06-2X to predict lower energy barriers by ~4 kcal/mol would indicate a similar activation energy to those found for the thiourea-methyl catalyst. Additionally, the 2-phenol containing system possesses a much higher binding energy of the substrate, indicating that while direct nucleophilic attack by a phenolate catalyst may be possible, special considerations would need to be made to ensure the favorable coordination of DMMP.

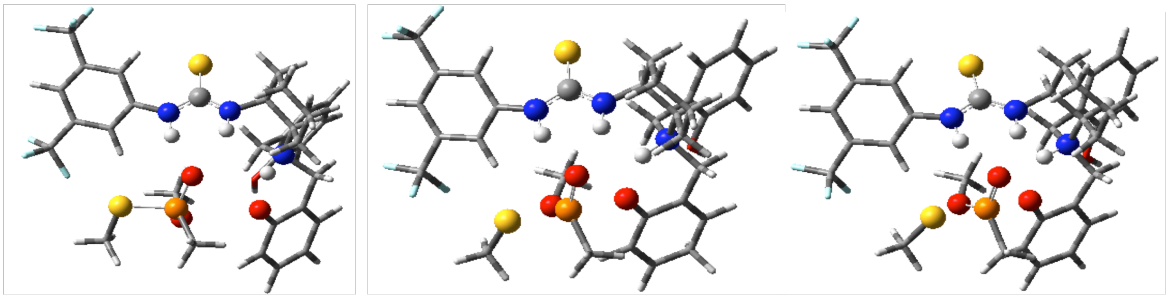

Complex
7.4 kcal/mol

TS
19.1 kcal/mol

Intermediate
19.7 kcal/mol

Figure 2.14. Pathway 1 reaction of the thiourea-2phenol catalyst with *S*-DMMP with direct attack by the 2-phenolate substituent, with energies reported relative to the completely separated reactants.

2.3.2.3. Benzimidazole Backbone

The benzimidazole backbone (Figure 2.2) was examined for methyl R-groups. The backbone imidazole was considered both in its free base and conjugate acid forms to test the effects of protonation upon catalyst activation of DMMP through hydrogen bonding. Consideration of both protonation states of the backbone system is important, as either form could be present in the aqueous phase depending on the pH of the solution. Both forms of the catalyst were analyzed for pathways 1 and 2 in order to assess the impact of protonation on the difference in free energies between the two pathways.

For pathway 1, the benzimidazole-methyl complex forms with a slight downhill energy of 1.0 kcal/mol (Figure 2.15). This small binding energy is associated with the formation of a single hydrogen bond between the imidazole group and the DMMP oxo-group with an O-H distance of 1.93 Å. A second hydrogen bond is formed between the

protonated aliphatic amine and the methoxy group, with an O-H distance of 2.05 Å. This hydrogen-bonding motif with coordination to two different oxygen atoms is unique compared to the coordination seen in the thiourea catalyst and is likely due to the larger distance between the nitrogen atoms of the benzimidazole backbone. This hydrogen bonding character is maintained throughout the nucleophilic attack reaction coordinate, which is characterized by a free energy of activation of 24.2 kcal/mol. A high-energy intermediate is then formed with the O-H distance to the oxo-group shortening to 1.83 Å while no change occurs in the length of the hydrogen bond to the methoxy group. In addition only slight bond lengthening occurs in the P-O distance to the methoxy unit. However, the P-S distance lengthens from 2.09 to 2.35 Å, illustrating the weakening of P-S bond and is analogous to the bound distances found in the thiourea systems.

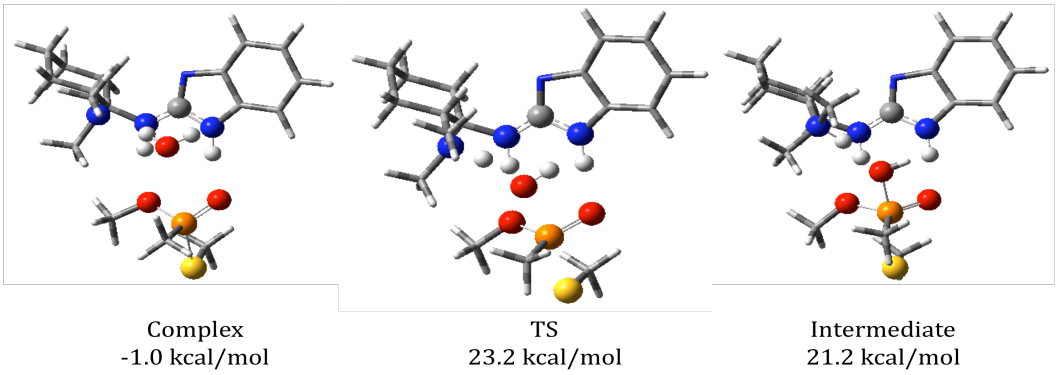

Figure 2.15. Pathway 1 reaction coordinate of benzimidazole-methyl catalyzing the hydrolysis of *R*-DMMP, with energies reported relative to completely separated reactants.

The protonated form of the benzimidazole backbone was investigated for pathway 1, and the DMMP bound complex was found to contain similar hydrogen bonds to both the

oxy and methoxy groups as found in the depotonated form, with hydrogen bond lengths of 1.77 and 2.00 Å respectively (Figure 2.16). Though both of these distances are shorter than predicted for the unprotonated system, an identical complexation energy was calculated. The following nucleophilic attack was characterized by a transition state with a free energy barrier of 24.7 kcal/mol, slightly higher than that found for the unprotonated system despite a very similar geometry. The subsequent intermediate was predicted to be 0.8 kcal/mol lower in energy than for the unprotonated system, likely due to the shorter O-H bonds of 1.68 and 1.92 Å to the oxy and methoxy groups respectively. Despite the continually stronger hydrogen bonds of this pathway, no major energetic benefit was provided, though preference for this pathway would be expected at a lower pH.

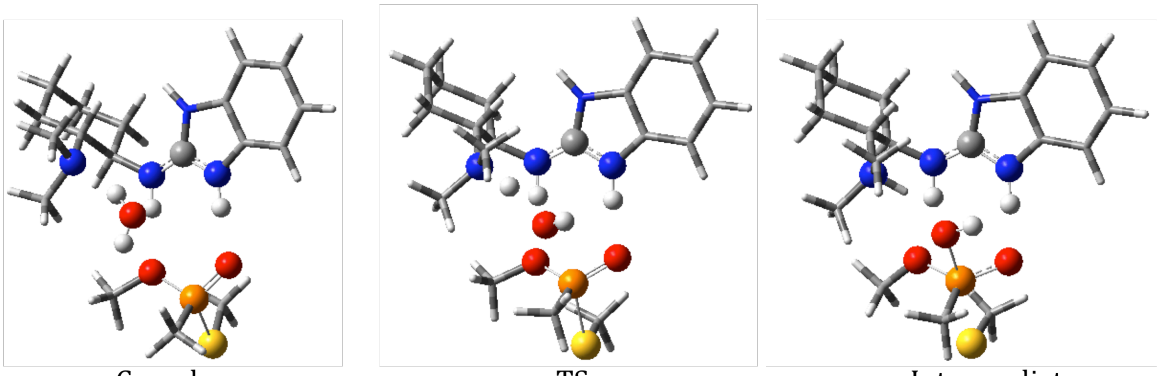

Figure 2.16. Pathway 1 reaction mechanism for protonated benzimidazole-methyl catalyzed hydrolysis of *R*-DMMP, with free energies reported relative to the completely separated reactants.

In order to consider all possible reaction mechanisms, pathway 1 was also considered for the rotation of the benzimidazole group with respect to the bridging amine,

allowing for the unprotonated aromatic amine to deprotonate the nucleophilic water molecule (Figure 2.17). The bound complex was formed with a single hydrogen bond to the oxo-group with a distance of 2.01 Å and the bound water molecule was coordinated to the two deprotonated amines, with a slight downhill binding energy of 0.6 kcal/mol. A free energy of activation of 25.9 kcal/mol was associated with the concerted deprotonation of the water molecule by the aromatic amine and the attack of the incipient hydroxide on the phosphorus center. In the resulting intermediate, the phosphate complex was bound to the catalyst by single hydrogen bond of 1.80 Å, and the internal P-S distance of 2.42 Å shows similar character to the thiourea catalyzed systems. However, the elevated energy of the TS structure suggests a preference for the catalytic deprotonation of the bound water molecule through an aliphatic amine.

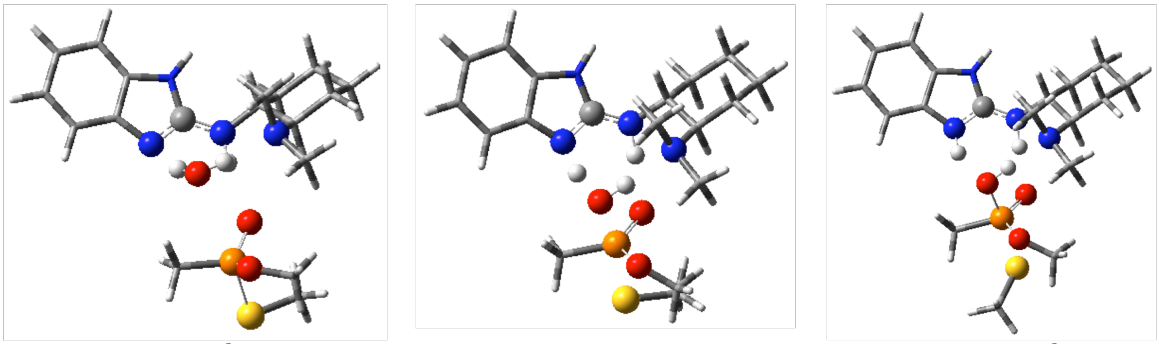

Figure 2.17. Mechanism of pathway 1 reaction of a rotated benzimidazole-methyl catalyst with *R*-DMMP, with energies reported relative to completely separated reactants.

In order to fully describe the benzimidazole-methyl system, pathway 2 must also be considered (Figure 2.18). For the unprotonated system, the catalytic complex forms with

two hydrogen bonds to the oxo-group with O-H distances of 2.06 and 2.07 Å, resulting in a weak association energy. Formation of the complex is followed by water nucleophilic attack at the phosphorus center, opposite the methoxy group, with a free energy of activation of 19.9 kcal/mol. The subsequent intermediate complex contains asymmetric hydrogen bonds with O-H distances of 1.93 and 2.16 Å and short P-S and P-O distances of 2.16 and 1.67 Å respectively indicating that both the methanethiolate and methoxy units remain attached to the phosphorus center. However, further reactivity should enable the cleavage of either the P-S or P-O bonds, allowing for the formation of either the toxic or benign product species.

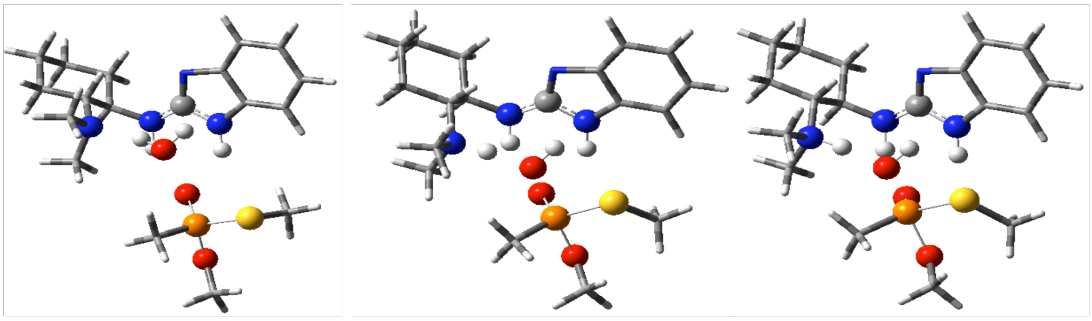

Figure 2.18. Pathway 2 reaction mechanism for the benzimidazole-methyl catalyzed hydrolysis of *R*-DMMP, with energies reported relative to completely separated reactants.

Pathway 2 was also considered for the protonated benzimidazole-methyl catalyst (Figure 2.19). The bound complex is formed with a favorable binding energy of 1.1 kcal/mol, with short O-H distances of 1.99 and 2.01 Å. This pathway proceeds through a transition-state structure with short O-H distances of 1.83 and 2.09 Å and an elevated free energy of activation of 22.2 kcal/mol and a subsequent intermediate energy of 19.2

kcal/mol. The increased activation energy upon protonation of the catalyst indicates that the use of the benzimidazole catalyst at a low pH may disfavor the generation of the toxic thio-ester product.

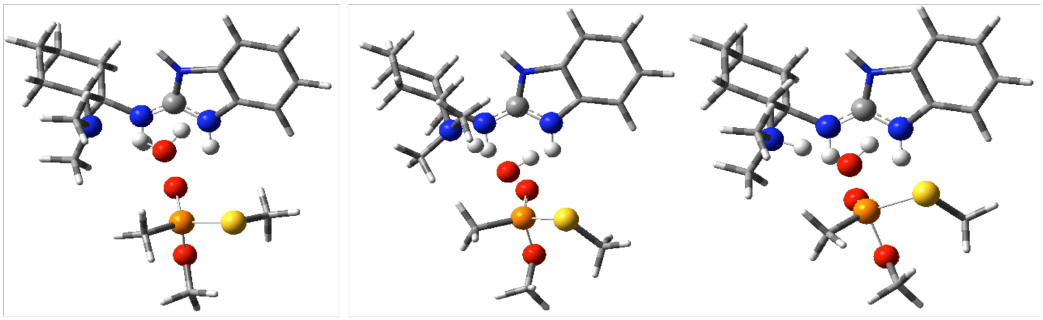

Figure 2.19. Pathway 2 reaction mechanism for the protonated benzimidazole-methyl catalyst with *R*-DMMP, with energies reported relative to completely separated reactants.

2.4. Conclusions

By considering the totality of all of these reaction pathways, trends in the catalytic hydrolysis of DMMP can be drawn. This requires a consideration both the binding energy of DMMP to possible catalysts and the energetic barriers for the nucleophilic attack step (Table 2.6). Analysis of key bond lengths can also help reveal the qualitative strengths of hydrogen bonds and the degree of coordination of phosphorus to both ester and thioester substituents for a wide array of complexes. By examining DMMP binding to the various catalysts, we note that for all catalysts the energy of recruiting the pre-reactive complex is similar for both pathways 1 and 2. This consistency of energetics illustrates a lack of preference for the alignment of the bound substrate and an absence of selection for either catalytic pathway.

Table 2.6. Comparison of all possible catalysts and pathways with energies reported with respect to the completely separated reactants.

Complex	Pathway	Complex (kcal/mol)	TS (kcal/mol)	Intermediate (kcal/mol)
TEA	1	-0.5	21.8	19.2
TEA	2	-0.8	18.4	16.6
Thiourea-Methyl *R*-DMMP	1	-4.9	19.0	18.4
Thiourea-Methyl *S*-DMMP	1	-4.6	20.5	18.7
Thiourea-Methyl	2	-3.6	16.8	13.8
Unfluorinated Methyl	1	-3.3	19.0	17.9
Unfluorinated Methyl	2	-3.3	15.7	13.0
Thiourea 2-pyridyl	1	1.5	27.2	24.7
Thiourea 2-pyridyl	2	1.5	22.5	21.8
Thiourea 2-pyridyl Direct Attack	1	6.0	40.5	37.8
Thiourea 2-phenol*	1	7.4	19.1	19.7
Benzimidazole	1	-1.0	23.2	21.2
Rotated Benzimidazole	1	-0.6	25.3	21.2
Benzimidazole	2	-0.5	19.4	18.9
Protonated Benzimidazole	1	-1.0	23.7	20.4
Protonated Benzimidazole	2	-1.1	21.1	19.2

*Energies calculated using M06-2X

A second important trend is that for the methyl R-group, the thiourea backbone shows consistently stronger binding energies to starting materials compared to the benzimidazole backbone. The benzimidazole catalysts only shows strong binding to DMMP with a single hydrogen bond, with all complexes possessing only one O-H

distance less than 2 Å. The presence of this binding motif is further supported by the observation that *all* benzimidazole complexes have roughly the same binding energy, including the rotated complex, for which only one hydrogen bond *can* be formed. In addition, no significant additional binding energy is gained upon protonation of the benzimidazole complex, illustrating that little additional activation of the N-H groups is produced. The addition of electron withdrawing CF_3 groups to benzimidazole could increase the acidity of the amine proton, though the effect on DMMP recruitment would be expected to be minimal.

We can also observe clear trends in DMMP binding by examining the variations in the thiourea catalysts. Upon removal of the electron withdrawing CF_3 groups, an increase in the energy of the bound complex by approximately 1.5 kcal/mol was seen due to the unfluorinated system's ability to form only one hydrogen bond to the DMMP oxo-group. When the 2-pyridyl R-group is compared, the formation of the bound complex becomes energetically less favorable by roughly 6 kcal/mol. This increase in energy can be attributed to the introduction of the large R-groups, resulting in both steric repulsion and shielding of the DMMP complex from the stabilizing influence of the polar solvent. A further 4.5 and 5.9 kcal/mol free energy penalty for DMMP binding was also observed for the direct attack pathways of the 2-pyridyl and 2-phenol R-groups respectively, which illustrates the stabilizing impact of the incorporation of a bound water molecule and the role it plays in facilitating complex formation.

The central question of catalytic activity revolves around the predicted free energies of activation relative to the lowest free energy state. When these energies are examined

for pathway 1 hydrolysis mechanisms, we find that they span a fairly narrow range of 22.3-25.7 kcal/mol. This range may be compared to a free energy of activation of 22.3 kcal/mol for the TEA general-base catalysis reference system. Thus, there is *no* lowering of the energetic barrier accomplished by any of these catalysts. However, if the free energies are compared directly to the separated reactants, we find that the energy of the TS is lowered by approximately 1-3 kcal/mol for pathway 1 for all thiourea-methyl mechanisms. However, no increase in reaction rates is associated with this transition state stabilization as the strong hydrogen bonding has a greater lowering of the free energies of the bound complexes, resulting in a net elevation of the energetic barriers.

Interestingly, the unfluorinated thiourea-methyl catalyst possesses the lowest free energy barrier for nucleophilic water attack. In this instance, we see the formation of a single hydrogen bond in the pre-reactive complex, while two hydrogen bonds are formed in the TS structure, as there is a build up of charge in the DMMP molecule. These energies illustrate that increased catalytic activity can be provided by tuning catalyst electronegativity to loosely bind the starting complex and tightly coordinate to the transition state structure. However, the magnitude of the energetic discrimination provided by the change in hydrogen bonding between the two structures for the unflourinated catalyst was predicted to be fairly low.

Evaluating the predicted activation energies for pathway 2, we find the free energy barriers for all catalysts to lay between 19.0 and 22.2 kcal/mol as compared to 19.2 kcal/mol for the TEA catalyzed hydrolysis. This trend is analogous to that associated with pathway 1, including the observation that the unfluorinated thiourea catalyst shows a

decrease in the transition state energy to 15.7 kcal/mol relative to separated reactants, but this low free energy barrier is again offset by the equal energetic lowering of the bound starting complex. Importantly, the studied catalysts fail to have a significant impact on the difference in energy barriers between pathways 1 and 2, as pathway 2 remains kinetically favored for every case.

In addition to examining the energetics, the geometric parameters of the bound complexes can provide additional insight into reactivity. The P-SMe and P-OMe distances for both pathways are similar to the TEA catalyzed mechanism for all systems with the exception of the direct attack by pyridine. In addition, the newly formed P-OH bond distance in the intermediate structures is also in good agreement with the TEA catalyzed pathway 1 and 2 complexes. This illustrates that all systems that proceed via water activation differ only by the binding of substrate complex, with little variation in the reactive sub-unit itself. This further supports the lack of major energetic changes for either pathway.

Investigation of direct nucleophilic attacks upon DMMP by catalyst subunits indicates that such pathways are energetically demanding. A large free energy penalty is paid for the unfavorable coordination of DMMP without the stabilizing influence of a polar water molecule in the coordination site. The bulky nature of these ligands also introduces destabilizing steric interactions. Finally, it appears that the formation of a P-N bond is unfavorable, restricting the choice of catalytic nucleophiles. Although, the use of oxygen based nucleophiles may produce energetically feasible pathways.

In summary, none of the systems investigated significantly catalyzed the P-S bond hydrolysis pathway 1, nor did they significantly improve the relative energies of the P-S hydrolysis pathway compared to that of P-O hydrolysis pathway 2. While some catalysts can capture DMMP with favorable free energies through hydrogen bonding, few of these systems preferentially stabilize the transition state geometries. Given these observations, it appears that hydrogen bonding through the catalytic backbone can be best utilized for binding DMMP, but this additional coordination does a poor job at enhancement of catalytic activity and improving pathway selectivity. In order to increase reaction rates and selectivity, R-groups need to be chosen for their ability to stabilize thiol-leaving groups over alcohol ones, likely based on supporting more diffuse charge concentrations in the position opposite the catalytic nucleophile. An additional possibility would be to design catalysts that stabilize the formation of the trigonal bipyramidal intermediate and to insure that the elimination from such intermediates favors the cleavage of the P-S bond.

This work helps establish a baseline for future studies of catalytic hydrolysis of VX, specifically by identifying the dominant conformers of VX and DMMP in solution. We also demonstrate that the thiourea backbone possesses the most effective binding of the pre-reactive complex, making a good starting point for future catalyst development. In addition, the computational protocol we developed should be efficient and accurate for future modeling studies aimed at aiding catalyst design.

Chapter 3. Mechanistic Analysis of Water Oxidation Catalyzed by Mononuclear Copper in Aqueous Bicarbonate Solutions

3.1. Introduction

Production of hydrogen gas from the oxidation of water generates a green fuel, potentially through the exploitation green sources of oxidizing power, and this process is now the subject of considerable research activity.[85-93] Many transition-metal-based homogeneous catalysts for water oxidation have been reported, especially those incorporating Ir[94-98] and Ru.[99-113] Reports of homogeneous catalysts based on more earth-abundant metals,[114-116] e.g., Mn,[117-120] Co,[121-135] Fe,[136-141] and Cu,[44,142-144] have also recently begun to appear. High turn-over frequencies have been reported for several robust copper-based catalysts active predominantly at high pH and for high over-potentials, but detailed mechanisms for the observed oxidation of water in these systems has not yet been established.

The recent work by Chen & Meyer stands out as they report the ability of Cu(II) salts to robustly catalyze water oxidation at fast turn-over frequencies under an external potential in a solution of carbonate at pHs of 6.7, 8.2 and 10.8.[44] Most importantly, these solutions demonstrate unique reactivity under each of these conditions. At the basic pH of 10.8 this catalytic system demonstrates an onset of oxidation at 1.05 V and a catalytic peak at 1.46 V with a large current indicating the rapid catalytic production of O_2. In addition, this catalyst demonstrates a second order dependence on the copper concentration, indicating the possible formation of a catalytic dimer unit. However, it

should be noted that under these conditions the formation of an oxidized film upon the electrode indicates the possibility of heterogeneous catalysis.

Upon the reduction of the pH to 8.2, the cyclic voltammetry (CV) results begin to demonstrate a dependence upon both the copper concentration and the scan rate. At [Cu(II)] greater than 5mM and the use of slow scan rates, features similar to those seen for the basic solution are observed with an onset of oxidation at ~1.3 V, which may be analogous to the oxidation behavior seen at a pH of 10.8, though a difference in the UV-Vis spectrum of the potential-free solution indicates the presence of a new ground-state species. In addition, the catalytic wave at 1.55 V demonstrates a second order dependence upon copper concentration and produces similar turn-over frequencies, which point to an analagous water oxidation mechanism, including the possible formation of a dimeric species on or near the electrode surface.

This reactivity stands in contrast to that observed at a pH of 8.2 for low copper concentrations or fast scan rates. Under these conditions the catalytic wave at 1.55 V disappears and an oxidation peak at ~1.8 V emerges with a first order dependence of the catalytic activity upon the concentration of copper, though under intermediate conditions both oxidation peaks are present. This system also lacks the formation of a copper containing film upon the electrode surface, which indicates the likely formation of a homogenous catalyst with a single copper center. This preference for first order catalysis under fast scan rates may be explained by a kinetic limitation for the formation of the dimeric species at this pH, indicating that monomeric species are likely present as both the starting material and the catalytic active species.

At the neutral pH of 6.7, the onset of oxidation is predicted to occur at ~1.4 V with the peak of the catalytic wave appearing at 1.65 V. This oxidation peak also demonstrates first order kinetics with respect to copper concentration and as such can be compared to monomeric catalysis at a pH of 8.2. It is important to note that the decrease in the oxidation potential with the lowering of the pH indicates a change in the identity of the oxidation reaction. However, the possible relationship of these two water oxidation mechanisms, besides a shared monomeric catalytic form, is unknown.

These experimental results demonstrate a cheap and robust catalytic system that exhibits multiple reactive pathways that can generate molecular oxygen with rapid turnover frequencies, although at the cost of an 800-900 mV overpotenital. However, due to the experimental conditions, little is known about the identity of the starting materials, their oxidation products, or the mechanism of O-O bond formation. In order to make educated improvements to the catalytic activity of these systems, the identity of all of these species needs to be elucidated. Through the use of computational methods we have been able to propose possible starting materials and monomeric reaction pathways consistent with experimental results.

3.2. Computational Methods

Calculations were performed using density functional theory (DFT) in the form of the M11-L[145] density functional with comparisons made using the B3LYP[22] density functional and an adjusted form of B3LYP with 15% Hartree-Fock exchange, which will be referred to hereafter as B3LYP*.[146] To correct for a poor description of dispersion

interactions, B3LYP was modified with the Grimme D2 empirical dispersion term.[33] All density functionals used a basis set consisting of the Stuttgart pseudopotential[147] for copper, augmented with 3 f functions with the exponents of 5.10, 1.275, and 0.32, and the 6-311+G(d,p)[80] basis set was implemented for all other atom types. All structures were fully optimized accounting for aqueous solvation effects using the SMD continuum solvent model.[81] Following optimization, intrinsic reaction coordinate (IRC) calculations were performed to verify transition states, and frequency calculations were undertaken to determine the Gibbs free energy of all structures, with a replacement of all frequencies less than 50 cm^{-1}. Adsorption spectra were calculated using time-dependent (TD) DFT, and all calculations were performed with the Gaussian09 software package.[84]

For reactions in solution, unless noted otherwise, free energy values were adjusted to refer to a 1 M standard-state concentration for all aqueous chemical species other than water through the introduction of an RTln(24.5) adjusting factor, which translates to a correction of 1.9 kcal/mol at 298 K. Additionally, the free energy of water molecules was adjusted to reflect a 55.56 M concentration corresponding to a bulk water density. This correction was performed through the use of an additional 2.38 kcal/mol free energy term.[148] For the computation of free energies associated with protonation/deprotonation processes, the experimental proton solvation of 264.0 kcal/mol was used, establishing a 1M H^+ concentration.[149,150] These free energies were also converted to the more experimentally relevant pK_a values using the equation:

$$pK_a = \frac{\Delta G_{aq}}{RT\ln(10)}$$

where ΔG_{aq} refers to the standard state free energy of the deprotonation reaction:

$$AH_{(aq)} \rightarrow A^-_{(aq)} + H^+_{(aq)}$$

where AH is an acid, A^- is the conjugate base, H^+ is a free proton in solution and all concentrations are taken to be 1M.[151,152] Free energies of reactions involving protons were also examined through the introduction a pH*1.36 kcal/mol term. This correction can allow for the investigation of reaction energies at a pH greater than 0.

It is also possible to evaluate electrochemical reactions of the form:

$$O_{(aq)} + n_e e^-_{(g)} + n_p H^+ \rightarrow R_{(aq)}$$

where O is the oxidized species, R is the reduced species, n_e is the number of electrons being transferred and n_p is the number of protons transferred. The standard state reduction potential of this class of reactions ($E^o_{O|R}$) can be calculated using the equation:

$$E^o_{O|R} = -\frac{\Delta G^o_{O|R} - \Delta G^o_{SHE}}{n_e F}$$

where $\Delta G^o_{O|R}$ is the standard state free energy of the redox reaction, F is the Faraday constant and ΔG^o_{SHE} is the free energy of the normal hydrogen electrode, which has been theoretically validated as 4.28 eV.[153-155] An additional n_p*pH*0.0591V term can be added to the potential to account for a pH greater than 0.

3.3. Results and Discussion

3.3.1. Copper-Carbonate Speciation

The first step in identifying the water oxidation mechanism of Cu(II) systems as characterized by CV was to identify the copper complexes present in a solution under no external potential. A suite of possible complexes was generated and the species most

likely to form at 1M $[HCO_3]^{1-}$ and a pH between 5 and 12 were characterized, in agreement with experimental water oxidation conditions.[44] For this range of pH conditions, three ground state species were identified (Figure 3.1), all of which demonstrated a planar geometry with no coordination of axial solvent molecules, as the axial coordination was predicted to be so weak that solvent effects were best accounted for using an implicit solvent model.

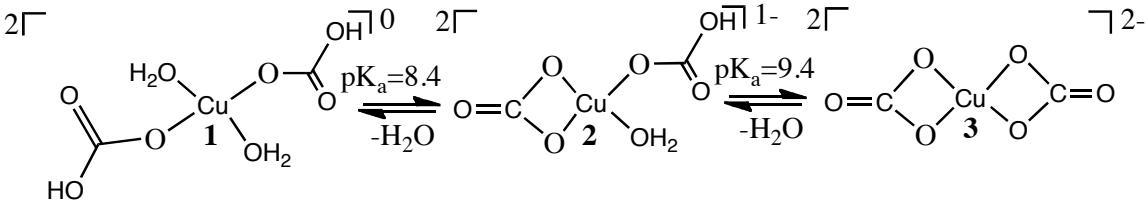

Figure 3.1. The most stable complexes present in a 1M $[HCO_3]^{-1}$ solution over a pH range of 5-12. Charges and spin multiplicities for all species are indicated at the upper right and upper left of structures, respectively.

Theory predicts the bis-monodentate bicarbonate species **1** to dominate below a pH of 8.4, the mixed mono-bicarbonate and bidentate-carbonate compound **2** in the narrow pH range of 8.4 to 9.4, and the bis-bidentate carbonate complex **3** to dominate at a pH above 9.4. These predictions are in fairly good agreement with electron spin-echo envelope modulation experiments that found analogous species in 14 K frozen solutions of copper in aqueous bicarbonate at pH values of 5.5, 6.5, and 8.0 to exhibit all monodentate, some bidentate, and bis-bidentate anion coordination, respectively.[156] Given the uncertainties associated with comparing frozen and liquid samples, we

consider this agreement to contribute acceptably to the validation of the description of equilibrium speciation in aqueous bicarbonate solutions.

In addition to verifying the identity of the equilibrium form of the copper complexes at the experimental pH conditions, it is also important to establish the rates of formation for these complexes, as water oxidation activity may proceed through a minority species. As such, the conversion pathways between species were examined and a mechanism determined where direct deprotonation of a bicarbonate ligand on **1** can occur with a pK_a of 12.4, corresponding to an endothermic energy of 5.7 kcal/mol at the experimentally studied pH of 8.2 (Figure 3.2). Once the deprotonated species **1a** is formed, an aqua-ligand can rotate away from the copper center coupled with the concomitant formation of a second Cu-O bond to the carbonate group. This concerted mechanism can occur with a low stepwise energy barrier of 0.6 kcal/mol, which translates to a reasonable global free energy of 6.3 kcal/mol at a pH of 8.2 or 8.3 kcal/mol at pH of 6.7. These favorable energetics indicate that we can expect both species to be accessible even at low pH conditions, though the formation of **2** may be slowed by a decrease in pH.

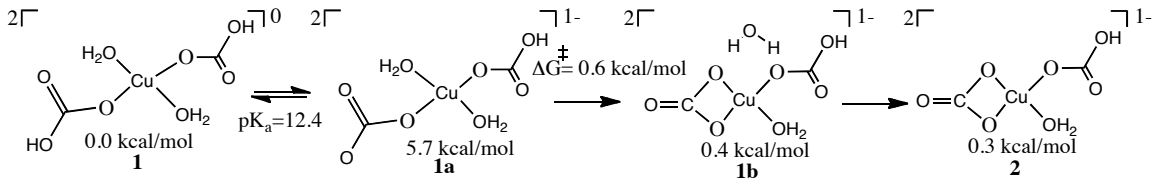

Figure 3.2. A mechanism for the possible conversion of **1** to **2** via bicarbonate deprotonation and the ejection of a water molecule. All energies are reported with respect to **1** for pH=8.2 and free energies of activation are given for individual

microscopic steps. Charges and spin multiplicities for all species are indicated at the upper right and upper left of structures, respectively.

The kinetic availability of **3** was also examined and a feasible mechanism for its formation was determined (Figure 3.3). The transformation of **2** to **3** occurs in a very similar manner to the generation of **2**, with the deprotonation of the remaining bicarbonate ligand occurring at a similar pK_a of 12.9, corresponding to a thermodynamically unfavorable energy of 6.7 kcal/mol at a pH of 8.2. Again, the aqua-group is predicted to leave during the concerted formation of a Cu-O bond to the newly formed carbonate ligand. This bond formation step is predicted to proceed with a low stepwise energy of 1.8 kcal/mol; however, this transition state possesses a global free energy barrier of 8.5 kcal/mol at a pH of 8.2 or 12.5 kcal/mol at a pH of 6.7. These energies indicate that while formation of **3** is possible at a neutral pH, the generation of the exclusively bidentate complex may only occur at sufficiently slow CV scan rates.

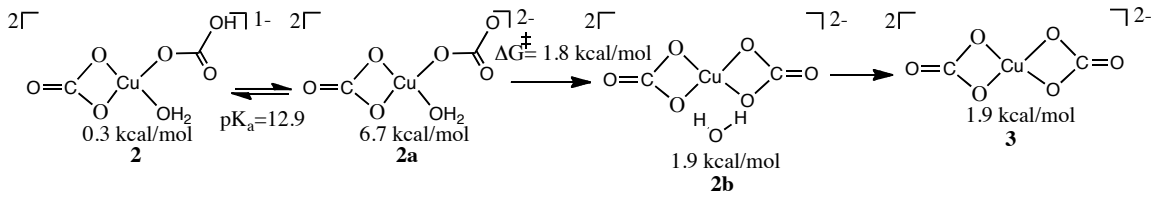

Figure 3.3. A mechanism for the conversion of **2** to **3** via bicarbonate deprotonation and the ejection of a water molecule. All energies are reported with respect to **1** for a pH of 8.2 and free energies of activation are given for individual microscopic steps. Charges and spin multiplicities for all species are indicated at the upper right and upper left of structures, respectively.

In an effort to verify the accuracy of the M11-L energies for the conversion of **1** to **3**, single-point calculations were performed using B3LYP, B3LYP-D2, and B3LYP*, which has recently been verified for its accuracy in modeling water oxidation reactions (Figure 3.4).[157] B3LYP-D2 and M11-L possessed good agreement for the energies of **1**, **2**, and **3**, however both B3LYP and B3LYP* predicted **3** to be the thermodynamically favored species for all experimentally considered conditions. However, examining the elementary reaction steps provided additional insight into the strengths and weaknesses of all the possible density functional methods.

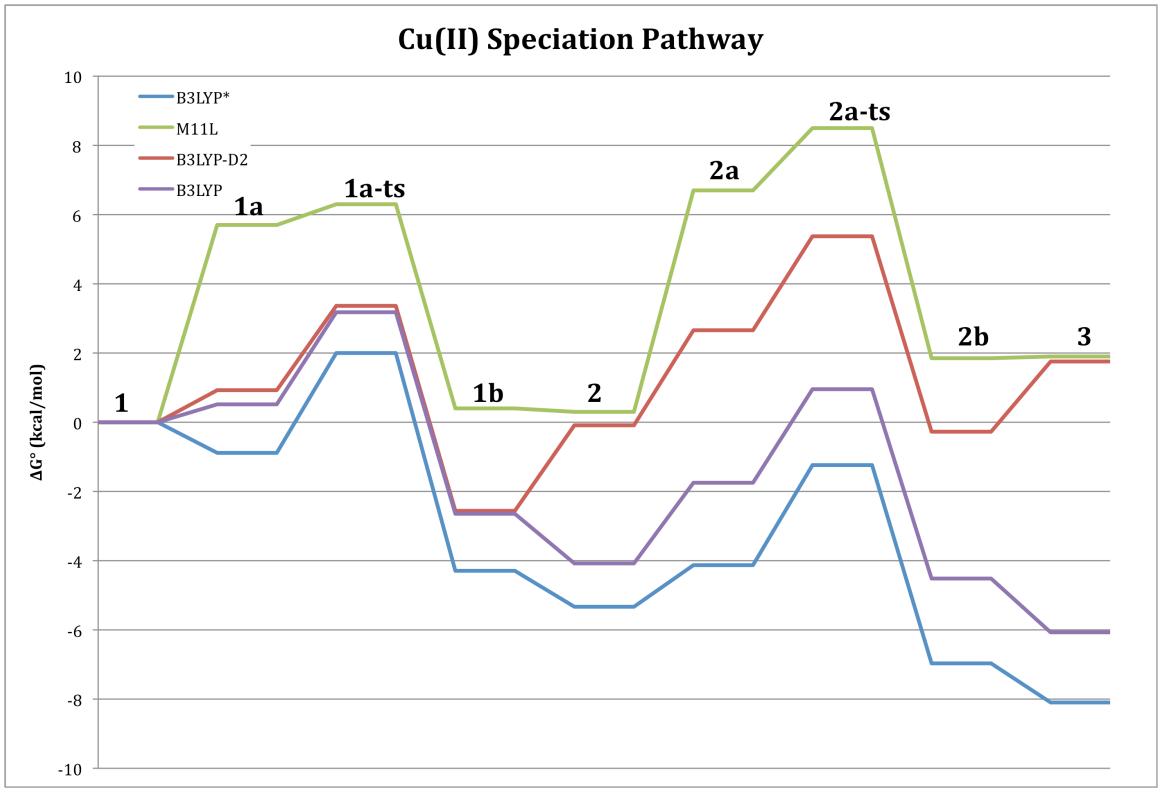

Figure 3.4. Energies for the reactivity of Cu(II) complexes at pH=8.2 calculated using single point energies for multiple density functionals.

It is important to note that the three B3LYP functionals differ from each other only in their predictions for the energies of the deprotonation steps and the release of the explicit water molecules. The predicted pK_a values of the bicarbonate ligands differ systematically with M11-L>>B3LYP-D2>B3LYP>B3LYP*, resulting in B3LYP* stabilizing the deprotonated structures by over 5 kcal/mol as compared to M11-L. This behavior indicates that the inclusion of non-local Hartree-Fock and dispersion corrections help stabilize the protonated system. In a similar manner B3LYP and B3LYP* predict a favorable release of explicit water molecules, indicating a large entropic cost for the inclusion of water into the reactive complex. In contrast, B3LYP-D2 predicts the inclusion of explicit water molecules to lower the free energy of the complex, indicating that in order to make a balanced comparison of energies across species, explicit solvation of all complexes may need to be considered. When analyzed as a whole, the energy differences indicate that M11-L is the most accurate choice of density functional as B3LYP and B3LYP* tend to over-predict the stability of the deprotonated structures and a more complete explicit solvation sphere needs to be considered to properly address the accuracy of B3LYP-D2.

As the possible starting complexes possess very similar free energies, TD-DFT calculations were performed for compounds **1**, **2**, and **3** using M11-L, B3LYP*, and B3LYP and were compared to experimental UV-vis data obtained at multiple pH conditions in order to clarify the identity of the starting materials (Table 3.1). The M11-L results predicted a single absorption peak at 580 nm for the neutral compound **3** with a red-shift in the predicted spectra by 22 nm upon the formation of the negatively charged

2. However, upon the formation of **1,** a 40 nm blue-shift is predicted in disagreement with experimental results, though this discrepancy may be due to a poor description of strong interactions with the solvation sphere. Furthermore, a systematic 100-200nm blue-shift is predicted for all M11-L results when compared to the experimental spectrum. Though when all structures are considered, the experimental red-shift of ~30-50 nm is best supported by a dominance of **2** at a low pH and **3** at a high pH. Though these predicted spectra should be taken cautiously as M11-L has been demonstrated to do a poor job predicting excitation energies.[158]

Table 3.1. Predicted absorbance peaks for **1**, **2**, and **3** and comparison to the experimental spectra for pH's 6.7, 8.2 and 10.8.

Method	Complex 1	Complex 2	Complex 3
M11-L	542 nm	602 nm	580 nm
B3LYP*	681-557nm	564-493 nm	524-457 nm
B3LYP	701-567 nm	584-506 nm	540-470 nm
pH	6.7	8.2	10.8
EXP	~760	~740	~710

Additional TD-DFT calculations were performed utilizing B3LYP and B3LYP*, with both functionals producing similar results, though B3LYP* predicted all peaks to be blue-shifted by ~20 nm due to the lower percent of Hartree-Fock exchange included, and both functionals demonstrated a systematic blue-shift of 100-200nm when compared to the experimental data. The most notable feature of the B3LYP results was the prediction of four adsorption peaks for all complexes, which would result in a broad adsorbance spectrum. However, shifts for the calculated absorbances compare well to the

experimental values, with the average absorbance peak for **2** predicted to possess a ~30 nm red-shift compared to **3**, corresponding well to the experimental decrease of the pH from 10.8 to 8.2. In contrast, the average absorbance peak for the theoretical predictions of **1** is red-shifted by ~114 nm and predicts significant broadening of the absorbance range, neither of which is observed for the experimental UV-vis spectra.

It is important to note the consistent prediction of ~30 nm redshift in the absorbance peak of **2** relative to complex **3**. Coupled with the wildly varying theoretical predictions for the absorbance spectra of **1**, this UV-vis data indicates the possibility that **2** may be the dominant species in the pH range of 6.7 to 8.2. Though when accounting for a lack of agreement on the theoretical spectra of **1**, the range of error possible in the TD-DFT results, and the accuracy of the calculated pH of equilibrium, the possible presence of either **1** or **2** for the pH range of 6.7-8.2 must be considered.

3.3.2. Oxidation Pathways

With an established set of possible compounds present in a potential free environment, the next step was to study the oxidation of each of these three complexes. It was assumed that the direct oxidation products involved only the loss of protons, with no recruitment of solvent molecules or formation new Cu-O bonds. Under these assumptions, complexes **1-3** all yield very different oxidation pathways and, using the M11-L density functional, a speciation diagram was constructed to describe the formation of the most stable direct-oxidation products (Figure 3.5).

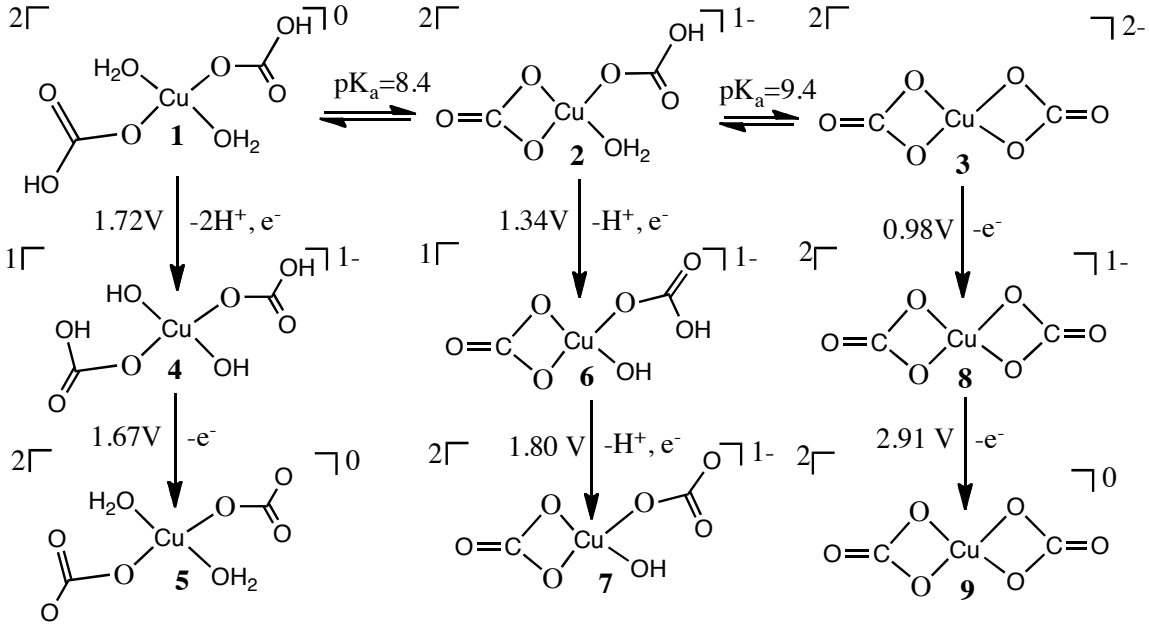

Figure 3.5. Compounds relevant to initial oxidation steps in copper-bicarbonate catalyzed water splitting. Voltages vs. the normal hydrogen electrode (NHE) are provided for elementary steps at pH = 8.2. Charges and spin multiplicities for all species are indicated at upper right and upper left of structures, respectively.

The bicarbonate-based compound **1** was found to undergo a difficult $1e^-/2H^+$ proton coupled electron transfer (PCET) to generate **4**, which contains a closed-shell singlet d^8 Cu(III) center. The formation of this complex involves the deprotonation of both bicarbonate groups and a simultaneous proton transfer from each of the two aqua groups to the carbonate ligands. With a requisite potential of 1.90 V for its formation at a pH of 6.7, complex **4** is an unlikely candidate for the experimental oxidation peak at 1.65 V under neutral conditions.

However, a second one-electron oxidation of **4** can occur with a requisite potential of 1.67 V to form **5**. This oxidation step involves the simultaneous transfer of a proton from each of the bicarbonate ligands to each bound hydroxo group. Complex **5** is also unique in that it possesses unpaired electron spin density delocalized over both carbonate ligands coupled anti-ferromagnetically to a doublet copper center. This indicates that the carbonate substituents play a role as non-innocent ligands and that they likely possess reactive radical character. Furthermore, the low energy of this complex with respect to **4** indicates that the most likely pathway for the formation of **5** is a via a $2H^+/2e^-$ PCET reaction from complex **1** that can proceed at a potential of 1.76 V at a pH of 6.7, in good agreement with the experimental catalytic wave at 1.65 V. Formation of **5** should remain possible at a pH of 8.2 with oxidation of **1** occurring at a potential of 1.69 V, within the realm of where mononuclear water oxidation is known to occur.

It is also important to examine the oxidation of the mixed-coordination complex **2**, as the energetics and TD-DFT results favor it as a possible ground-state species at a pH of 6.7 or 8.2. The single-electron oxidation of **2** is predicted to feature the deprotonation of the bicarbonate ligand, which will allow a proton transfer from the bound aqua-group to the newly generated carbonate ligand resulting in the stable complex **6,** which possesses the singlet electronic structure characteristic of a Cu(III) center. This oxidation is predicted to occur at the relatively low potential of 1.34 V for a pH of 8.2, establishing it as a likely candidate for the experimental onset of oxidation at ~1.3 V for this pH. This favorable energy also indicates **6** as a possible intermediate for both first- and second-order water oxidation at a pH of 8.2.

The most likely candidate for direct oxidation of **6** features a PCET reaction occurring at the bicarbonate ligand to result in the product species **7**. This ligand deprotonation causes the resulting carbonate group to rotate out of the plane, leading to the plane of the ligand lying perpendicular to the plane of copper coordination. This rotation of the carbonate group may be due to the generation of unpaired spin density localized on the monodentate carbonate ligand, indicating its possible oxidation to produce radical character in a similar fashion to that seen for the generation of **5**. The oxidative formation of **7** from **6** is predicted to occur at the potential of 1.80 V for a pH of 8.2, providing a possible explanation for the first-order catalytic wave at high potentials, though this high potential indicates that direct formation of **7** does not occur at the neutral pH of 6.7.

Finally, to address possible reactivity at a pH of 10.8, the oxidation products of complex **3** were also examined. A simple one-electron oxidation of **3** is predicted to produce the stable closed-shell singlet compound **8** at the low potential of 0.98 V. This theoretical potential may correspond to the experimental onset of oxidation behavior at a potential of 1.05 V. However, further oxidation of this species is unlikely to occur, due to the requisite potential of 2.91 V to form the product compound **9**, which is well outside the range of feasible oxidation potentials. With a lack of monomeric oxidation products it is assumed that complex **8** will undergo dimerization on the electrode surface to form a reactive species that can catalyze water oxidation at a potential of 1.46 V.

3.3.3. Rearrangements of Oxidized Species

It should be noted that these direct oxidation products can undergo further reactivity to form stable oxidized complexes, which may demonstrate catalytic activity. When considering the formation of possible reactive species it is important to note that the products need to be both thermodynamically favored and kinetically accessible. This is especially true for the case of copper-bicarbonate water oxidation, where the catalytic behavior has been demonstrated to depend on CV scan rate. As such, favorable oxidized products were identified and the kinetics for their formation under the range of experimentally observed conditions was assessed.

3.3.3.1. Thermodynamically Favored Products

With this thought in mind, a full survey of possible homogenous complexes was undertaken and a theoretical pourbaix diagram was constructed for an experimentally relevant range of potentials and pH conditions (Figure 3.6). This representation shows the most thermodynamically favored complex for a given set of conditions without accounting for kinetically limiting factors. This set of complexes includes changes in the coordination sphere of the copper center, which do not occur for a ground-state Cu(II) species. Specifically, under external potentials the formation of complexes with octahedral coordination of three carbonate ligands becomes favored (Figure 3.7). By comparing this equilibrium speciation to the experimental results we can help determine the availability of these structures.

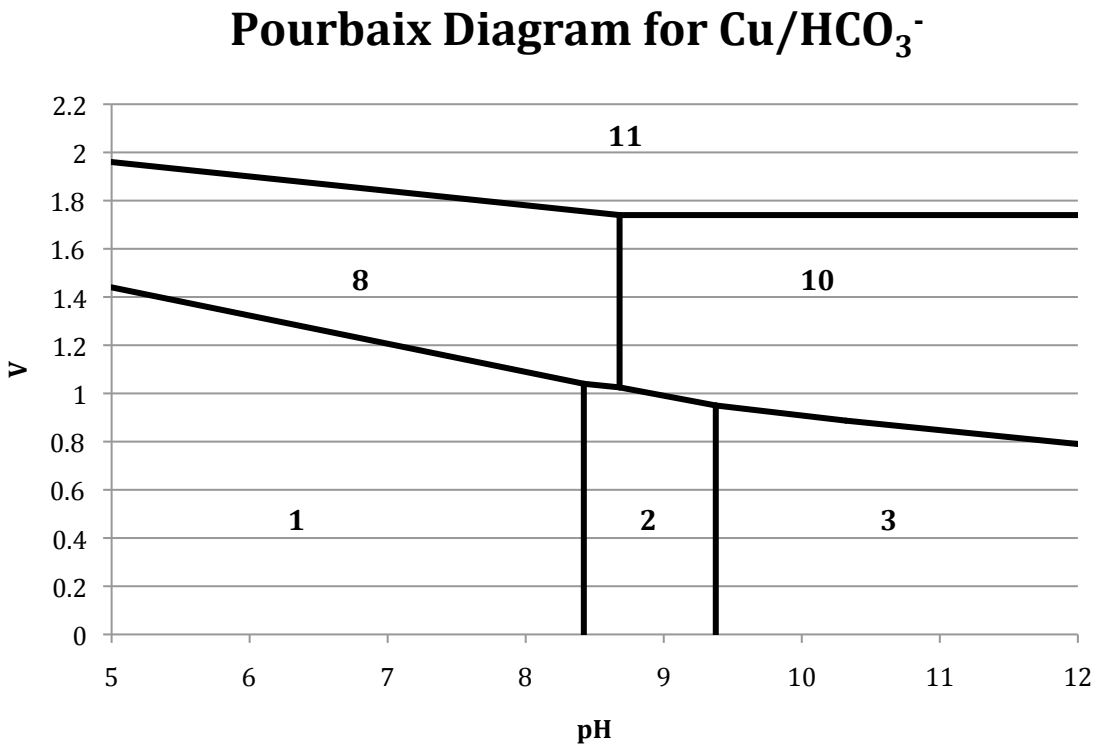

Figure 3.6. Theoretical pourbaix diagram of homogenous copper complexes in a 1 M bicarbonate solution over a range of experimentally observed potentials and pH values.

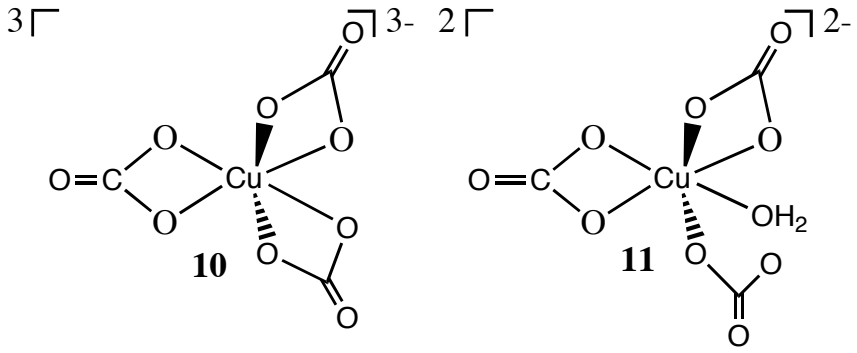

Figure 3.7. Thermodynamically accessible tri-carbonate copper complexes. Charges and spin multiplicities for all species are indicated at the upper right and upper left of structures, respectively.

This examination of the thermodynamically dominant compounds reveals that under low pH conditions complex **8** is predicted to be the most stable one-electron oxidized species and may form under an external potential of 1.24 V at a pH of 6.7 or 1.06 V at a pH of 8.2. Though it is worth noting that experimentally no oxidation peaks were observed at these low potentials and that kinetic factors likely prevent oxidation from occurring. Specifically, the oxidative generation of **8** is expected to be rate limited by the generation of the precursor complex **3** with significant free energy barriers of formation at neutral pH conditions as examined in detail in sections 3.3.1 and 3.3.3.2.

At a pH higher than 8.7 the dominant one-electron oxidized species is predicted to switch from the square planar complex **8** to the octahedral **10**. This change in the preference of copper coordination is related to a change in the spin state of the copper center. While a singlet Cu(III) metal center favors a square-planar coordination sphere such as those found in **4**, **6**, and **8**, by the adoption of a triplet electronic structure the coordination of axial ligands becomes feasible. The formation of these triplet species occurs in a less direct mechanism than is predicted for the generation of the singlet copper species, as no stable octahedral Cu(II) complexes have been identified. As a result, the formation of an octahedral compound by direct oxidation is impractical and the likely precursor for the generation of complex **10** is instead **8**, which may be able to undergo a spin transformation to form a distorted see-saw triplet complex with an endothermic energy of 6.2 kcal/mol, which can then recruit a carbonate molecule from solution to form **10**. These limitations to the formation of this triplet Cu(III) complex illustrates that despite the fact that compound **10** is predicted as the most stable species at

a pH of 10.8 and a potential as low as 0.89 V, the formation of **10** is unlikely to occur until a precursor singlet Cu(III) complex can be formed.

In a similar manner, the most stable two-electron oxidized complex (**11)** is an octahedral species, which is not predicted to form via direct oxidation from a precursor planar complex. This species is also unique in that it contains a single unpaired electron localized on the copper center, which indicates the absence of oxidation of the carbonate ligands and the formation of a "true" Cu(IV) center. This highly oxidized copper center is likely stabilized by the presence of three charged carbonate ligands, but unlike the Cu(III) center in **10**, the coordination of three bidentate ligands is predicted as unstable. Instead, one carbonate ligand retains monodentate coordination to the copper center and forms a hydrogen bond to an aqua-group that is recruited at the open metal site. This difference in coordination may be attributed to the tight bite angle of carbonate ligands and the need for monodentate ligands that can better adapt to the needs of the Cu(IV) coordination sphere.

It is important to note that despite being the most stable two-electron oxidized species, **11** is only predicted to be the dominant copper complex under potentials higher than those where catalytic water oxidation has been experimentally observed. This energetic destabilization of the two-electron oxidized species can be attributed to the low free energies of **8** and **10**, which are expected to be kinetically limited and experience minimal formation under acidic and neutral conditions. Under basic conditions, no generation of monomeric two-electron oxidized species is expected, as experimental

results indicate a preferential formation of the di-nuclear catalytic species under these conditions.

In an effort to assess the possible presence of *homogenous* di-nuclear species, a thermodynamic survey of these complexes was undertaken for comparison to the monomeric species, with calculations assuming a total copper concentration of 5 mM in agreement with experimental results, allowing the identification of the most stable di-nuclear species (Figure 3.8). In the absence of an external potential, the lowest energy di-nuclear species was identified as the bis(μ-hydroxo) bridged complex **12,** which contains two square-planar Cu(II) centers ferromagnetically coupled to produce a triplet state. However, this dimeric species possesses a free energy 14.0 kcal/mol above the comparable mono-nuclear complex **3**, indicating the low likelihood of a di-nuclear species being present in a potential-free environment.

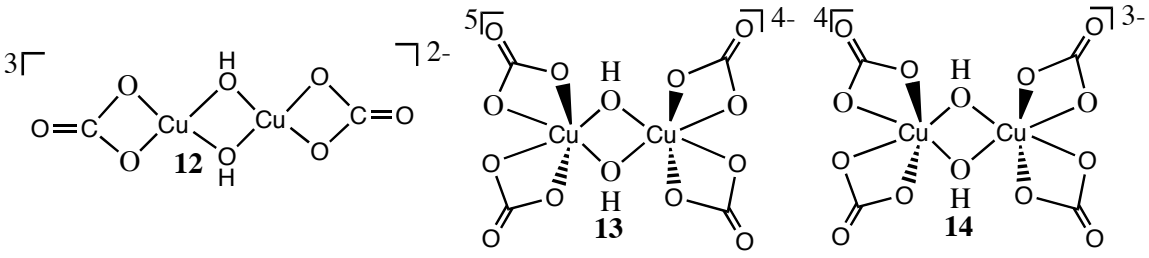

Figure 3.8. The thermodynamically most favorable homogenous di-nuclear copper complexes. Charges and spin multiplicities for all species are indicated at the upper right and upper left of structures, respectively.

In the presence of an external potential, the surveyed di-nuclear complexes also demonstrated an ability to form stable octahedral copper centers in a similar manner to the mono-nuclear case, with the lowest energy oxidized copper dimer (**13**) containing a bis(μ-hydroxo) bridge that ferromagnetically couples two triplet octahedral Cu(III) centers, with the di-nuclear complex formation likely occurring through a hydroxide initiated dimerization of the triplet analog of **8**. At the basic pH of 10.8, this oxidized dimer may be thermodynamically available with a free energy penalty of 2.1 kcal/mol with respect to two equivalents of **8**, or 7.9 kcal/mol with respect to the thermodynamic ground-state species **10**, and at a pH of 8.2, **13** possesses a free energy of 9.2 kcal/mol above the ground-state species **8**. These energies indicate the thermodynamic accessibility of **13** under this range of pH conditions. Unfortunately, no di-nuclear complexes of this oxidation state have been found to demonstrate the ability to form O-O bonds and **13** is predicted to undergo a $1e^-$ oxidation to produce the most stable 3 e^- oxidized di-nuclear species (**14**) at a potential of 1.73 V, well above the experimental oxidation peak. The energetic difficulty of both oxidation and O-O bond formation indicates that while **13** may play a key role in dimer formation, the generation of the reactive form likely takes place at the heterogenous surface, in agreement with the film formation experimentally observed for di-nuclear water oxidation.[44] This survey also demonstrates that no *homogenous* di-nuclear species is expected to be in direct thermodynamic competition with the mono-nuclear complexes under experimental conditions and as such their role in mono-nuclear water oxidation pathways is predicted to be minimal.

3.3.3.2. Kinetically Accessible Structures

The disagreement between the energies of the thermodynamically favored structures and experimental oxidation peaks illustrates the importance of considering the kinetic availability of oxidized species. These kinetic pathways need to be considered for both the availability of reduced precursor complexes and the generation of the multiple low energy product species not available via direct oxidation pathways such as **10** and **11**. Though most importantly, due to the key role that protonation of these species plays in the energetics of reactive pathways, the pH of the solution needs to be considered when evaluating possible reaction mechanisms and free energy barriers.

At the experimentally relevant pH of 6.7, the dominant candidates for oxidative products include **5**, **6**, and **8**, with thermodynamic energies for favorable formation of these species at 1.76, 1.55 and 1.24 V respectively. Though it is important to note that the oxidative formation of **6** requires the generation of the precursor **2**, whose production from the equilibrium species **1** will occur with a barrier of 7.7 kcal/mol. In a similar manner the generation of **8** will be limited by a 12.5 kcal/mol free energy barrier for the production of the precursor **3**. These energetics may limit the formation of **6** and **8** so that the oxidative generation of **5** becomes favorable under these conditions and results in the lack of oxidation peaks below 1.65 V. As such, the low potential generation of the Cu(III) complexes **6** and **8** would only be expected at slower CV scan rates.

At the experimental pH of 8.2, the dominant candidates for direct oxidative products include **5**, **6**, and **8** with thermodynamic energies for favorable formation at 1.69, 1.38 and 1.06 V respectively. At this pH, the generation of the precursor complexes **2** and **3**

possess free energy barriers of 6.3 and 8.5 kcal/mol respectively. When these values are compared to experimental oxidation peaks, the onset of oxidation at ~1.4 V indicates that the formation **6** is feasible, but that the formation of **8** is kinetically forbidden. As a result, the presence of **1** and **6** in solution indicates that the first order catalytic wave may be attributed to the oxidative formation of either **5** or **7** under experimental conditions. In addition, the availability of **6** at potentials below 1.55 V indicates that the slow scan rate requirement for second-order water oxidation may be due to the slow formation of a surface bound dinuclear complex from the monomeric precursor **6**. This dimer species is then expected to oxidize to a catalytically active form at the electrode surface at 1.55 V.

At the pH of 10.8, compound **8** is predicted to be the exclusive direct oxidation product at a potential of 1.0 V, as addressed earlier. This species is then expected to undergo dimerization at the electrode surface to form a reactive species that can be further oxidized at a potential of 1.46 V. The stable nature of **8** and possible presence of **10** causes the formation of two-electron oxidized complexes such as **11** to be unfavorable at these low potentials and as a result the formation of a reactive monomeric water oxidation catalyst is unexpected at this basic pH.

First-order water oxidation is predicted to occur solely under conditions where we expect the formation of **5** or **7**, but it has been established that these complexes are not the lowest energy two-electron oxidized species. As such, there is a clear need to identify the kinetics and reactivity of these two complexes, starting with chemical transformation of **5** into **7** (Figure 3.9). Complex **5** can release an aqua-group by cleavage of the Cu-O bond via rotation of the oxygen atom away from the copper center with a free energy barrier of

4.3 kcal/mol to generate **15**, which contains a loosely coordinated water molecule. This water molecule can then fully disassociate with an exothermic energy of 2.5 kcal to form **16**. Upon the formation of **16**, the carbonate ligand can establish a second Cu-O bond to the copper center to generate a bidentate ligand with a step-wise energy barrier of 1.7 kcal/mol and a global free energy barrier of 3.4 kcal/mol to generate **17**. This bond formation transfers the unpaired electron spin from the carbonate ligand to the metal center to form a singlet Cu(III) center and a single non-innocent carbonate ligand. With a pK_a of 2.1, the aqua-group on **17** can then be readily deprotonated to form **7** under any experimentally studied pH. With a 4.3 kcal/mol barrier and a downhill energy of 4.8 kcal/mol at a pH of 8.2, **7** can be rapidly generated from **5** under all experimental conditions in addition to the possible oxidative production of **7** from **6** at a pH of 8.2.

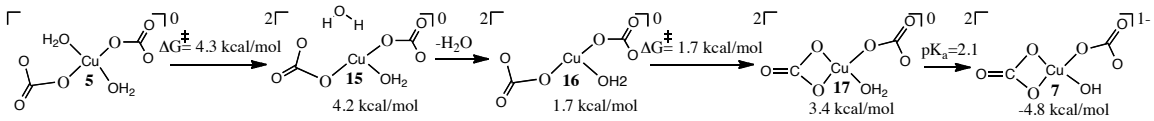

Figure 3.9. Mechanism for the conversion of **5** to **7**. All energies are given with respect to complex **5** and a pH of 8.2 with free energies of activation reported for individual microscopic steps. Charges and spin multiplicities for all species are indicated at the upper right and upper left of structures, respectively.

Complex **7** can then undergo further reactivity to form the previously identified low energy complex **11** (Figure 3.10). This transformation can occur via the monodentate carbonate ligand on **7** attacking the copper center at an open axial position with a small 3.4 kcal/mol barrier to generate **18** with a slightly endothermic energy of 1.5 kcal/mol.

This bond formation involves the transfer of electron density from the copper center to the carbonate ligand, eliminating the non-innocent character of the ligand and establishing a Cu(IV) center. Once this Cu-O bond is formed, a free bicarbonate molecule may coordinate to the copper center at the remaining free axial site to generate the energetically favored **19**. A final proton transfer from the bicarbonate ligand to the hydroxo group generates **11** with an energy 7.9 kcal/mol lower than **7** and a low 3.4 kcal/mol free energy barrier that assures the rapid generation of **11**. As a result, all monomeric water oxidation pathways should consider **11** as the energetic ground state when calculating the rates of O-O bond formation.

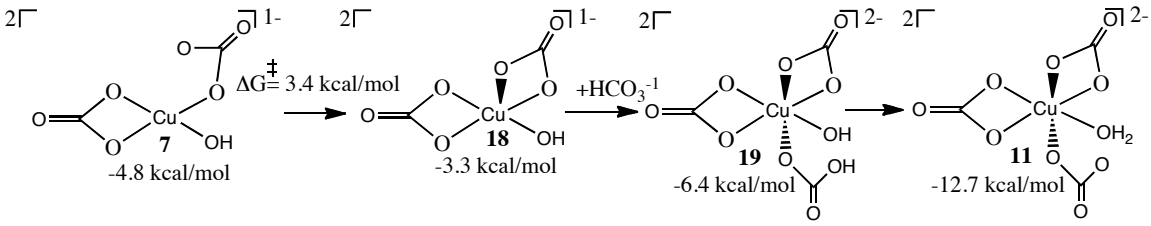

Figure 3.10. Mechanism for the conversion of **7** to **11**. All energies are given with respect to complex **5** and a pH of 8.2 with free energies of activation reported for individual microscopic steps. Charges and spin multiplicities for all species are indicated at the upper right and upper left of structures, respectively.

3.3.4. Water Oxidation Pathways

These two-electron oxidized species have been characterized as the likely candidates for mononuclear water oxidation. However, it should be noted that the formation of an O-O bond is a two-electron process, and consequently the likely product species of this

bond formation pathway will be a square-planar Cu(II) complex. As such, despite its stability, the octahedral **11** is an unlikely precursor for water oxidation and instead remains as the thermodynamic ground state structure with all thermodynamic barriers considered with respect to this species. Instead focus was placed on the reactivity of the two most stable square-planar two-electron oxidized species, the di-aqua monodenate complex **5** and the mono-aqua mixed coordination complex **7**, and their respective abilities to catalyze water oxidation.

3.3.4.1. Mono-Aqua Water Oxidation Pathways

The lowest energy square-planar complex, **7**, was the first examined for possible O-O bond formation pathways, with the most favorable mechanism proceeding through the formation of a hydrogen peroxycarbonate group (Figure 3.11). This reaction occurs through a pathway in which the radical carbonate group undergoes a coupling mechanism with the hydroxo ligand to form an O-O bond, with the excess electron density shifting to the metal center to re-establish a Cu(II) unit. This reaction proceeds with a low stepwise barrier of 7.8 kcal/mol, which translates into a global free energy barrier of 15.7 kcal/mol with respect to **11**. This radical-coupling mechanism results in the formation of **18**, which contains a hydrogen peroxycarbonate ligand and a free energy 0.4 kcal/mol lower than **11,** insuring the favorable formation of the O-O bond. The product complex **18** can then be readily deprotonated to generate the peroxycarbonate ligand found in **19** with a favorable formation for pHs above 5.1, allowing the production of this species under all available experimental conditions.

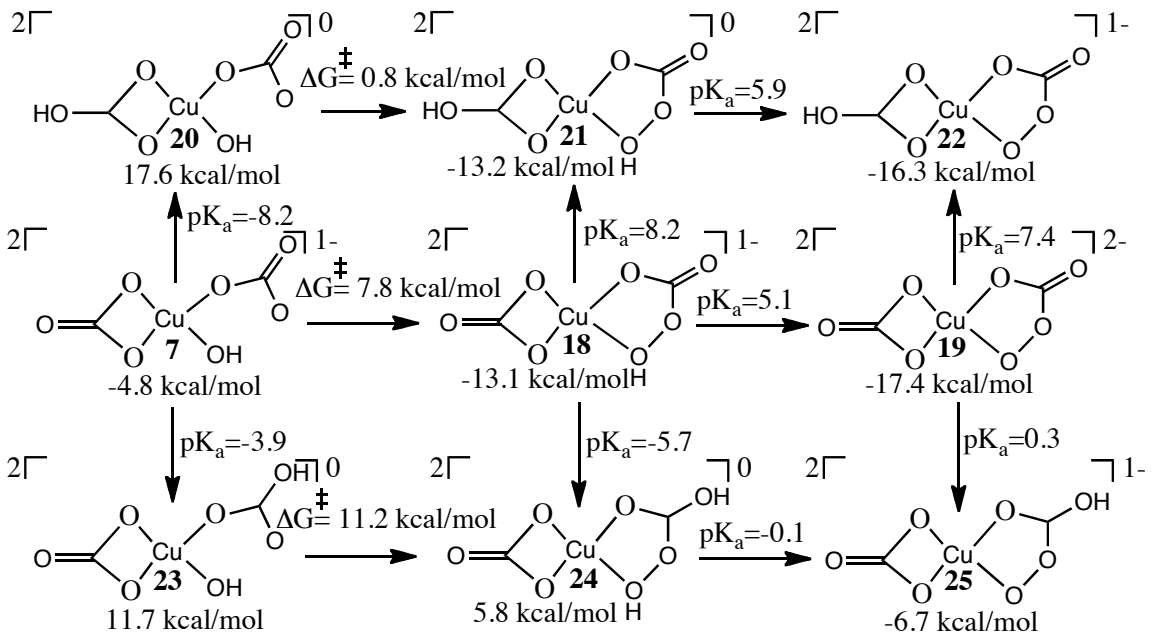

Figure 3.11. Mechanism of peroxycarbonate forming pathways using **7** and its protonated analogs, **20** and **23** as starting materials. Relative free energies are reported with respect to **5** for a pH of 8.2 with free energies of activation given for the individual microscopic steps. Charges and spin multiplicities for all species are indicated at the upper right and upper left of structures, respectively.

To examine the effect that protonation of the carbonate ligands has upon the formation of peroxycarbonates, an additional proton was added to the bidentate carbonate group of complex **7** to form **20**. The protonation of this group occurs with a low pK_a of -8.2, forbidding the formation of this complex under experimental conditions, though the subsequent generation of an O-O bond has a low energy barrier of 0.8 kcal/mol. However, the unfavorable nature of **20** raises the global free energy barrier to 30.7 kcal/mol relative to **11** at a pH of 8.2. A more feasible mechanism to produce the

resulting hydrogen peroxycarbonate complex **21** can proceed via the protonation of the carbonate analog **18** with a pK_a of 8.2, indicating the possible generation of this species under available experimental conditions. The hydrogen peroxy unit of complex **21** can then be deprotonated with a favorable pK_a to produce the peroxycarbonate ligand contained in **22**, which is predicted to be preferred at a pH of 6.7, though at a pH of 8.2 the carbonate containing analog **19** is predicted to provide the lowest energy pathway.

The alternative protonation of the available carbonate ligands in **7** places the proton upon the monodentate carbonate ligand to form **23**. However, this reaction is unlikely to occur as the formation of **23** possesses a pK_a of -3.9 and a significant global free energy barrier of 35.6 kcal/mol is associated with the formation of the O-O bond. The increase of this energetic barrier is likely due to the decreased electron availability for the formation of the O-O bond. This inactivating property of protonation is further illustrated by the unfavorable nature of the hydrogenperoxybicarbonate ligand in **24**, which possesses a pK_a of -5.7 with respect to **18**. This energetic penalty is slightly decreased for the peroxybicarbonate analog **25**, though the generation of any of these species remains unfavorable with respect to the O-O bond formation pathways of both **19** and **22**.

A final available mechanism for the formation of a peroxycarbonate ligand from **7** involves the generation of the copper-oxo complex **26** (Figure 3.12). With a pK_a of formation of 13.1, the creation of this deprotonated species is unfavorable, but a global free energy of 14.8 kcal/mol at a pH of 8.2 may allow for the formation of **26** as an intermediate. Once formed, the monodentate carbonate ligand can attack the newly generated oxo-group with an transition state energy of 4.3 kcal/mol uphill to form the

previously described complex **19**. This translates to a global free energy of 18.3 kcal/mol, indicating that the formation of the O-O bond is slightly favored for the hydroxo-containing system. This preference in pathways largely stems from the high-energy proccess of deprotonating the hydroxo-group of **7** outweighing the increased reactivity provided by the electron rich oxo-ligand.

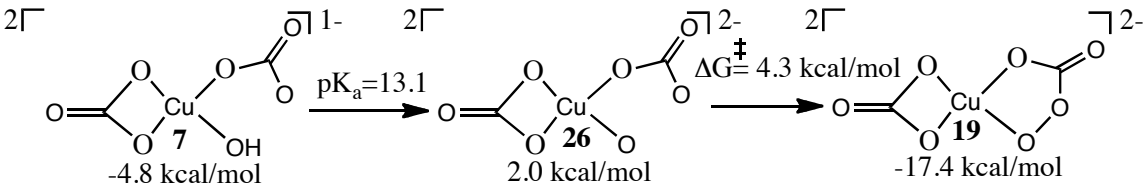

Figure 3.12. Mechanism of a peroxycarbonate forming pathway proceeding through an oxo-containing intermediate. Relative free energies are reported with respect to **5** for a pH of 8.2 and free energies of activation are given for individual microscopic steps. Charges and spin multiplicities for all species are indicated at the upper right and upper left of structures, respectively.

As the peroxycarbonate complex most likely to form at a pH of 8.2, **19** was examined for further reactivity and found to readily oxidize into a closed-shell singlet species **27** at a potential of 1.10 V (Figure 3.13). Complex **27** can best be described as a Cu(III) peroxycarbonate product, and no pathway for the cleavage of the C-O peroxycarbonate bond was discovered for this species. However, conversion to the triplet species **28** is energetically feasible with a S-T splitting of 3.7 kcal/mol, where analysis of the spin density indicates the formation of a Cu(II) doublet center coupled

ferromagnetically to an unpaired electron delocalized over the peroxy substituent, with this non-innocent ligand character allowing for further reactivity. Additionally, the possible reduction of the reactive **28** may also explain a re-reduction peak seen experimentally at ~1.25 V at fast scan rates, as eirther **27** or **28** may persist with short lifetimes in solution.[44]

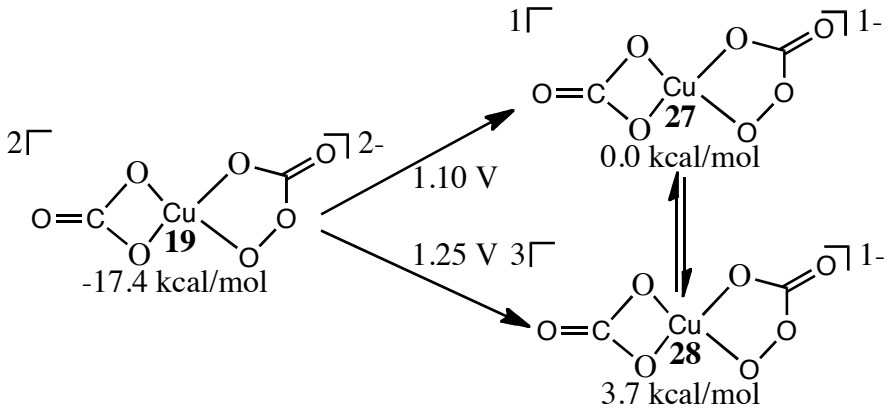

Figure 3.13. Mechanism for the possible oxidation of **19** into a singlet or triplet species with possible subsequent interconversion. The energies for two- and three-electron oxidized species are given with respect to **5** and **27** respectively with all energies assuming a pH of 8.2, and voltages vs. NHE are provided for elementary steps. Charges and spin multiplicities for all species are indicated at the upper right and upper left of structures, respectively.

The formation of the reactive triplet complex **28** allows for a retro-cyclization reaction characterized by the simultaneous cleavage of a Cu-O and C-O bond, resulting in the elimination of CO_2 with a mild free energy barrier of 3.4 kcal/mol (Figure 3.14).

However, the transition state possesses a global free energy barrier of 7.1 kcal/mol when compared to **27** and would account for **27** or **28** persisting over short time scales. The resulting product of this retro-cyclization reaction contains a CO_2 molecule over 2.9 Å distant from the copper center, indicating its complete release. The favorable ejection of this CO_2 group is further illustrated by the fact that upon the removal of the carbon dioxide molecule from the explicit solvation shell, the complex is stabilized by a further 11.7 kcal/mol due to a preferred interaction with the implicit solvent. This remaining complex can best be described as a doublet Cu(II) center ferromagnetically coupled to a superoxo-radical ligand as indicated by the spin-density calculated for both **29** and **30**.

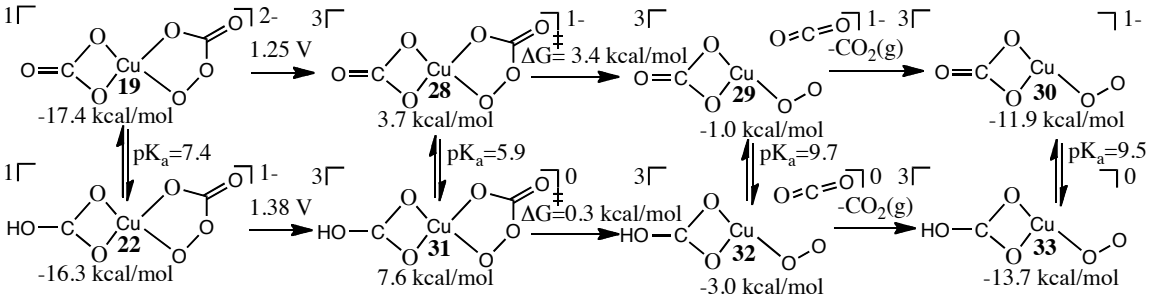

Figure 3.14. Mechanism for the release of CO_2(g) from the catalytic complex. The energies for two- and three- electron oxidized species are given with respect to **5** and **27** respectively with all energies assuming a pH of 8.2, free energies of activation reported for individual microscopic steps, and voltages vs. NHE provided for elementary steps. Charges and spin multiplicities for all species are indicated at the upper right and upper left of structures, respectively.

A similar degradation pathway was mapped out for **22**, which was established as the dominant Cu(II) peroxycarbonate species under low pH conditions. The oxidation of **22** is predicted to occur at a potential of 1.38 V**,** with exclusive production of the triplet species **31** due to a weaker stabilization of the oxidized metal center. Formation of this complex is disfavored over the production of the protonated analog **28** due to the reduced availability of stabilizing electron density. However, the neutral charge of the system favors the retro-cyclization reaction with a global free energy barrier of 5.9 kcal/mol at a pH of 6.7, which proves to favor this bond cleavage for the protonated system under these low pH conditions. However, it is of note that both the product copper-CO_2 complex and the superoxo radical species are calculated to be more stable for the protonated system under all experimental pH conditions, though similar geometric and electronic structures were calculated for both protonation states.

The release of O_2 from the system was examined for both **30** and **33** (Figure 3.15), though the direct cleavage of the Cu-O bond for these compounds is impractical. However, both complexes are vulnerable to oxidation at a weak potential and can generate a product quartet species characterized by triplet molecular oxygen coupled ferromagnetically to a d^9 Cu(II) center with a Cu-O distance of over 2.9 Å, which indicates the complete release of molecular oxygen. This spontaneous bond cleavage is predicted to occur in a concerted manner with the oxidation of the superoxo group with the low energy of oxidation allowing for a kinetically facile reaction pathway. Additional energetic stabilization is provided by the complete release of O_2 from the reactive complex to form the Cu(II) species **35** or **37**.

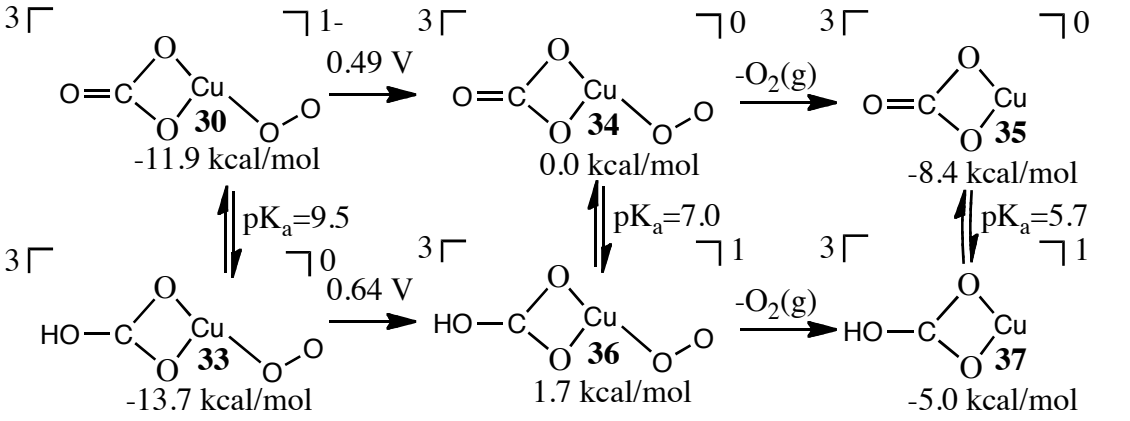

Figure 3.15. Mechanism for the release of O_2(g) from the catalytic complex. The energy for three- and four-electron oxidized species are given with respect to **27** and **34** respectively with all energies accounting for a pH of 8.2, and voltages vs. NHE provided for elementary steps. Charges and spin multiplicities for all species are indicated at the upper right and upper left of structures, respectively.

The potential at which oxidative formation of these species occurs reflects a stabilization of the deprotonated pathway due to the favorable interaction of the charged carbonate ligand with the metal center. The generation of **34** via PCET from the stable precursor **33** is predicted to be the dominant pathway at a pH of 8.2, with the oxidative formation of the bicarbonate containing **36** predicted to dominate at the lower pH of 6.7. Although, upon release of O_2 the formation of the **35** is favored, likely due a greater stabilization of this charge separated species by the increased interaction between the aqueous solvent and the copper center. In addition, the formation of **35** allows for the a bicarbonate ligand and water molecule to be recruited in order to generate the starting

complex **2** with a thermodynamic driving force of 14.0 kcal/mol with respect to **34**, insuring the completion of the catalytic cycle under any range of pH conditions.

Due to the unique nature of this water oxidation mechanism, investigation of alternate O-O bond formation pathways using a bidentate carbonate ligand were investigated with the most favorable competing pathway examined here (Figure 3.16). Although the hydroxo ligand of the starting complex **7** showed little activity towards the formation of an O-O bond, the oxo-containg **26** provides a reasonable site for water-nucleophilic attack to occur, which is a common reaction mechanism for other mono-nuclear water oxidation catalysts.[159-162] Complex **26** may recruit a water molecule with a 0.6 kcal/mol penalty associated with the entropic cost of forming the pre-reactive complex, allowing for the water molecule to be supported by hydrogen bonds to the carbonate ligand and the oxo-group. This reaction pathway proceeds via a rotation of the oxygen atom on the water molecule towards the activated oxo-group, forming an O-O bond while concurrently transferring a proton to the carbonate group, with a stepwise transition state energy of 21.0 kcal/mol. This activated water nucleophilic attack produces a hydrogenperoxo group 1.8 kcal/mol lower in energy than the starting complex **7**, illustrating a mildly exothermic reaction. However, when compared to other chemical mechanisms, this pathway possesses a global free energy barrier of 33.7 kcal/mol, approximately 15.2 kcal/mol higher than predicted for the generation of the peroxycarbonate ligand contained in compound **18**. The large free energy barrier for this water nucleophilic attack helps underlie the favorable nature of generating the O-O bond through the use of an activated carbonate ligand.

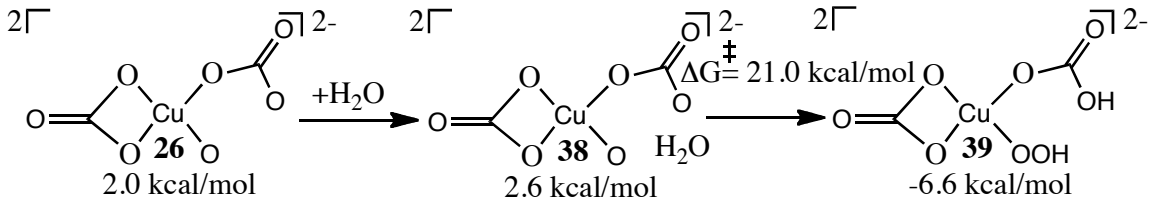

Figure 3.16. Mechanism of O-O bond formation via water nucleophilic attack for a bidentate carbonate ligand system. Relative free energies are reported with respect to **5** for a pH of 8.2 and free energies of activation are given for individual microscopic steps. Charges and spin multiplicities for all species are indicated at the upper right and upper left of structures, respectively.

3.3.4.2. Di-Aqua Water Oxidation Pathway

It is important to note that **5** is predicted as the dominant product of oxidation under low pH conditions and its ability to oxidize water in a pathway competing with the mono-aqua species should be considered. Additionally, the ability of **5** and **7** to interconvert indicates that these two pathways may be linked and that this possibility should be considered for all di-aqua structures. However, it is important to note that the favorable formation of an O-O bond requires the presence of an activated hydroxo-ligand, with the formation of three possible activated complexes considered here (Figure 3.17). The most energetically favored hydroxo containing compound is predicted to form via the deprotonation of **5** with a pk_a of 10.7. This product complex possesses a free energy of 16.2 kcal/mol with respect to the ground-state complex **11,** indicating a significant preference for the formation of the mono-aqua analog **7**.

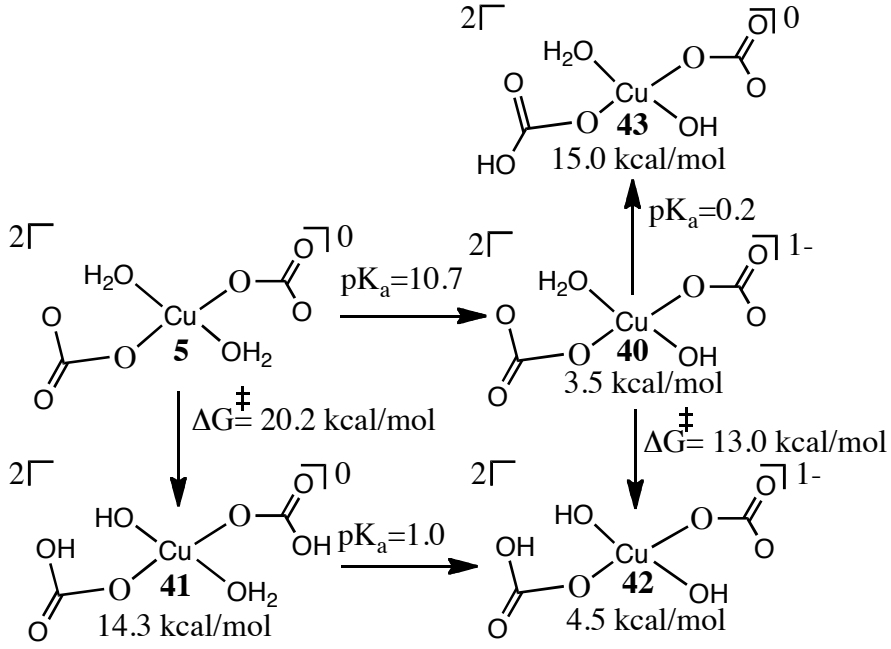

Figure 3.17. Mechanism for the formation of three reactive hydroxo containing complexes. Relative free energies are reported with respect to **5** for a pH of 8.2 and energies of activation are given for individual microscopic steps. Charges and spin multiplicities for all species are indicated at the upper right and upper left of structures, respectively.

An alternative pathway for the formation of an activated species involves an intramolecular proton transfer to form a cis-hydroxo/bicarbonate complex **41**, with a free energy barrier of 20.2 kcal/mol. This barrier coupled with the high energy of the product species indicates the unfavorable nature of this hydroxo/bicarbonate complex. However, an analogous proton transfer for **40** is predicted to generate the di-hydroxo complex **42** with a global free energy of 17.2 kcal/mol, indicating an energy similar to that predicted for the aqua/carbonate ligand system. These complexes can also be compared to the

formation of the trans-hydroxo/bicarbonate ligand system found in complex **43**, which possesses an energy 0.7 kcal/mol higher than the analogous complex **41**, indicating the slight preference of for allowing the hydroxo and bicarbonate groups to support each other through hydrogen bonding. However, it is clear that the formation of a hydroxo-ligand for the mono-aqua systems is favored and that the reactivity of these diaqua complexes will be impeded by the elevated energies of the hydroxo containing species.

Despite the high-energy of formation for these three activated species, all complexes maintain a reactive carbonate radical substituent placed in close proximity to the hydroxo-ligand. This similarity to the mono-aqua system allows for an examination of the impact of an additional aqua-ligand to the copper-coordination sphere on the formation of the critical peroxycarbonate goup (Figure 3.18). Complex **40** serves as a hydrated analog to **7** and the radical coupling of the hydroxo and carbonate ligands is predicted to occur in a similar fashion, with a 1.3 kcal/mol lowering of the stepwise free energy barrier indicating that the transition state energy may be stabilized by the increased O-C-O angle provided by the monodentate ligands. However, the transition state possesses a global free energy of 22.7 kcal/mol due to the high-energy character of the starting complex. The product hydrogenperoxycarbonate complex **44** lays 14.0 kcal/mol downhill in energy, ensuring its favorable formation, but possesses a free energy 3.6 kcal/mol above the mono-aqua complex **18**. In addition, **44** also possesses a slightly higher pK_a for the peroxy hydrogen, further increasing the difficulty of generating the product peroxycarbonate ligand with respect to the analogous complex **19**.

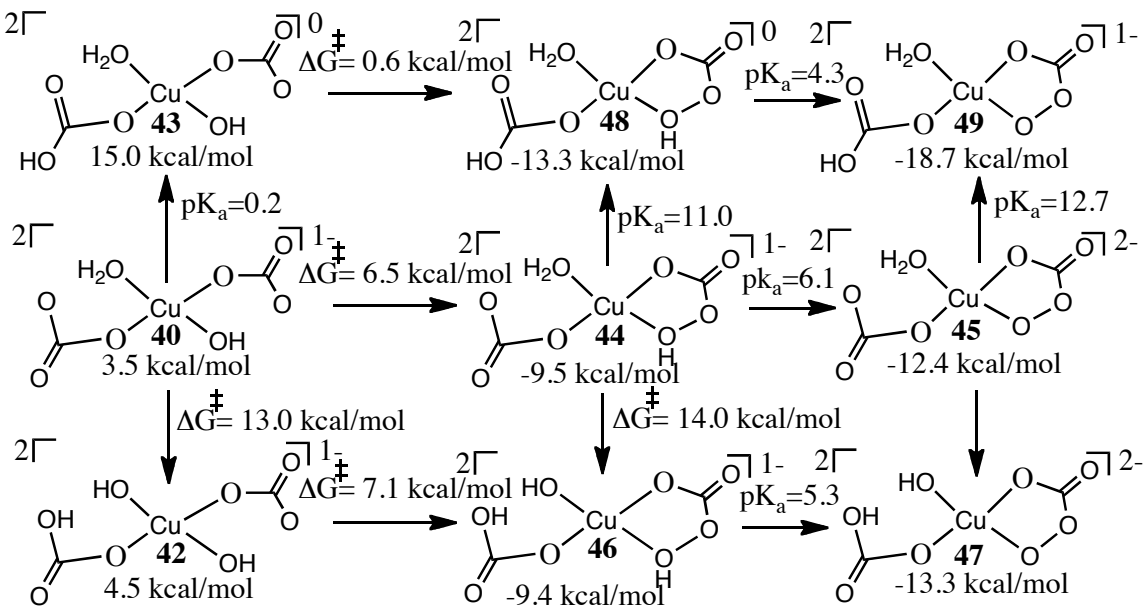

Figure 3.18. Mechanism of peroxocarbonate forming pathways using activated di-aqua complexes as a starting material. Relative free energies are reported with respect to **5** for a pH of 8.2 and free energies of activation are given for individual microscopic steps. Charges and spin multiplicities for all species are indicated at the upper right and upper left of structures, respectively.

The formation of the peroxycarbonate ligand was also examined for the tautomer complex **42** to examine the effect of a second hydroxo-ligand on the pathway energetics. The formation of the O-O bond is predicted to occur with a stepwise free energy barrier 0.6 kcal/mol higher than was predicted the for the aqua/carbonate ligand system, indicating that the change in coordination sphere results in only a slight destabilization of the transition state. The product hydrogenperoxycarbonate **46** is predicted to be equi-energetic with the tautomer complex **44**, though the bicarbonate containing system is predicted to possess a more acidic peroxy-hydrogen atom. The slight increase in acidity

indicates that the electron withdrawing bicarbonate ligand has a greater impact than the electron rich hydroxo-ligand. As a result, the stable product species **47** is preferred over the aqua/carbonate analog **45** and may be formed via an intramolecular proton transfer in a barrierless process. The generation of **47** can then be expected by either the formation of the precursor complex **45** or by the recruitment of a hydoxide molecule by the mono-aqua bicarbonate complex **22** with an endothermic energy of 3.0 kcal/mol, demonstrating a continued preference for the electron poor mono-aqua system.

The water oxidation pathway was also examined for the protonated complex **43** to assess the impact of the electron withdrawing bicarbonate ligand. However, the formation of the peroxycarbonate group for this system is unlikely to occur despite the low stepwise barrier for O-O bond formation of 0.6 kcal/mol, as the high energy of the precursor complex translates to a global free energy barrier of 27.7 kcal/mol. This elevated transition state energy stands in contrast to the product complex **48**, which is equi-energetic with the favorable bidentate bicarbonate containing compound **21**. With the direct formation of the O-O bond from **43** forbidden, the most likely route for the generation of **48** is via the recruitment of a water molecule by **21**. In addition, this low energy is further enhanced by the greater acidity of the peroxycarbonate group, due to the increased electron withdrawing character of the bicarbonate/aqua ligand system over the deprotonated or bidentate analog compounds.

The oxidative activation and susbsequent degradation of these peroxycarbonate ligands was examined and compared to the mono-aqua pathways (Figure 3.19). The oxidation of the aqua/carbonate **45** was predicted to occur at a potential of 1.23 V with

the dominant product predicted to be the triplet species **50**, indicating a preference for the formation of a peroxy-radical over the generation of a charged Cu(III) center. Despite this favoring of Cu(II), the formation of the peroxycarbonate radical species is predicted to occur at a potential similar to that found for the bidentate system, indicating that the inclusion of an aqua-ligand destabilizes the Cu(III) system, but has little impact on the oxidation of the peroxycarbonate group. Although the formation of the triplet complex is predicted to occur at a similar potential, the monodentate carbonate species lays 4.4 kcal/mol above the bidentate triplet analog due to the higher energy of the reduced precursor for the aqua/carbonate system. In a similar fashion, both triplet complexes possess near identical energies for both the barrier and product complexes of the retro-cyclization reaction as well as for the release of CO_2. In addition, all of these complexes demonstrate similar geometric and electronic properties for the reactive peroxycarbonate group, which when coupled with the energetic values indicates that the recruitment of a water molecule only impacts the pathway by a ~4 kcal/mol destabilization of the copper coordination sphere and has little effect on the degradation of the peroxycarbonate ligand.

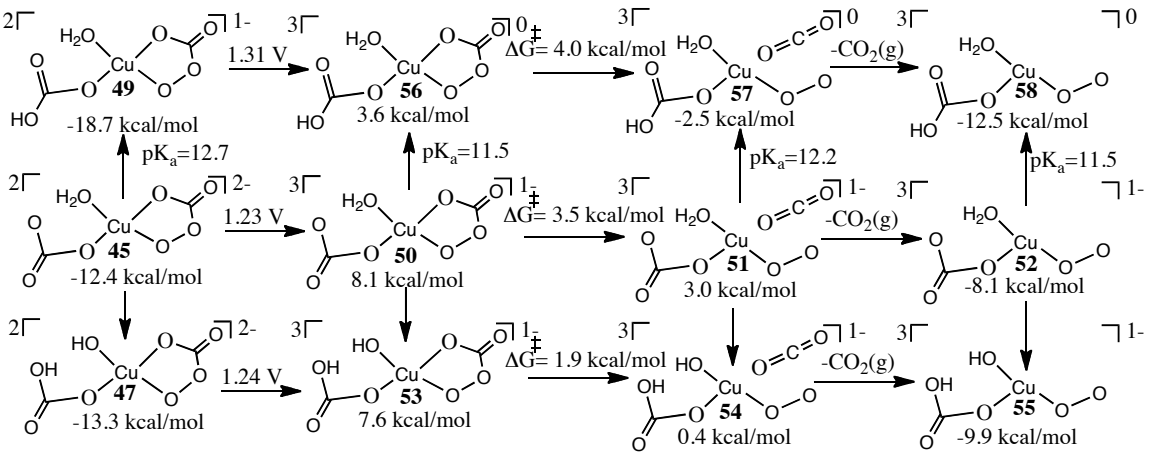

Figure 3.19. (Previous Page) Mechanism for the release of CO_2(g) from catalytic the complex. The energies for two- and three-electron oxidized species are given with reference to **5** and **27** respectively with all energies assuming a pH of 8.2, free energies of activation reported for individual microscopic steps, and voltages vs. NHE provided for elementary oxidation steps. Charges and spin multiplicities for all species are indicated at the upper right and upper left of structures, respectively.

The pathway for the release of CO_2 from the hydroxo/bicarbonate containing system was also examined in order to determine the impact of the proton transfer. The oxidation of the peroxycarbonate ligand in **47** was predicted to occur at 1.24 V to generate the triplet species, with a potential comparable to the aqua/carbonate system indicating that the choice of ligand protonation has little impact on the electron density of the peroxycarbonate ligand. However, the subsequent retrocyclization reaction is predicted to occur with a product and stepwise free energy barrier lower than predicted for the aqua/carbonate system but higher then expected for the bidentate bicarbonate complex, indicating that the inclusion of the hydroxo ligand destabilizes the superoxo radical species less than the protonation of the carbonate ligand. However, the change in ligand system had little impact on the release of CO_2 from the product complex.

The oxidative activation of **49** is of specific interest, as this complex is predicted to be the most stable Cu(II) peroxycarbonate species and can help to assess the impact of the protonation of the carbonate ligand and the recruitment of a water molecule to the copper coordination sphere. The oxidation of **49** is predicted to occur at 1.31 V to

exclusively produce the triplet species, with the recruitment of an aqua group preferentially stabilizing the oxidized peroxycarbonate ligand compared to the bidentate bicarbonate complex, though oxidation is predicted to occur at potentials higher than for the more negatively charged systems. This high oxidation potential is offset by the lower energy of the starting material, resulting in **56** possessing an equivalent energy to the triplet peroxycarbonate **28**, though formation of the aqua/bicarbonate system will be preferred under low pH conditions. The stability of **56** is supported by the fact that it possesses the highest stepwise free energy barrier for the retro-cyclization reaction, though this translates to a reasonable global free energy barrier of 7.6 kcal/mol as compared to the singlet species **27**. In addition, the energy of the product complex **57** demonstrates the stabilizing influence of electron poor ligands on the product superoxo radical species as the only ligand system with a lower free energy is the bidentate bicarbonate complex, indicating that the possible loss of an aqua ligand may occur concurrently with the release of CO_2.

The oxidation of these superoxo complexes was predicted to occur in a similar manner as found for the bidentate ligand systems, with an oxidation of the peroxo-group generating molecular oxygen in a barrierless process (Figure 3.20). The oxidation of the aqua/carbonate containing complex **52** is predicted to occur at a potential slightly lower than calculated for the bidentate system with the subsequent complete release of O_2 occurring at a slightly smaller exothermic energy than for the monodentate case. The difference in these energetic steps likely reflects a stabilization of the oxidized intermediate by the aqua containing system, which may be due to either the open

coordination sphere around the copper center or an increase in electron donation from the additional aqua ligand. It is important to note that due to the high energy of the initial complex **52**, the aqua/carbonate system is unfavorable in energy and the recruitment of a water molecule by the bidentate coordinated system is unlikely to occur.

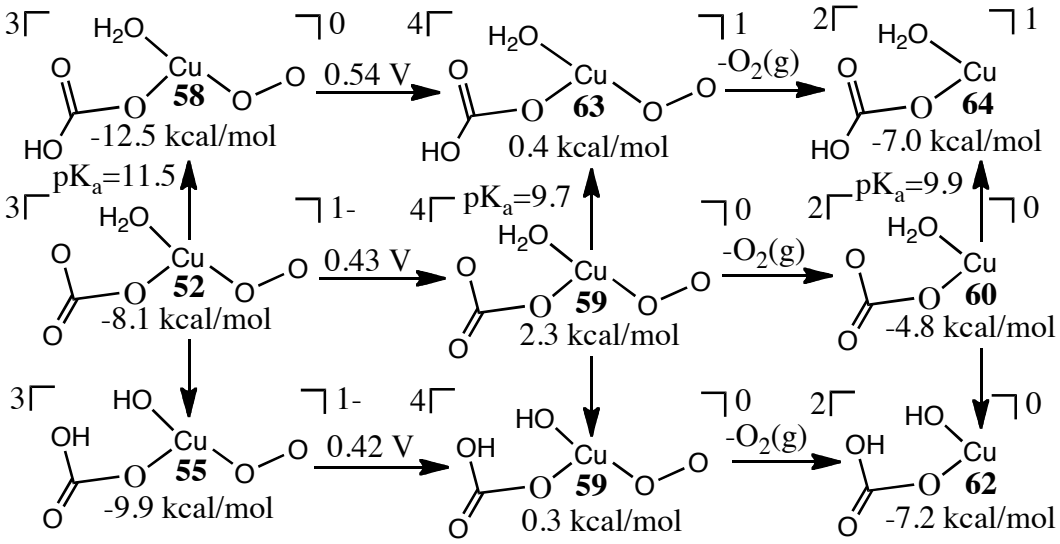

Figure 3.20. Mechanism for the release of O_2(g) for the di-aqua containing pathways. The energies for three- and four-electron oxidized species are reported in reference to **27** and **34** respectively with all energies accounting for a pH of 8.2 and with voltages vs. NHE provided for elementary steps. Charges and spin multiplicities for all species are indicated at the upper right and upper left of structures, respectively.

The release of O_2 from the hydroxo/bicarbonate compound follows a similar reaction pathway to the tautomer species **52**. Complex **55** is predicted to undergo an oxidation of the superoxo group at a potential of 0.42 V, near identical to that predicted for the tautomer form. In addition, both complexes demonstrate similar energies for the release

of O_2, indicating that proton transfer has little impact on the energetics of these pathways. When compared to the bicarbonate complex **33**, a decrease in both the oxidation potential and the exothermic energy of O_2 release demonstrates that the recruitment of a hydroxo-group aids in product stabilization through the addition of electron donating character.

Finally, the oxidation of the aqua/bicarbonate complex **58** is of importance as this compound is predicted to be the most stable superoxo radical species and to undergo oxidation at a potential of 0.54 V to form a quartet complex. This energy reflects a favorable oxidation in comparison to the bidentate system due to the electron donating aqua-ligand. However, both bicarbonate species show a similar energy for the release of O_2, though the lower oxidation energy results in a favoring of the aqua/bicarbonate system by 2.0 kcal/mol. The low energy of this pathway compares favorably with the bidentate carbonate pathway, with the monodentate system dominating at a pH of 6.7. Furthermore, the recruitment of an additional bicarbonate and water molecule allows for the reformation of the starting complex **1** with an exothermic energy of 7.2 kcal/mol with respect to **64**, offering a completion of the catalytic cycle for low pH systems.

Mechanisms including a peroxycarbonate intermediate offer the most favorable di-aqua water oxidation pathways, but water nucleophilic attack mechanisms for O-O bond formation were examined with the most energetically favorable pathway described here for comparison (Figure 3.21). However, it is of note that an oxo-ligand is needed to provide a site where water nucleophilic attack may occur. The most likely pathway to form this reactive oxo-group uses **40** as a starting material and proceeds via an intramolecular proton transfer from the hydroxy-group to the carbonate ligand to form **63**

with an endothermic energy of 8.1 kcal/mol. The subsequent recruitment of a water molecule from solution to form a pre-reactive complex is predicted to occur with a low free energy. The remaining carbonate ligand can then abstract a proton from this loosely coordinated water molecule, which can undergo a concerted water nucleophilic attack upon the oxo-group, with a stepwise free energy barrier of 13.6 kcal/mol. This reaction generates a final product of **65**, which contains a stable hydrogen peroxo group supported by hydrogen bonding with a bicarbonate ligand. Unfortunately the global free energy barrier for the formation of this complex is 36.9 kcal/mol relative to **11**, leading to a continued preference for O-O bond formation through pathways including peroxycarbonate intermediates.

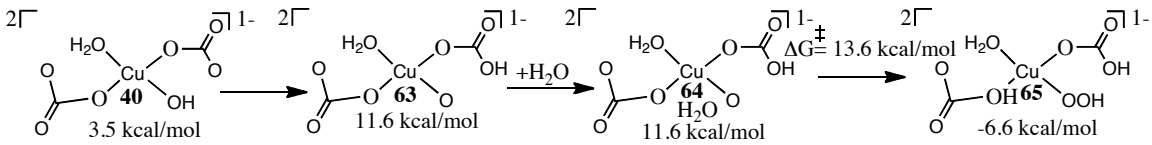

Figure 3.21. Formation of a peroxo group via water nucleophilic attack for a system with monodentate ligands. Relative free energies are reported with respect to **5** for a pH of 8.2 and free energies of activation are given for individual microscopic steps. Charges and spin multiplicities for all species are indicated at the upper right and upper left of structures, respectively.

3.4. Conclusions

The water oxidation ability of this class of copper catalysts is unique in that the carbonate ligand system allows for a great deal of mechanistic flexibility. This behavior

is exemplified by the availability multiple protonation states, binding motifs and the redox non-innocent nature of the carbonate ligands. All of these properties are needed to explain the cyclic voltammetry of the copper solution, as three complexes are available in the ground state and mild free energy barriers allows for the dominance of a single complex at a given pH. This results in three separate oxidative pathways that can generate a mix of Cu(III) and carbonate radical species that can rapidly interconvert once formed. However, it is the presence of the highly oxidized non-innocent ligands found in **5** or **7** that allows for monomeric water oxidation and requires the use of large external potentials.

Once these highly oxidized compounds are formed, a wide range of ligand rearrangements can take place, including the formation of the stable octahedral Cu(IV) complex **11**. However, this compound is catalytically inactive and fast O-O bond formation is predicted to occur solely through the radical coupling of the carbonate and hydroxo-groups found in **7**, with all other pathways for O-O bond formation predicted to be significantly higher in energy. After the formation of this hydrogen peroxycarbonate ligand, several pathways for the release of O_2 and CO_2 are available, but mainly differ in the identity of the supporting ligands.

Under all conditions, the catalytic pathway is predicted to proceed through the formation of a peroxycarbonate group that can be oxidized to form a reactive triplet species. This complex can either be re-reduced at ~1.25 V at fast scan rates, or undergo a retro-cylization reaction with a low free energy barrier. This results in the loss of CO_2 from the complex, leaving behind a Cu(II)-superoxo radical species that can be oxidized

at the peroxo group to spontaneously release triplet O_2 from the remaining complex and finally recruit bicarbonate and water molecules from solution to reform the starting materials. This process can occur with a wide range of supporting ligands, but the most favorable pathway at high pH conditions utilizes a bidentate carbonate ligand and at a low pH favors the use of a mono-dentate aqua/bicarbonate ligand system. However, the low free energy difference between binding motifs indicates that both forms occur in solution and that changes in the copper coordination sphere likely happen rapidly after the kinetically limited formation of **18**.

When compared to other water oxidation catalysts, this monomeric system demonstrates both a fast turn-over frequency and a large overpotential. These traits can be explained by the need to oxidize the carbonate ligand system, which takes place only at high potentials, but allows for the rapid formation of a peroxycarbonate group. This ligand can then be oxidized to release O_2 and CO_2, which can reform carbonate and bicarbonate in solution, allowing for the high degree of durability shown experimentally. Though future work needs to be performed to properly identify the nature of the *heterogeneous* dinuclear catalytic system and whether similar copper water oxidation catalysts also utilize a radical coupling mechanism for O-O bond formation.

Chapter 4. Adsorption of Nitrogen-Rich Aromatic Groups to Aluminum Containing Surfaces

4.1. Introduction

There is currently a desire to understand how both high-energy compounds (HECs) and industrial byproducts bind to minerals, soil components and industrial materials in order to understand the impact of these substances upon the environment.[163-167] Specifically, the abundance of aluminum-based surfaces in both nature and industry makes these compounds important possible substrates for the binding of environmental contaminants.[168-170] To understand the interactions of these adsorbates and surfaces, computational methods were employed to examine these interfaces at a molecular level. Special attention was placed on alumina surfaces as they can be found in industrial materials,[171-173] natural minerals,[168,169] and serve as model systems for a range of metal oxide surfaces.[174-176]

The aluminum metal surface, while not present in nature, was also investigated in order to provide a reference for other aluminum containing surfaces. Specifically, the (001) aluminum surface was examined as it is comparable to the experimentally relevant α-alumina phase and has been demonstrated to generate an alumina surface upon oxidation.[177-179] The α-alumina phase is of particular interest due to its presence in wear resistant coatings,[180-182] catalytic substrates[183-186] and optics. Additionally, the (0001) α-alumina surface has been determined to be the most thermodynamically stable alumina phase and is known to contain a variety of terminating groups that may be present in

nature, depending upon the environment at the surface.[187-189] Under "dry" conditions the alumina surface has been found to terminate with a single aluminum atom, with the aluminum-terminated surface representing an alumina surface exposed to gas-phase adsorbates.[190-192] However, in the presence of water, a hydroxyl termination of the alumina surface has been experimentally and theoretically identified as the dominant configuration, and as such this "wet" surface is a likely substrate for the adsorption of environmental contaminants.[193-195] In order to accurately address the possible adsorption capacity of a wide range of aluminum containing substrates, we investigated the molecular interactions of a set of adsorbates with the aluminum metal surface in addition to both aluminum and hydroxyl terminations of the α-alumina surface.

The adsorption capacity of these three aluminum containing surfaces was examined utilizing a test set of adsorbates relevant to both industry and potential future use in HECs. This test set included a complete survey of pyridine, diazine, triazine, and tetrazine molecules (Figure 4.1). These adsorbates were chosen to describe both common industrial agents and the binding behavior of adsorbates containing multiple aromatic nitrogen groups, as nitrogen-rich compounds have been targeted for the future development of "green" explosives, which may be more friendly to the environment than traditional HECs.[195-197] This test set was also chosen for the modest size of the adsorbates, which allows for the easy computational analysis of the electronic binding energies of molecular adsorption onto an aluminum containing surface through the use of a periodic slab model.

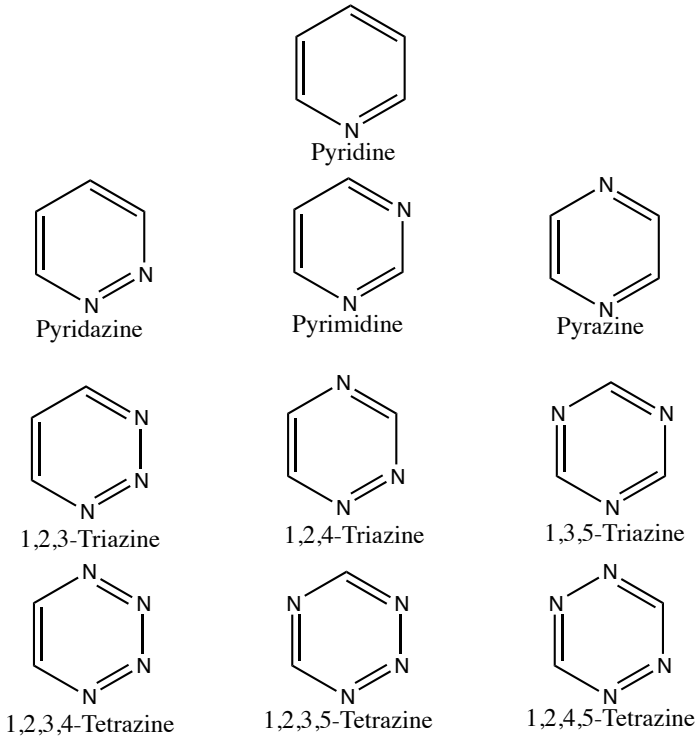

Figure 4.1. A suite of ten possible adsorbates that were chosen to describe the interaction of industrial products and nitrogen-rich aromatic compounds with aluminum containing surfaces. The test set includes one pyridine, three diazine, three triazine, and three tetrazine molecules. These adsorbates represent all possible arrangements of cyclic amines in the aromatic ring in order to examine binding motifs that may play a role in the adsorption behavior of HECs.

4.2. Computational Methodology

To accurately describe the interactions of this family of adsorbates with aluminum containing surfaces, both an aluminum metal and α-alumina slab were constructed in a periodic lattice using the Vienne *ab intio* Simulation Package (VASP).[198-200] This procedure involved the optimization of a computational protocol for a single unit cell of

each material in the bulk phase. This optimized protocol was then used to construct a periodic slab model, which includes a large vacuum space separating the repeating slabs to allow for the analysis of an adsorbate molecule bound to the surface of the slab.

4.2.1. The Aluminum (001) Surface

Calculations for the aluminum metal surface were performed using plane-wave density functional theory (PW-DFT) as implemented in VASP with the Perdew-Burke-Ernzehof (PBE) functional, which is based on the Generalized Gradient Approximation (GGA).[201] Treatment of all atom types were accomplished through the use of ultrasoft pseuodpotentials of the projected augmented wave (PAW) type.[41,202-204] Convergence tests were performed on the aluminum metal face-centered cubic (FCC) unit cell, which informed the choice of a 450 eV cutoff energy and the use of a 6x6x1 kpoint lattice with an optimized unit cell length of 4.03 Å.

These parameters were used to optimize a model of the aluminum metal (001) surface by constructing an aluminum slab. Multiple slab thicknesses were tested and a surface six aluminum layers deep was determined to offer the best compromise between accuracy and computational expense. During optimizations of the surface, the bottom three layers of the slab were fixed at their bulk geometries in order to allow for an accurate representation of surface interactions with the bulk phase. A surface of 3x3 unit cells was utilized to minimize the interactions between periodic reflections of the large adsorbate molecules, and the use of a ~20 Å vacuum space insured that the adsorbed molecules interacted with a single aluminum metal surface. Additional calculations were

performed to insure that the computational parameters optimized for the bulk phase produced reasonable and consistent results when applied to both the bare surface and bound adsorbate containing systems.

4.2.2. Alumina Surfaces

The α-alumina system was also examined using PW-DFT with the PBE density functional and ultrasoft PAW pseudopotentials. In addition, this system was characterized using spin polarization, as accounting for unpaired spin has been known to improve the description of binding to the alumina surface.[205] Convergence tests were performed using the primitive α-alumina rhombohedral unit cell in the bulk phase and this indexing of the alumina unit cell will be used throughout this work. Calculations on this system showed a convergence of energies with the choice of a 500 eV energy cutoff and a 2x2x1 kpoint lattice. In addition, the unit cell lengths were optimized at a=4.810 Å and c=13.218 Å, which are slightly larger than experimentally observed distances, but were found to be in good agreement with previous theoretical work.[206-209]

An alumina slab was constructed using the experimentally relevant (0001) surface, which contains an offset Al-O-Al-Al-O-Al stacking motif that repeats after six O-layers. However, previous studies have shown that adsorption behavior can be best modeled using an alumina slab six O-layers deep with no fixing of any atomic positions, as fixation of these positions introduces asynchronous behavior in the slab and produces errors in calculated electronic binding energies.[210-212] This alumina slab was expanded to a 2x2 surface with a vacuum space of ~20 Å to allow for the inclusion of our test set of

adsorbate molecules, which demonstrated no interactions with the periodic surface boundary or periodic adsorbate molecules for this super-cell. The use of these computational parameters for an alumina surface was confirmed to accurately describe surfaces terminated by either a single aluminum atom or hydroxyl groups.

4.3. Results

4.3.1. Aluminum Metal Surface

Optimizations were performed for the bare aluminum surface, allowing for a characterization of the metal surface when exposed to vacuum. Specifically the outermost layer of aluminum atoms experienced a displacement of 0.05 Å into the vacuum space while all other atoms remained close to their bulk phase positions, though no displacements were observed in the X and Y directions for any layer. When examined for possible adsorption sites, the (001) aluminum surface provides only a single class of surface aluminum atoms, which is characterized by four neighboring aluminum atoms and four small adjacent vacancies (Figure 4.2), allowing for a degree of flexibility in the orientation of bound adsorbates.

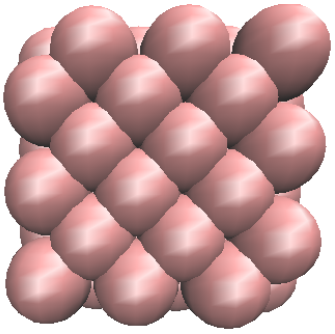

Figure 4.2. The structure of the (001) aluminum surface of a 3x3 super-cell containing eighteen available aluminum atoms and eighteen small vacancies.

The binding of adsorbates at the aluminum surface was first probed using a pyrdine molecule, and two main modes of adsorption were identified, includinng a possible side-on coordination and the formation of an Al-N bond to the pyridine nitrogen group. The side-on adsorption takes place through association of the pyridine π-complex with the aluminum surface, where the pyridine ring is centered over the aluminum atom and the plane of the aromatic ring is rotated such that the nitrogen group rests directly above a neighboring surface aluminum atom. However, the pyridine molecule remains only loosely coordinated to the metal surface with a distance of ~4 Å between the aluminum surface and the plane of the pyridine aromatic ring, and a low favorable electronic binding energy of 1.3 kcal/mol was observed with this weak binding unlikely to overcome destabilizing entropic effects. As a consequence, coordination to the aluminum surface through these π-interactions is unlikely to occur.

The alternative method for the binding of pyridine to the aluminum surface is predicted to involve the formation of a σ-bond between the cyclic amine and a surface aluminum atom (Figure 4.3). This adsorption process includes the generation an Al-N bond at an angle perpendicular to the aluminum surface and with a bond distance of 2.11 Å. The plane of the pyridine molecule is rotated such that it lays diagonal across the face of the unit cell, placing both ortho-methine groups proximal to the neighboring aluminum atoms, which results in Al-H distances of ~2.9 Å, indicating a possible weak coordination to the electron rich metal surface. Additionally, the bound aluminum atom was observed at a distance 0.50 Å above the surface of the slab, indicating the possible build up of positive charge on the bound aluminum center, which may allow for the formation of the

Al-N bond. This combination of the generation of a stable covalent bond and the energetic cost of isolating an aluminum atom from the metal surface results in a favorable electronic binding energy of 12.1 kcal/mol, illustrating the preference of pyridine to coordinate to the aluminum surface through the formation of a covalent bond as compared to binding exclusively through the use of weak dispersive π-interactions.

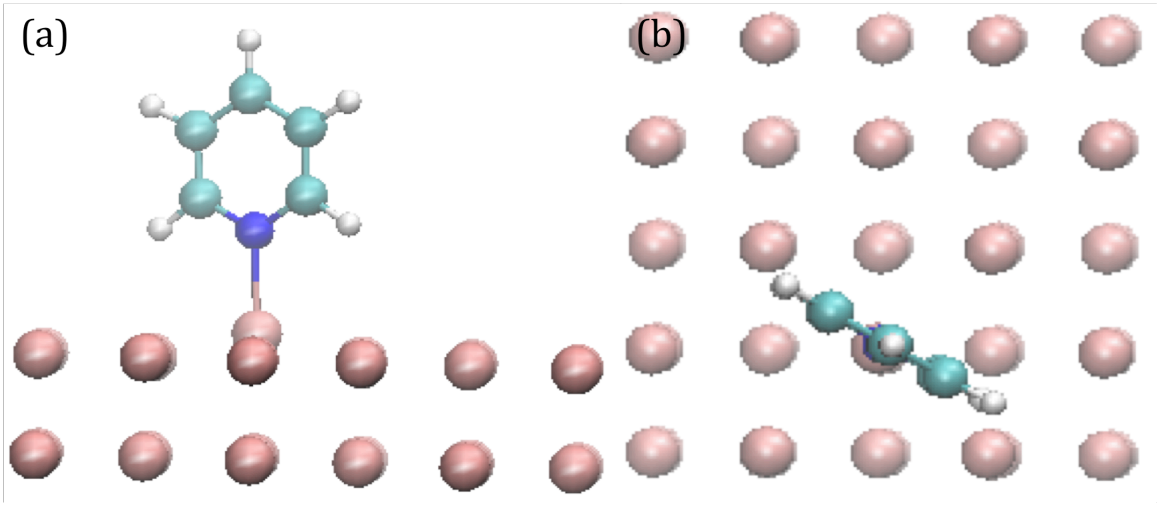

Figure 4.3. Geometry of a pyridine molecule bound to the surface of the aluminum metal slab through the formation of an Al-N bond from a side-on (a) and a top-on view (b). Aluminum atoms are shown in pink, nitrogen in blue, carbon in teal, and hydrogen is depicted in white.

The full set of test adsorbate molecules was examined for both possible binding motifs. When the formation of the side-on complex was investigated, all members of the test set demonstrated adsorbate distances of ~4 Å above the alumina surface with weak favorable electronic binding energies between 1 and 1.4 kcal/mol. This small variability

in energies was largely due to the rotation of the adsorbate molecule relative to the surface aluminum center in order to maximize interactions between cyclic amine groups and the neighboring aluminum atoms. These consistently weak binding energies to the metal surface help indicate the minor role that dispersive interactions likely play in the association of aromatic adsorbates with the aluminum metal surface.

In comparison, the multiple nitrogen groups found on the aromatic rings of the adsorbate test set allows for the formation of unique arrangements of covalent bonds to the metal surface, though in all cases the Al-N bond was found to form perpendicular to the aluminum surface with the bound aluminum atom displaced ~0.5 Å above the surface aluminum layer. However, slight rotations of the plane of the aromatic ring were observed, with the plane of adsorbate molecules possessing two ortho-methine groups laying parallel to the plane of the neighboring aluminum atoms while the remaining adsorbates were oriented in line with the vacant sites of the aluminum metal surface, though the Al-H distances in all cases were large enough that their impact on the electronic binding energies is expected to be minimal.

The lowest energy bound complex for the test set of adsorbates is predicted to form through the generation of an Al-N bond with a distance between 1.97-2.16 Å and a binding energy in the range of 7.6-16.4 kcal/mol (Table 4.1). By analyzing this data we find a trend in the impact of nitrogen substitution on the aromatic ring; specifically, examination of the diazine adsorbates demonstrates a destabilizing influence of nitrogen substitution at the meta- and para- positions, likely due to the additional electron withdrawing character of these nitrogen groups. However, analysis of the triazine and

tetrazine electronic binding energies indicates that this destabilization only occurs in the absence of ortho-amine substituents, indicating a change in binding behavior upon the inclusion of nitrogen groups at the ortho-position.

Table 4.1 Electronic binding energies and Al-N distances for ten possible nitrogen containing aromatic adsorbates on an aluminum metal surface bound through the formation of a covalent Al-N bond. For adsorbates containing more than one unique cyclic-amine group, the nitrogen atom bound to the surface is highlighted in red.

Adsorbate	Binding Energies	Al-N Distances
Pyridine	-12.6 kcal/mol	2.11 Å
Pyridazine	-12.8 kcal/mol	2.08 Å
Pyrimidine	-9.5 kcal/mol	2.11 Å
Pyrazine	-9.7 kcal/mol	2.16 Å
1,2,3-Triazine	-9.8 kcal/mol	2.05 Å
1,2,3-Triazine	-12.4 kcal/mol	2.00 Å
1,2,4-Triazine	-13.3 kcal/mol	2.02 Å
1,2,4-Triazine	-12.2 kcal/mol	2.04 Å
1,2,4-Triazine	-8.1 kcal/mol	2.07 Å
1,3,5-Triazine	-7.6 kcal/mol	2.15 Å
1,2,3,4-Tetrazine	-12.7 kcal/mol	2.01 Å
1,2,3,4-Tetrazine	-12.9 kcal/mol	2.00 Å
1,2,3,5-Tetrazine	-11.0 kcal/mol	2.04 Å
1,2,3,5-Tetrazine	-16.4 kcal/mol	1.97 Å
1,2,3,5-Tetrazine	-11.6 kcal/mol	2.03 Å
1,2,4,5-Tetrazine	-15.4 kcal/mol	2.00 Å

In comparison to nitrogen substitution at the meta- and para- positions, the electronic binding energies of adsorbates with ortho-amine groups indicate a stabilization of the Al-N bond upon nitrogen substitution. The covalent bond is likely stabilized through π-backdonation from the electron rich metal surface to the electron poor aromatic ring, with the inclusion of nitrogen groups at the ortho-position lowering the LUMO of the aromatic

ring such that electron density can be accepted from the metal surface. This π-backdonation results in shorter Al-N distances for adsorbates with increasing numbers of nitrogen substituents, indicating an increased occupation of the Al-N π-orbitals. This stabilizing influence of electron-withdrawing character for this binding motif is further supported by the favorable binding energies for aromatic groups with increasing nitrogen substitution once an ortho-amine group enables electron donation from the metal surface.

In summary, binding of aromatic groups containing cyclic amines on an aluminum metal surface is predicted to occur through the formation of an Al-N bond. If two methine groups are located in the ortho-positions relative to the bound amine, the addition of electron withdrawing character is predicted to destabilize σ-donation to the metal surface, decreasing the electronic binding energy. However, if at least one ortho-position contains a nitrogen group, the addition of electron withdrawing groups to the aromatic ring appears to strengthen binding to the metal surface. Furthermore, for nitrogen-rich adsorbates, we predict surface binding to occur at cyclic amine groups that contains at least one nitrogen substituent in the ortho-position.

4.3.2. Alumina Surfaces

4.3.2.1. Aluminum-Terminated (0001) α-Alumina Surface

The (0001) α-alumina slab was optimized for a surface terminated by a single aluminum atom and was compared to previous theoretical and experimental results for validation. The outer layer of the slab was found to contract from a distance of 0.85 Å between the Al and O layers found in the bulk phase to an optimized distance of 0.10 Å,

which is consistent with other PW-DFT results and is attributed to the highly ionic nature of the Al^{3+} and O^{2-} components.[213-215] Progressively smaller contractions of the Al-O distances were observed for deeper layers until the bulk positions were reproduced for the center layers of the alumina slab, with only minor migrations of the aluminum and oxygen atoms in the X and Y directions.

Once the alumina slab was optimized, possible adsorption sites were selected from the available atoms on the surface (Figure 4.4). This α-alumina (0001) surface presents one highly available aluminum center, three equivalent oxygen atoms near the surface, and one partially buried aluminum atom. The adsorption behavior of the aromatic groups on the aluminum metal surface dissuades the possibility of π-interactions with the alumina surface and the formation of hydrogen bonds to the available oxygen groups is unlikely to significantly bind adsorbates to the surface. This indicates that the formation of an Al-N bond to the available surface aluminum atom will provide the most favorable electronic binding energies between nitrogen-containing aromatic groups and the "dry" alumina surface.

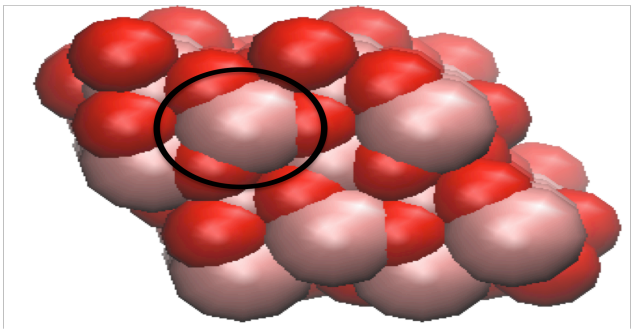

Figure 4.4. Aluminum-terminated (0001) α-alumina surface with the available aluminum binding site highlighted. Aluminum atoms are shown in pink while oxygen is depicted in red.

A pyridine molecule was used to probe the possible adsorbate binding positions and found to undergo optimal coordination to the surface through the formation of a single Al-N bond perpendicular to the surface of the alumina slab in a fashion similar to that found for the binding of pyridine to the aluminum metal surface (Figure 4.5). However, the plane of the pyridine molecule was predicted to lay slightly out of the plane of the neighboring oxygen atoms, minimizing any opportunities to form hydrogen bonds to the surface. Instead, the formation of a strong σ-bond to the aluminum center was observed with an Al-N distance of 2.00 Å, a binding energy of 36.7 kcal/mol and a displacement of the bound aluminum atom by 0.48 Å away from the alumina surface, which has been previously proposed to demonstrate electron donation from bound adsorbate molecules to the electron poor aluminum center.[51]

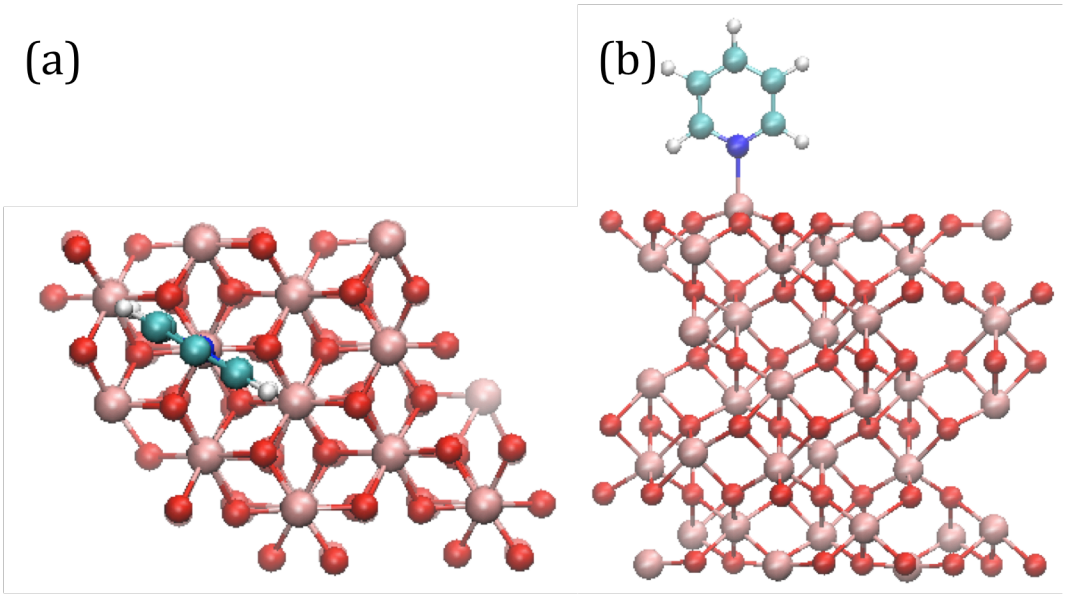

Figure 4.5. Adsorption of the pyridine molecule to an aluminum atom of the α-alumina (0001) surface from a top-on (a) and a side-on view (b).

These binding energies and aluminum migration distances can be compared to those calculated in previous theoretical studies for H_2O,[216] CO,[212] and H_3COH[217] for low adsorbate loadings (Table 4.2). A correlation between the aluminum position and the electronic binding energy of the adsorbate can be drawn, with the formation of a strong bond to the alumina surface correlated to a large migration of the aluminum center away from the unbound position. This trend indicates a preference for alumina surfaces to bind adsorbates with large electron donating character. It is also important to note that the binding of pyridine to the "dry" alumina surface is predicted to be preferred over the coordination of water and methanol by more than 8 kcal/mol, and as such we predict significant coordination of pyridine in the gas phase to alumina surfaces, though the inclusion of vibrational terms needs to be considered in order to obtain a quantitative assessment of pyridine adsorption to the alumina surface.

Table 4.2. Theoretically calculated binding energies and positions of bound aluminum atoms on the aluminum-terminated (0001) α-alumina surface for a possible set of bound adsorbates.

Adsorbate	Binding Energy (kcal/mol)	Aluminum Displacement
Carbon Monoxide[212]	-10.4	0.30 Å
Water[216]	-26.2	0.37 Å
Methanol[217]	-28.4	0.38 Å
Pyridine	-36.7	0.48 Å

The full suite of adsorbates was tested, and found to bind to the alumina surface via the formation of a covalent bond with Al-N distances between 1.98-2.03 Å and an identical orientation of the aromatic ring as was found for the pyridine case, resulting in the lack of hydrogen bonding to the surface. However, a 16 kcal/mol variation in binding

energies within the adsorbate test set was predicted, with a rough correlation to the displacement of the bound aluminum atom away from the alumina surface (Table 4.3). The introduction of nitrogen groups into the aromatic ring results in a reduction of both the electronic binding energy and the displacement of the bound aluminum atom away from the alumina surface, with the greatest reduction of binding capacity provided by the introduction of nitrogen groups at the ortho-position. These trends indicate that binding to the electron poor alumina surface may be destabilized by π-backbonding to the aromatic adsorbate.

Table 4.3. Calculated binding energies and displacement distances for the bound aluminum atom on the aluminum-terminated (0001) α-alumina surface for a test set of nitrogen containing aromatic adsorbates. For adsorbates possessing more than one unique cyclic-amine group, the position of the nitrogen atom bound to the surface is highlighted in red.

Adsorbate	Binding Energies	Al Displacement
Pyridine	-36.7 kcal/mol	0.48 Å
Pyridazine	-30.0 kcal/mol	0.46 Å
Pyrimidine	-31.9 kcal/mol	0.46 Å
Pyrazine	-33.8 kcal/mol	0.46 Å
1,2,3-Triazine	-31.0 kcal/mol	0.41 Å
1,2,3-Triazine	-24.1 kcal/mol	0.40 Å
1,2,4-Triazine	-29.4 kcal/mol	0.43 Å
1,2,4-Triazine	-29.2 kcal/mol	0.44 Å
1,2,4-Triazine	-31.0 kcal/mol	0.41 Å
1,3,5-Triazine	-31.6 kcal/mol	0.43 Å
1,2,3,4-Tetrazine	-27.6 kcal/mol	0.39 Å
1,2,3,4-Tetrazine	-20.8 kcal/mol	0.39 Å
1,2,3,5-Tetrazine	-28.3 kcal/mol	0.40 Å
1,2,3,5-Tetrazine	-21.2 kcal/mol	0.39 Å
1,2,3,5-Tetrazine	-26.9 kcal/mol	0.40 Å
1,2,4,5-Tetrazine	-26.0 kcal/mol	0.42 Å

This data indicates that nitrogen containing aromatic groups can preferentially bind to the "dry" alumina surface as compared to other atmospheric components such as water and carbon monoxide. However, the inclusion of additional nitrogen groups to the aromatic ring substantially reduces the binding energy of the adsorbate to the point where water and methanol may displace the aromatic groups from the surface, due to the additional electron withdrawing character. The presence of ortho-nitrogen groups results in the largest lowering of electronic binding energies and as a result, the adsorption of any nitrogen-rich aromatic group is predicted to occur at a nitrogen group with no ortho-amine substituents.

4.3.2.2. Hydroxyl-Terminated (0001) α-Alumina Surface

A hydroxyl-terminated surface was constructed by replacing the four surface aluminum atoms of the aluminum-terminated (0001) α-alumina slab with twelve hydrogen atoms. Six hydroxylated surfaces were constructed using random starting positions for the hydrogen atoms, which were then optimized and the lowest energy surface was selected (Figure 4.6). All surveyed conformations possessed four hydrogen atoms laying in the plane of the alumina surface and eight hydroxyl groups pointing towards the vacuum space, in agreement with previous theoretical and experimental findings.[192,193,218]

The central axial hydroxyl group on the alumina slab was selected for direct hydrogen bonding to the aromatic amine group present in our adsorbate test set. Six hydroxyl groups neighbor this central substituent, where three of the neighboring

hydrogen atoms lay in the plane of the alumina surface and three hydroxyl groups point towards the vacuum space. These surrounding hydroxyl groups are arranged in such a fashion that the planar aromatic adsorbates can interact with two neighboring hydroxyl groups at a time. This variety of neighboring hydroxyl substituents allows for the direct interaction of the adsorbate with two axial groups, two equatorial groups, or one axial and one equatorial group, enabling multiple types of interactions between the bound adsorbate and the surrounding alumina surface.

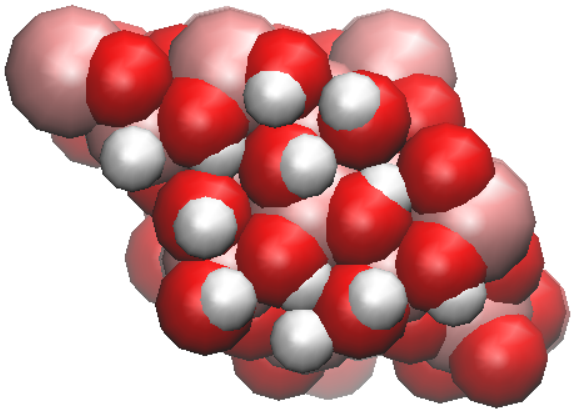

Figure 4.6. Lowest energy conformation of the hydroxyl-terminated (0001) α-alumina surface.

A pyridine molecule was utilized to probe the most favorable binding interactions between the adsorbate and the hydroxylated surface, allowing for the identification of a stable bound species (Figure 4.7). The most energetically favorable conformation for pyrdine adsorption to the hydroxylated surface was predicted to occur via the formation of a hydrogen bond to central hydroxyl group with a N-H distance of 1.93 Å and the rotation of the aromatic ring such that it lays in the plane of the two neighboring

equatorial hydroxyl groups. This positioning of the pyridine molecule results in a weak coordination of the ortho-methine groups to the surface oxygen atoms with O-H distances of 2.4 and 3.9 Å. This hydrogen bond mediated coordination results in a calculated electronic binding energy of 9.0 kcal/mol, indicating weak overall coordination of the aromatic group to the "wet" alumina surface.

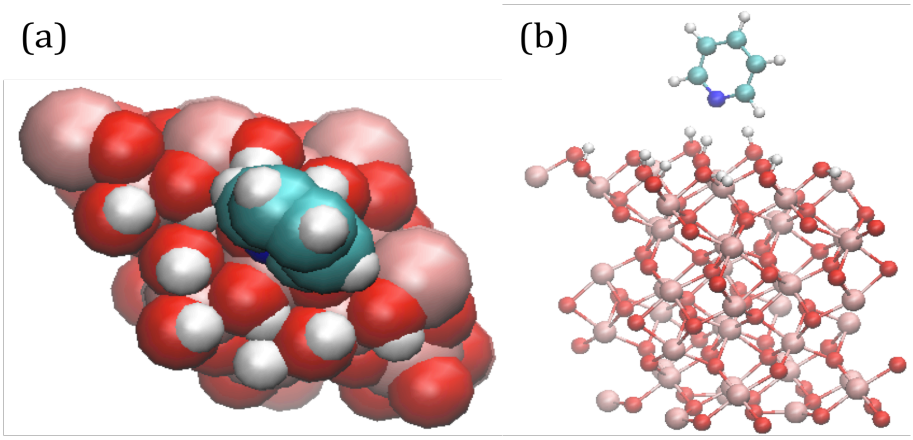

Figure 4.7. Lowest energy conformer for pyridine bound to the hydroxyl-terminated (0001) α-alumina surface from a top-on (a) and a side-on view (b).

A full survey of the adsorbate test set was undertaken, and three main configurations were observed for the binding of the aromatic group to the hydroxyl terminated alumina surface with a dependence upon the nature of the adsorbate ortho-positions. Adsorbates with two ortho-methine groups adopted conformations consistent with pyridine binding to the alumina surface. These species possessed N-H bond distance between 1.91-1.95 Å with adsorption energies between 5.7-9.0 kcal/mol (Table 4.4). The trends in these binding energies appear to be controlled by the proton affinities of the coordinating

nitrogen groups, indicating that the electronic binding energies for this class of adsorbates is dominated by the formation of a single hydrogen bond to the hydroxyl surface. This trend is confirmed by the electron rich pyridine adsorbate undergoing the tightest binding to the hydroxyl-terminated surface, while the electron poor 1,2,3,5-tetrazine experiences relatively weak surface coordination.

Table 4.4. Binding energies and hydrogen bond lengths for the coordination of adsorbates with two ortho-methine groups to the hydroxyl-terminated alumina surface. For adsorbates containing more than one unique cyclic-amine group, the nitrogen atom bound to the surface is highlighted in red.

Adsorbate	Binding Energies	N-H Distances
Pyridine	-9.0 kcal/mol	1.93 Å
Pyrimidine	-7.5 kcal/mol	1.94 Å
Pyrazine	-7.6 kcal/mol	1.91 Å
1,2,4-Triazine	-6.4 kcal/mol	1.92 Å
1,3,5-Triazine	-6.9 kcal/mol	1.95 Å
1,2,3,5-Tetrazine	-5.7 kcal/mol	1.93 Å

The second main class of adsorbate binding to the hydroxylated surface involves aromatic compounds containing two ortho-nitrogen groups. For this case, the plane of the adsorbate is found to orientate towards two axial hydroxyl groups (Figure 4.8). These complexes form the longest set of hydrogen bonds to the surface, with N-H distances between 2.01-2.05 Å and weak electronic binding energies between 6.0 and 7.8 kcal/mol (Table 4.5). These long hydrogen bond lengths likely stem from the electronic withdrawing character of the nitrogen groups and a slight tilting of the aromatic ring that allows for the formation of a weak secondary hydrogen bond with N-H distances between

2.3-2.4 Å, which may offer minor stabilization effects. However, the energetic stabilization of this additional hydrogen bond is eclipsed by the large electron withdrawing character of the ortho-nitrogen groups and results in the weak electronic binding energy for this sub-class of adsorbates to the hydroxylated surface.

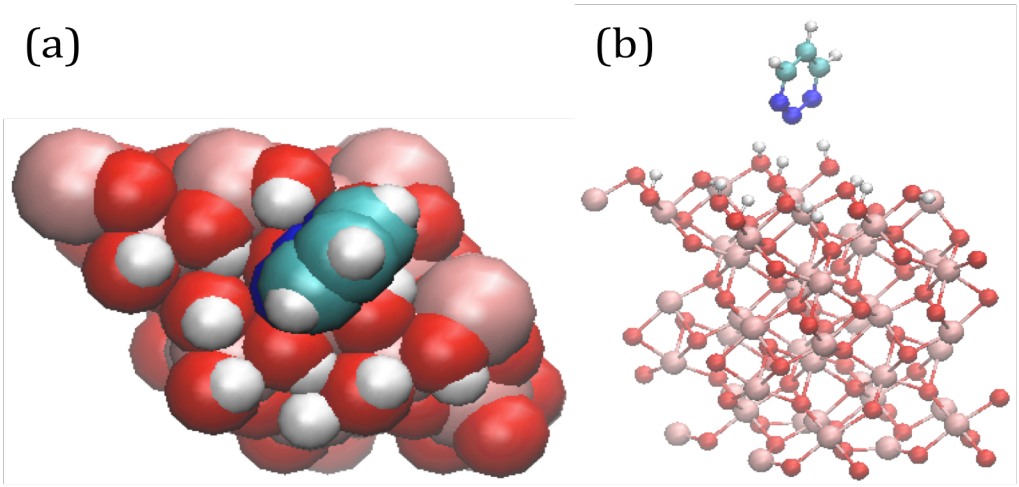

Figure 4.8. Lowest energy conformer for 1,2,3-triazine bound to the hydroxyl-terminated (0001) α-alumina surface through the 2-nitrogen group from a top-on (a) and side-on view (b).

Table 4.5. Binding energies and hydrogen bond lengths for the coordination of adsorbates with two ortho-amine groups to the hydroxyl-terminated alumina surface. For adsorbates containing more than one unique cyclic-amine group, the nitrogen atom bound to the surface is highlighted in red.

Adsorbate	Binding Energies	N-H Distances
1,2,3-Triazine	-7.8 kcal/mol	2.02 Å
1,2,3,4-Tetrazine	-6.4 kcal/mol	2.05 Å
1,2,3,5-Tetrazine	-6.0 kcal/mol	2.01 Å

The final class of adsorbates includes species with both nitrogen and methine groups in the ortho-position. These species bind to the hydroxyl-terminated surface such that the ortho-amine substituent points towards the nearest neighboring axial hydroxyl group and the ortho-methine group is placed in line with an open site created by a neighboring equatorial hydrogen atom (Figure 4.9). For this class of adsorbates, the bound nitrogen atom is predicted to form a hydrogen bond to the surface hydroxyl group with moderate N-H distances between 1.94-2.00 Å and electronic binding energies between 6.5 and 10.4 kcal/mol (Table 4.5). It should be noted that for this case, the length of the hydrogen bond is not directly related to the electronic binding energy, which may due to an energetic stabilization for complexes where the bound nitrogen group plays the role of a terminal substituent in a chain of adjacent nitrogen atoms. This stabilization helps offset the decreased hydrogen bonding capacity involved with the addition of nitrogen groups to the aromatic ring, resulting in 1,2,3-triazine possessing the most favorable binding energy, as it best balances cooperative nitrogen stabilization of the hydrogen bond and the electron withdrawing character of additional aromatic amine groups.

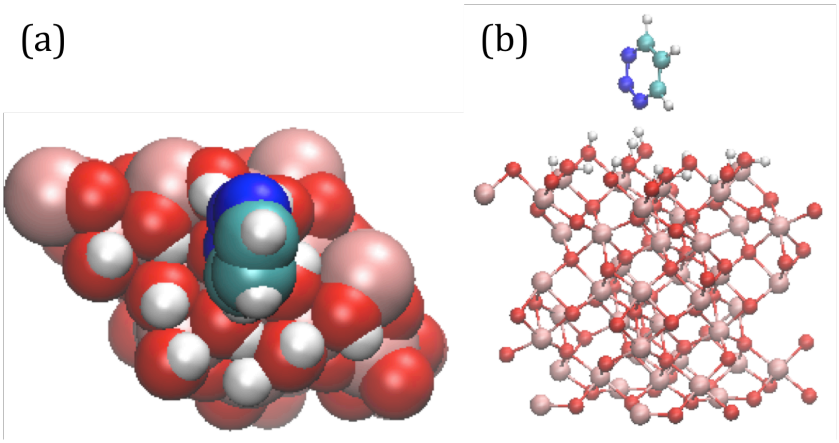

Figure 4.9. (Previous Page) The lowest energy conformer of 1,2,3-triazine bound to the hydroxyl-terminated (0001) α-alumina surface through the 1-nitrogen group from a top-on (a) and a side-on view (b).

Table 4.6. Electronic binding energies and hydrogen bond lengths for the coordination of adsorbates possessing both amine and methine groups at ortho-positions to the hydroxyl-terminated alumina surface. For adsorbates containing more than one unique cyclic-amine group, the nitrogen atom bound to the surface is highlighted in red.

Adsorbate	Binding Energies	N-H Distances
Pyridazine	-9.9 kcal/mol	1.96 Å
1,2,3-Triazine	-10.4 kcal/mol	1.98 Å
1,2,4-Triazine	-8.2 kcal/mol	1.96 Å
1,2,4-Triazine	-8.0 kcal/mol	1.97 Å
1,2,3,4-Tetrazine	-8.4 kcal/mol	1.98 Å
1,2,3,5-Tetrazine	-7.6 kcal/mol	2.00 Å
1,2,4,5-Tetrazine	-6.5 kcal/mol	1.96 Å

By comparing the binding energies of these three classes of adsorbates, we can assess the overall trends in the binding of nitrogen-rich aromatic groups to the "wet" alumina surface. Most important of which is that the dominant interaction with the surface proceeds through the formation of a single N-H hydrogen bond, with the orientation of the aromatic plane determined by the identity of the ortho-substituents. The strength of this hydrogen bond was found to be weakened by the addition of electron withdrawing nitrogen groups. However, improved coordination to the alumina surface was observed when the hydrogen bonding occurred at the terminal nitrogen-group of a chain of adjacent cyclic amines, indicating that this arrangement of nitrogen substituents

allows for a rearrangement of electron density that helps stabilize the formation of hydrogen bonds. However, certain binding conformations do allow for the formation of weak secondary hydrogen bonds and, due to the lack of covalent bonds involved in adsorbate binding to this surface, the use of molecular modeling techniques may provide insight into the complete range and strength of hydrogen bonding motifs allowed between the hydroxyl-terminated surface and these nitrogen-rich aromatic adsorbates in addition to lending insight about the impact of entropic terms on surface binding.

4.4. Conclusions

Comparison of the electronic binding energies for the adsorption of the molecules in our test set to the three surfaces examined here provides insight into the binding mechanisms of nitrogen-rich aromatic groups to aluminum containing surfaces (Table 4.7). For all of these surfaces the primary coordination of the adsorbate takes place through electron donation from an aromatic amine to an available electropositive group on the aluminum containing surface. For the aluminum metal and the "dry" α-alumina surface, this involves the formation of an Al-N σ-bond, which is weakened upon the inclusion of electron withdrawing aromatic amine substituents to the adsorbate. Additional coordination to the surface is provided by the inclusion of nitrogen groups at the ortho-position, which enables π-backbonding from the aluminum atom into the aromatic ring. For electron rich surfaces, this strengthens the coordination of electron poor aromatic rings to the aluminum atom found at the binding site, while for electron poor surfaces, the presence of ortho-nitrogen groups results in weak binding energies. In

natural systems, this indicates that nitrogen-rich adsorbates may undergo weaker surface binding, due to the dominance of electron poor alumina surfaces.

Table 4.7. Adsorption energies for all ten studied adsorbates onto the three possible aluminum containing surfaces. For adsorbates possessing more than one unique cyclic-amine group, the nitrogen atom bound to the surface is highlighted in red.

Adsorbate	Aluminum	Alumina	OH
Pyridine	-12.6	-36.7	-9.0
Pyridazine	-12.8	-30.0	-9.9
Pyrimidine	-9.5	-31.9	-7.5
Pyrazine	-9.7	-33.8	-7.6
1,2,3-Triazine	-9.8	-31.0	-10.4
1,2,3-Triazine	-12.4	-24.1	-7.8
1,2,4-Triazine	-13.3	-29.4	-8.2
1,2,4-Triazine	-12.2	-29.2	-8.0
1,2,4-Triazine	-8.1	-31.0	-6.4
1,3,5-Triazine	-7.6	-31.6	-6.9
1,2,3,4-Tetrazine	-12.7	-27.6	-8.4
1,2,3,4-Tetrazine	-12.9	-20.8	-6.4
1,2,3,5-Tetrazine	-11.0	-28.3	-7.6
1,2,3,5-Tetrazine	-16.4	-21.2	-6.0
1,2,3,5-Tetrazine	-11.6	-26.9	-5.7
1,2,4,5-Tetrazine	-15.4	-26.0	-6.5

However, slightly different trends are observed for the hydroxyl-terminated surface, which contains no surface aluminum atoms that can bind adsorbates. For this case, the nitrogen group undergoes hydrogen bonding to the surface hydroxyl groups, with the hydrogen-bond being weakened by the presence of electron-withdrawing substituents on the aromatic ring, though mild stabilization of this hydrogen bond is observed for adsorbates where surface binding takes place through the terminal group of a chain of adjacent nitrogen atoms, possibly through the stabilization of partial charges on the

aromatic ring. Though a complete molecular mechanics study of the interaction of adsorbates with multiple surface configurations would be recommended to exclude the possibility of weak secondary hydrogen bonds to the alumina surface producing an energetic favoring of this class of binding sites.

This work helps demonstrate the importance of knowing the nature of both the adsorbate and adsorption surface in order to enable the prediction of electronic binding energies for nitrogen-rich HECs. An electron rich surface prefers adsorbates that allow π-backbonding, while electron poor surfaces select against adsorbates with any form of electron withdrawing groups, and "wet" α-alumina surfaces prefer binding of adsorbates that can form strong hydrogen bonds. Though for all cases the identity of the ortho-groups plays the most significant role in determining the mode of coordination. However, this work shows that strong surface-binding is only predicted to occur for the coordination of molecules that contain no ortho-amine substituents onto a "dry" α-alumina surface.

References:

1) Cramer, C. J. *Essentials of Computational Chemistry: Theories and Models,* 2nd ed. John Wiley Sons, Chicheseter, **2004**.

2) Hartree, D. R. *Proc. Cambridge Phil. Soc.* **1928**, 24, 89-110.

3) Hartree, D. R. *Proc. Cambridge Phil. Soc.* **1928**, 24, 110-132.

4) Slater, J. C. *Phys. Rev.* **1928**, 32, 339-348.

5) Slater, J. C. *Phys Rev.* **1930**, 35, 210-211.

6) Rootham, C. C. J. *Rev. Mod. Phys.* **1951**, 23, 69-89.

7) Moller, C.; Plesset, M. S. *Phys Rev.* **1934**, 46, 618-622.

8) Peterson, G. A.; Bennett, A.; Tensfeldt, T. G. AlLahan, M. A.; Shirley, W. A.; Mantzaris, J. *J. Chem. Phys.* **1988**, 89, 4, 2193-2218.

9) Peterson, G. A.; Tansfeldt, T. G.; Montgomery, J. A. *J. Chem. Phys.* **1991**, 9, 6091-6101.

10) Ochterski, J. W.; Peterson, G. A.; Montgomery, J. A. *J. Chem. Phys.* **1996**, 104, 7, 2598-2619.

11) Hohenberg, P.; Kohn, W. *Phys. Rev.* **1964**, 136, B 864-871.

12) Kohn, W.; Sham, L. J. *Phys Rev.* **1965**, 140, A 1133-1138.

13) Langreth, D. C.; Mehl, M. J. *Phys. Rev. B* **1983**, 28, 1809-1834.

14) Perdew, J. P. *Phys. Rev. B* **1986**, 33, 8822-8824.

15) Lee, C.; Yang, W.; Parr, R. G. *Phys. Rev. B* **1988**, 37, 785-789.

16) Becke, A. D. *Phys. Rev. A* **1988**, 38, 3098-3100.

17) Becke, A. D. *J. Chem. Phys.* **1996**, 104, 1040-1046

18) Tao, J.; Perdew, J. P.; Staroverov, V. N.; Scuseria, G. E. *Phys. Rev. Lett.* **2003**, 91, 146401-146404.

19) Zhao, Y.; Truhlar, D. G. *J. Chem. Phys.* **2006**, 125, 194101-194118.

20) Gruning, M.; Gritsenko, O. V.; Baerends, E. J. *J. Phys. Chem. A* **2004**, 108, 4459-4469.

21) Becke, A. D. *J. Chem. Phys.* **1993**, 98, 1372-1377.

22) Becke, A. D. *J. Chem. Phys.* **1993**, 98, 5648-5652.

23) Adamo, C.; Barone, V. *J. Chem. Phys.* **1998**, 108, 664-675.

24) Lynch, B. J.; Fast, P. L.; Harris, M.; Truhlar, D. G. *J. Phys. Chem. A* **2000**, 104, 4811-4815.

25) Cramer, C. J.; Truhlar, D. G. *Phys. Chem. Chem. Phys.* **2009**, 11, 10757-10816.

26) Toulouse, J.; Colonna, F.; Savin, A. *Phys Rev. A* **2004**, 70, 062505-16.

27) Heyd, J.; Scuseria, G. E. *J. Chem. Phys.* **2004**, 120, 7274-7280.

28) Yanai, T.; Tew, D. P.; Handy, N. C. *Chem. Phys. Lett.* **2004**, 393, 51-57.

29) Gerber, I. C.; Angyan, J. G. *Chem. Phys. Lett.* **2005**, 415, 100-105.

30) Peverati, R.; Truhlar, D. G. *J. Phys. Chem. Lett.* **2011**, 2, 2810-2817.

31) Peverati, R.; Truhlar, D. G. *J. Phys. Chem. Lett.* **2012**, 3, 117-124.

32) Grimme, S. *J. Comp. Chem.* **2006**, 27, 1787-1799

33) Grimme, S.; Antony, J.; Ehrlich, S.; Krieg, H. *J. Chem. Phys.* **2010**, 132, 154104-19.

34) Hehre, W. J.; Radom, L.; Schleyer, Pv. R.; Pople, J. A. *Ab Initio Molecular Orbital Theory,* Wiley, New York, **1986**.

35) Hellmann, H. *J. Chem. Phys.* **1935**, 3, 61.

36) Lee, Y. S.; Ermler, W. C.; Pitzer, K. S. *J. Chem. Phys.* **1977**, 67, 5861-5876.

37) Slater, J. C. *Phys. Rev.* **1937**, 51, 846-851.

38) Phillips, J. C.; Kleinman, L. *Phys. Rev.* **1959**, 116, 287-294

39) Hamn, D. R.; Schluter, M.; Chiang, C. *Phys. Rev. Lett.* **1979**, 43, 194-197.

40) Vanderbilt, D. *Phys. Rev. B.* **1990**, 41, 7892-7895.

41) Miertus, S.; Scrocco, E.; Tomasi, J. *Chem. Phys.* **1981**, 55, 117-129.

42) Cossi, M.; Scalmani, G.; Rega, N.; Barone, V. *J. Chem. Phys.* **2002**, 117, 43-54

43) Marenich, A. V.; Cramer, C. J.; Truhlar, D. G. *J Phys. Chem. B* **2009**, 113, 6378-6396.

44) Chen, Z.; Meyer, T. J. *Angew. Chem. Int. Ed.* **2013**, *52*, 700-703.

45) Talmage, S. S.; Watson, A. P.; Hauschild, V.; Munro, N. B.; King, J. *Curr. Org. Chem.* **2007***, 11*, 285-298.

46) Munro, N. B.; Ambrose, K. R.; Watson, A. P. *Environ. Health Perspect.* **1994**, 102, 18-34.

47) Munro, N. B.; Talmage, S. S.; Griffin, G. D.; Waters, L. C.; Watson, A. P. King, J. F.; Hauschild, V. *Environ. Health Perspect.* **1999**, 107, 933-974.

48) Kim, K.; Tsay, O. G.; Atwood, D. A.; Churchill, D. G. *Chem. Rev.* **2011**, *111*, 5345-5403.

49) NRC *Review of Systemization of the Tooele Chemical Agent Disposal Facility;* National Acadamy Press: Washington, DC, 1996.

50) Pearson, G. S.; Magee, R. S. *Pure Appl. Chem.* **2002**, 74, 187-316.

51) Seckute, J.; Menke, J. L.; Emnett, R. J.; Patterson, E. V.; Cramer, C. J. *J. Org. Chem.* **2005**, *70*, 8649-8660.

52) Daniel, K. A.; Kopff, L. A.; Patterson, E. V. *J. Phys. Org. Chem.* **2008**, *21*, 321-328.

53) Yang, Y. C.; Szafraniec, L. L.; Beaudry, W. T.; Rohrbaugh, D. K. *J. Am. Chem. Soc.* **1990***, 112*, 6621-6627.

54) Epstein, J.; Callahan, J. J.; Bauer, V. E. *Phosphorus* **1974**, 4, 157-163.

55) Debruin, K. E.; Tang, C. W.; Johnson, D. M.; Wilde, R. L. *J. Am. Chem. Soc.* **1989**, 111, 5871-5879.

56) Yang, Y. C.; Barker, J. A.; Ward, J. R. *Chem. Rev.* **1992**, 92, 1729-1743.

57) Yang, Y. C.; Berg, F. J.; Szafraniec, L. L.; Beaudry, W. T.; Bunton, C. A.; Kumar, A. *J. Chem. Soc., Perkin Trans.* **1997**, 2, 607-613.

58) Kuo, L. Y.; Blum, A. P.; Sabat, M. *Inorg. Chem.* **2005**, 44, 5537-5541.

59) Melnychuck, S. A.; Neverov, A. A.; Brown, R. S. *Angew. Chem. Int. Ed.* **2006,** 45, 1767-1770.

60) Kuo, L. Y.; Adint, T. T.; Akagi, A. E.; Zakharob, L. *Organometallics* **2008**, 27, 2560-2564.

61) Andrea, T.; Neverov, A. A.; Brown, R. S. *Ind. Eng. Chem. Res.* **2010**, 49, 7027-7033.

62) Epstein, J.; Bauer, V. E.; Saxe, M.; Demek, M. M. *J. Am. Chem. Soc.* **1956**, 78, 4068-4071.

63) Wagner, G. W.; Yang, Y. C. *Ind. Eng. Chem. Res.* **2002**, 41, 1925-1928.

64) Raber, E.; McGuire, R. *J. Hazard. Mater.* **2002**, 93, 339-352.

65) Ekerdt, J. G.; Klabunde, K. J.; Shapley, J. R.; White, J. M.; Yates, J. T., Jr. *J. Phys. Chem.* **1988**, *92*, 6182.

66) Henderson, M. A.; White, J. M. *J. Am. Chem. Soc.* **1988**, 110, 6939-6947.

67) Wagner, G. W.; Bartram, P. W. *Langmuir* **1999**, 8113-8118.

68) Wagner, G. W.; Bartram, P. W.; Koper, O.; Klabunde, K. J. *J. Phys. Chem. B* **1999**, 3225-3228.

69) Wagner, G. W.; Koper, O. B.; Lucas, E.; Decker, S.; Klabunde, K. J. *J. Phys. Chem. B* **2000**, 104, 5118-5123.

70) Wagner, G. W.; Procell, L. R.; O'Connor, R. J.; Munavalli, S.; Carnes, C. L.; Kapoor, P. N.; Klabunde, K. J. *J Am. Chem. Soc.* **2001**, 123, 1636-1644.

71) Margot, J. M.; Ardouin, T.; Istin, M.; Vandais, A.; Noel, J. P.; Rima, G.; Sagte, J.; Pradel, C.; Sentenac-Roumanou, H.; Lion, C. *Arch. Toxicol.* **1993**, 67, 66-71.

72) Vayron, P. Renard, P. Y.; Valleix, A.; Mioskowski, C. *Chem. Eur. J.* **2000**, 6, 1050-1063.

73) Hill, C. M.; Li, W.; Thoden, J. B.; Holden, H. M.; Raushel, F. M. *J. Am. Chem. Soc.* **2003***, 125*, 8990-8991

74) Amitai, G.; Adani, R.; Hershkovitz, M.; Bel, P.; Rabinovitz, I.; Meshulam, H. *J. Appl. Toxicol.* **2003***, 23*, 225-233.

75) Briseño-Roa, L.; Hill, J.; Notman, S.; Sellers, D.; Smith, A. P.; Timperley, C. M.; Wetherell, J.; Williams, N. H.; Williams, G. R.; Fersht, A. R.; Griffiths, A. D. *J. Med. Chem.* **2006**, 49 246, 255.

76) Hamza, A.; Schubert, G.; Soos, T.; Papal, I. *J. Am. Chem. Soc.* **2006**, *128*, 13151-13160.

77) Liu, T.; Li, R.; Chai, Q.; Long, J.; Li, B.; Wu, Y.; Ding, L.; Chen. Y. *Chem. Eur. J.* **2007**, *13*, 319-327.

78) Almasi, D.; Alonso, D. A.; Gomez, E.; Najera, C. *J. Org. Chem.* **2009**, *74*, 6163-6168.

79) Zhao, Y.; Truhlar, D. G. *Theor. Chem. Acc.* **2008**, *120*, 215-241.

80) Hehre, W. J.; Radom, L.; Schleyer, P. V. R.; Pople, J. A. *Ab Initio Molecular Orbital Theory;* Wiley: New York, 1986.

81) Marenich, A. V.; Cramer, C. J.; Truhlar, D. G. *J. Phys. Chem. B* **2009**, *113*, 6378-6396.

82) Grimme, S. *J. Chem. Phys.* **2003**, *118*, 9096-9102.

83) Montgomery, J. A.; Frisch, M. J. *J. Chem. Phys.* **1999**, *110*, 2822-2827.

84) Frisch, M. J.; Trucks, G. W.; Schlegel, H. B.; Scuseria, G. E.; Robb, M. A.; Cheeseman, J. R.; Scalmani, G.; Barone, V.; Mennucci, B.; Petersson, G. A.; Nakatsuji, H.; Caricato, M.; Li, X.; Hratchian, H. P.; Izmaylov, A. F.; Bloino, J.; Zheng, G.; Sonnenberg, J. L.; Hada, M.; Ehara, M.; Toyota, K.; Fukuda, R.; Hasegawa, J.; Ishida, M.; Nakajima, T.; Honda, Y.; Kitao, O.; Nakai, H.; Vreven, T.; Montgomery, J. A.; Peralta, J. E.; Ogliaro, F.; Bearpark, M.; Heyd, J. J.; Brothers, E.; Kudin, K. N.; Staroverov, V. N.; Kobayashi, R.; Normand, J.; Raghavachari, K.; Rendell, A.; Burant, J. C.; Iyengar, S. S.; Tomasi, J.; Cossi, M.; Rega, N.; Millam, J. M.; Klene, M.; Knox, J. E.; Cross, J. B.; Bakken, V.; Adamo,

C.; Jaramillo, J.; Gomperts, R.; Stratmann, R. E.; Yazyev, O.; Austin, A. J.; Cammi, R.; Pomelli, C.; Ochterski, J. W.; Martin, R. L.; Morokuma, K.; Zakrzewski, V. G.; Voth, G. A.; Salvador, P.; Dannenberg, J. J.; Dapprich, S.; Daniels, A. D.; Farkas, Ö.; Foresman, J. B.; Ortiz, J. V.; Cioslowski, J.; Fox, D. J. *Gaussian 09, Revision A.02*; Gaussian, Inc.: Wallingford, CT, 2010.

85) Cramer, C. J. *J. Mol. Struct. (Theochem)* **1996**, *370*, 135-146.

86) Tinker, L. L.; McDaniel, N. D.; Bernhard, S. *J. Mater. Chem.* **2009**, *19*, 3328-3337.

87) Dau, H.; Limberg, C.; Reier, T.; Risch, M.; Roggan, S.; Strasser, P. *Chemcatchem* **2010**, *2*, 724-761.

88) Yamazaki, H.; Shouji, A.; Kajita, M.; Yagi, M. *Coord. Chem. Rev.* **2010**, *254*, 2483-2491.

89) Llobet, A.; Meyer, F. *Angew. Chem. Int. Ed.* **2011**, *50*, A30-A33.

90) Fukuzumi, S.; Kishi, T.; Kotani, H.; Lee, Y.-M.; Nam, W. *Nat Chem* **2011**, *3*, 38-41.

91) Herrero, C.; Quaranta, A.; Leibl, W.; Rutherford, A. W.; Aukauloo, A. *Energy Environ. Sci.* **2011**, *4*, 2353-2365.

92) Gust, D.; Moore, T. A.; Moore, A. L. *Faraday Discuss.* **2012**, *155*, 9-26.

93) Joya, K. S.; Valles-Pardo, J. L.; Joya, Y. F.; Eisenmayer, T.; Thomas, B.; Buda, F.; de Groot, H. J. M. *Chempluschem* **2013**, *78*, 35-47.

94) Swierk, J. R.; Mallouk, T. E. *Chem. Soc. Rev.* **2013**, *42*, 2357-2387.

95) McDaniel, N. D.; Coughlin, F. J.; Tinker, L. L.; Bernhard, S. *J. Am. Chem. Soc.* **2007**, *130*, 210-217.

96) Blakemore, J. D.; Schley, N. D.; Balcells, D.; Hull, J. F.; Olack, G. W.; Incarvito, C. D.; Eisenstein, O.; Brudvig, G. W.; Crabtree, R. H. *J. Am. Chem. Soc.* **2010**, *132*, 16017-16029.

97) Vilella, L.; Vidossich, P.; Balcells, D.; Lledos, A. *Dalton Trans.* **2011**, *40*, 11241-11247.

98) Hong, D. C.; Murakami, M.; Yamada, Y.; Fukuzumi, S. *Energy Environ. Sci.* **2012**, *5*, 5708-5716.

99) DePasquale, J.; Nieto, I.; Reuther, L. E.; Herbst-Gervasoni, C. J.; Paul, J. J.; Mochalin, V.; Zeller, M.; Thomas, C. M.; Addison, A. W.; Papish, E. T. *Inorg. Chem.* **2013**, *52*, 9175-9183.

100) Gersten, S. W.; Samuels, G. J.; Meyer, T. J. *J. Am. Chem. Soc.* **1982**, *104*, 4029-4030.

101) Yang, X.; Baik, M. H. *J. Am. Chem. Soc.* **2008**, *130*, 16231-16240.

102) Bozoglian, F.; Romain, S.; Ertem, M. Z.; Todorova, T. K.; Sens, C.; Mola, J.; Rodriguez, M.; Romero, I.; Benet-Buchholz, J.; Fontrodona, X.; Cramer, C. J.; Gagliardi, L.; Llobet, A. *J. Am. Chem. Soc.* **2009**, *131*, 15176-15187.

103) Sala, X.; Romero, I.; Rodriguez, M.; Escriche, L.; Llobet, A. *Angew. Chem. Int. Ed.* **2009**, *48*, 2842-2852.

104) Wasylenko, D. J.; Ganesamoorthy, C.; Henderson, M. A.; Koivisto, B. D.; Osthoff, H. D.; Berlinguette, C. P. *J. Am. Chem. Soc.* **2010**, *132*, 16094-16106.

105) Li, X. C.; Chen, G. J.; Schinzel, S.; Siegbahn, P. E. M. *Dalton Trans.* **2011**, *40*, 11296-11307.

106) Ghosh, S.; Baik, M. H. *Inorg. Chem.* **2011**, *50*, 5946-5957.

107) Duan, L. L.; Araujo, C. M.; Ahlquist, M. S. G.; Sun, L. C. *Proc. Natl. Acad. Sci., USA* **2012**, *109*, 15584-15588.

108) Wada, T.; Ohtsu, H.; Tanaka, K. *Chem. Eur. J.* **2012**, *18*, 2374-2381.

109) Kaveevivitchai, N.; Zong, R. F.; Tseng, H. W.; Chitta, R.; Thummel, R. P. *Inorg. Chem.* **2012**, *51*, 2930-2939.

110) Ghosh, S.; Baik, M.-H. *Angew. Chem. Int. Ed.* **2012**, *51*, 1221-1224.

111) Kimoto, A.; Yamauchi, K.; Yoshida, M.; Masaoka, S.; Sakai, K. *Chem. Commun.* **2012**, *48*, 239-241.

112) Kang, R.; Yao, J.; Chen, H. *J. Chem. Theory Comput.* **2013**, *9*, 1872-1879.

113) Hirahara, M.; Ertem, M. Z.; Komi, M.; Yamazaki, H.; Cramer, C. J.; Yagi, M. *Inorg. Chem.* **2013**, *52*, 6354-6364.

114) Vaquer, L.; Miro, P.; Sala, X.; Bozoglian, F.; Masllorens, E.; Benet-Buchholz, J.; Fontrodona, X.; Parella, T.; Romero, I.; Roglans, A.; Rodriguez, M.; Bo, C.; Llobet, A. *Chempluschem* **2013**, *78*, 235-243.

115) Saveant, J. M. *Chem. Rev.* **2008**, *108*, 2348-2378.

116) Cao, R.; Lai, W. Z.; Du, P. W. *Energy Environ. Sci.* **2012**, *5*, 8134-8157.

117) Singh, A.; Spiccia, L. *Coord. Chem. Rev.* **2013**, *257*, 2607-2622.

118) Cady, C. W.; Crabtree, R. H.; Brudvig, G. W. *Coord. Chem. Rev.* **2008**, *252*, 444-455.

119) Herrero, C.; Quaranta, A.; Protti, S.; Leibl, W.; Rutherford, A. W.; Fallahpour, R.; Charlot, M. F.; Aukauloo, A. *Chem. Asian J.* **2011**, *6*, 1335-1339.

120) Karlsson, E. A.; Lee, B. L.; Akermark, T.; Johnston, E. V.; Karkas, M. D.; Sun, J. L.; Hansson, O.; Backvall, J. E.; Akermark, B. *Angew. Chem. Int. Ed.* **2011**, *50*, 11715-11718.

121) Siegbahn, P. E. M.; Blomberg, M. R. A. *J. Chem. Theory Comput.* **2014**, *10*, 268-272.

122) Yin, Q.; Tan, J. M.; Besson, C.; Geletii, Y. V.; Musaev, D. G.; Kuznetsov, A. E.; Luo, Z.; Hardcastle, K. I.; Hill, C. L. *Science* **2010**, *328*, 342-345.

123) Artero, V.; Chavarot-Kerlidou, M.; Fontecave, M. *Angew. Chem. Int. Ed.* **2011**, *50*, 7238-7266.

124) Dogutan, D. K.; McGuire, R.; Nocera, D. G. *J. Am. Chem. Soc.* **2011**, *133*, 9178-9180.

125) Gerken, J. B.; McAlpin, J. G.; Chen, J. Y. C.; Rigsby, M. L.; Casey, W. H.; Britt, R. D.; Stahl, S. S. *J. Am. Chem. Soc.* **2011**, *133*, 14431-14442.

126) Wang, L. P.; Van Voorhis, T. *J. Phys. Chem. Lett.* **2011**, *2*, 2200-2204.

127) Wasylenko, D. J.; Ganesamoorthy, C.; Borau-Garcia, J.; Berlinguette, C. P. *Chem. Commun.* **2011**, *47*, 4249-4251.

128) Rigsby, M. L.; Mandal, S.; Nam, W.; Spencer, L. C.; Llobet, A.; Stahl, S. S. *Chem. Sci.* **2012**, *3*, 3058-3062.

129) Ertem, M. Z.; Cramer, C. J. *Dalton Trans.* **2012**, *41*, 12213-12219.

130) Goberna-Ferron, S.; Vigara, L.; Soriano-Lopez, J.; Galan-Mascaros, J. R. *Inorg. Chem.* **2012**, *51*, 11707-11715.

131) Hong, D.; Jung, J.; Park, J.; Yamada, Y.; Suenobu, T.; Lee, Y. M.; Nam, W.; Fukuzumi, S. *Energy Environ. Sci.* **2012**, *5*, 7606-7616.

132) La Ganga, G.; Puntoriero, F.; Campagna, S.; Bazzan, I.; Berardi, S.; Bonchio, M.; Sartorel, A.; Natali, M.; Scandola, F. *Faraday Discuss.* **2012**, *155*, 177-190.

133) Pizzolato, E.; Natali, M.; Posocco, B.; Lopez, A. M.; Bazzan, I.; Di Valentin, M.; Galloni, P.; Conte, V.; Bonchio, M.; Scandola, F.; Sartorel, A. *Chem. Commun.* **2013**, *49*, 9941-9943.

134) Li, X.; Siegbahn, P. E. M. *J. Am. Chem. Soc.* **2013**.

135) Kwapien, K.; Piccinin, S.; Fabris, S. *J. Phys. Chem. Lett.* **2013**, *4*, 4223-4230.

136) Lei, H. T.; Han, A.; Li, F. W.; Zhang, M. N.; Han, Y. Z.; Du, P. W.; Lai, W. Z.; Cao, R. *Phys. Chem. Chem. Phys.* **2014**, *16*, 1883-1893.

137) Ellis, W. C.; McDaniel, N. D.; Bernhard, S.; Collins, T. J. *J. Am. Chem. Soc.* **2010**, *132*, 10990-10991.

138) Fillol, J. L.; Codolà, Z.; Garcia-Bosch, I.; Gómez, L.; Pla, J. J.; Costas, M. *Nat Chem* **2011**, *3*, 807-813.

139) Ertem, M. Z.; Gagliardi, L.; Cramer, C. J. *Chem. Sci.* **2012**, *3*, 1293-1299.

140) Hoffert, W. A.; Mock, M. T.; Appel, A. M.; Yang, J. Y. *Eur. J. Inorg. Chem.* **2013**, *2013*, 3846-3857.

141) Hong, D.; Mandal, S.; Yamada, Y.; Lee, Y. M.; Nam, W.; Llobet, A.; Fukuzumi, S. *Inorg. Chem.* **2013**, *52*, 9522-9531.

142) Liao, R.-Z.; Li, X.-C.; Siegbahn, P. E. M. *Eur. J. Inorg. Chem.* **2014**, *2014*, 728-741.

143) Barnett, S. M.; Goldberg, K. I.; Mayer, J. M. *Nature Chemistry* **2012**, *4*, 498-502.

144) Zhang, M.-T.; Chen, Z.; Kang, P.; Meyer, T. J. *J. Am. Chem. Soc.* **2013**, *135*, 2048-2051.

145) Zhang, T.; Wang, C.; Liu, S. B.; Wang, J. L.; Lin, W. B. *J. Am. Chem. Soc.* **2014**, *136*, 273-281.

146) Peverati, R.; Truhlar, D. G. *J. Phys. Chem. Lett* **2012**, 3, 117-124.

147) Reiher, M.; Salomon, O.; Hess, B. A. *Theor. Chem. Acc.* **2001,** 107, 48-55.

148) Stoll, H.; Metz, B.; Dolg, M. *J. Comp. Chem.* **2002**, *23*, 767-778.

149) Bryantsev, V. S.; Diallo, M. S.; Goddard III, W. A. *J. Phys. Chem. B* **2008**, 112, 9709-9719.

150) Tissandier, M. D.; Cowen, K. A.; Feng, W. Y.; Gundlach, E.; Cohen, M. H.; Earhart, A. D.; Coe, J. V.; Tuttle, T. R. Jr. *J. Phys. Chem. A* **1998**, 102, 7787-7794.

151) Camaioni, D. M.; Schwerdtferger, C. A. Comment on *J. Phys. Chem. A* **2005**, 109, 10795-10797.

152) Kelly, C. P.; Cramer, C. J.; Truhlar, D. G. *J. Phys. Chem. A* **2006**, 110, 2493-2499.

153) Sadlej-Sosnowska, N. *Theor. Chem. Acc.* **2007**, 118, 281-293.

154) Winget, P.; Cramer, C. J.; Truhlar, D. G. *Theor. Chem. Acc.* **2004**, 112, 217-227.

155) Lewis, A.; Bumpus, J. A.; Truhlar, D. G.; Cramer, C. J. *J. Chem. Ed.* **2004**, 81, 596-604. (erratum **2007**, 84, 934)

156) Kelly, C. P.; Cramer, C. J.; Truhlar, D. G. *J. Phys. Chem. B* **2007**, 111, 408-422.

157) Schosseler, P. M.; Wehrli, B.; Schweiger, A. *Inorg. Chem.* **1997,** 36 4490-4499.

158) Siegbahn, P. E. M.; Blomberg, M. R. A. *J. Chem. Theory Comput.* **2014,** 10, 268-272.

159) Luo, S.; Averkiev, B.; Yang, K. R.; Xu, X.; Truhlar D. G. *J. Chem. Theor. Comput.* **2014,** 10, 102-121.

160) Binstead, R. A.; Chronister, C. W.; Ni, J.; Hartshorn, C. M.; Meyer, T. J. *J. Am. Chem Soc.* **2000,** *122,* 8464-8473.

161) Concepcion, J. J.; Jurss, J. W.; Templeton, J. L.; Meyer, T. J. *J. Am. Chem. Soc.* **2008,** *130,* 16462-16463.

162) Chen, Z.; Concepcion, J. J.; Hu X.; Yang, W.; Hoertz, P. G.; Meyer, T. J. *Proc. Natl. Acad. Sci.* **2010,** *107,* 7225-7229.

163) Pennington, J. C.; Brannon, J. M. *Thermochim. Acta* **2002**, 384, 163-172

164) Alavi, G.; Chung, M.; Lichwa, J.; D'Alessio, M.; Ray, C. *J. Hazard. Mater.* **2011**, 185, 1600-1604.

165) Lin, K. S.; Dehvari, K.; Hsien, M. J.; Hsu, P. J.; Kuo, H. *Propellants Explos. Pyrotech.* **2013**, 38, 786-790.

166) Panz, K.; Miksch, K. *J. Environ. Manag.* **2012**, 113, 85-92.

167) Mason, S. E.; Iceman, C. R.; Trainor, T. P.; Chaka, A. M. *Physics Procedia* **2010**, 4, 67-83.

168) *Principles and Applications of Inorganic Geo-chemistry;* Fauer, G. MacMillan, New York, 1991.

169) Sposito, G. *The Environmental Chemistry of Aluminum;* 2nd Ed; CRC Press, Inc. 1996.

170) Henrich, V. E., Cox, P. A. *The surface science of metal oxides*; Cambridge University Press: New York, 1994.

171) Muller, J.; Shierling, M.; Zimmermann, E.; Neushutz, D. *Surf. Coat. Technol.* **1999**, 120-121, 16.

172) Karadge, M.; Zhao, X.; Preuss, M.; Xiao, P. *Scr. Mater.* **2006**, 54, 639-644.

173) Bartholomew, C. H.; Farruto, R. J. *Fundamentals of Industrial Catalytic Processes;* Hoboken, Wiley, 2006.

174) Henry, C. R. *Surf. Sci. Rep.* **1998**, 31, 231-325.

175) Hellman, A.; Gronbeck, H. *J. Phys. Chem. C* **2009**, 113, 3674-3682.

176) Mason, S. E.; Iceman, C. R.; Tanwar, K.; Trainor, T. P.; Chaka, A. M. *J. Phys. Chem. C.* **2009**, 113, 2159-2170.

177) Ram. S; Rana, S. *Curr. Sci.* **1999**, 77, 1530-1536.

178) Reichel, F.; Jeurgens, L. P. H.; Richter, G.; Aken, P. A. V.; Mittemeijer, E. J. *Acta. Mater.* **2007**, 55, 6027-6037.

179) Reichel, F.; Jeurgens, L. P. H.; Mittemeijer, E. J. *Surf. Inter. Anal.* **2008**, 40, 281-284.

180) Brindley, W. J.; Miller, R. A. *Surf. Coat. Technol.* **1990**, 43/44, 446-457.

181) Rabiei, A.; Evans, A. G.; *Acta Mater.* **2000**, 48, 3963-3976.

182) Padture, N. P.; Gell, M.; Jordan, E. H. *Science* **2002**, 296, 280-284.

183) Nakamura, S.; Senoh, M.; Mukai, T. *Appli. Phys. Lett.* **1993**, 62, 2390-2392.

184) Minahan, D. M.; Hoflund, G. B.; Epling, W. S.; Schoenfeld, D. W. *J. Catal.* **1997**, 168, 393-399.

185) Lyubovsky, M.; Pfefferle, L. *Catal. Today* **1999**, 47, 29-44.

186) Choi, J. H.; Kim, D. Y.; Hockey, B. J.; Widerhorn, S. M.; Handwerker, C. A.; Blendell, J. E.; Carter, W. C.; Roosen, A. R. *J. Am. Ceram. Soc.* **1997,** 80, 62-68.

187) Marmier, J.; Parker, S. C. *Phys. Rev. B* **2004**, 69, 115409.

188) Ahn, J.; Rabalais, J. W. *Surf. Sci.* **1997,** 388, 121-131.

189) Blonski, S.; Garofalini, S. H. *Surf. Sci.* **1993**, 295, 1, 263-274.

190) Suzuki, T.; Hishita, S.; Oyoshi, K.; Souda, R. *Surf. Sci.* **1999**, 437, 289-298.

191) Soares, E. A; Van Hove, M. A.; Walters, C. F.; McCarty, K. F. *Phys. Rev. B.* **2002,** 65, 195405.

192) Eng, P. J.; Trainor, T. P.; Brown, G. E. Jr.; Waychunas, G. A.; Newville, M. A.; Sutton, S. R.; Rivers, M. L. *Science* **2000**, 288, 1029-1033.

193) Hass, F. C.; Schneider, W. F.; Curioni, A.; Andreoni, W. *Science* **1998**, 282, 265-268.

194) Liu, P.; Kendelewicz, T.; Brown, G. E. Jr.; Nelson, E. J.; Chambers, S. A. *Surf. Sci.* **1998**, 417, 53-65.

195) Singh, R. P.; Verma, R. D.; Meshri, D. T.; Shreeve, J. M. *Angew. Chem. Int. Ed.* **2006**, 45, 3584.

196) Klapotke, T. M.; Steinhauser, G. *Angew. Chem. Int. Ed.* **2008**, 47, 3330-3347.

197) Tan, B.; Huang, M.; Huang, H.; Long, X.; Li, J.; Nie, F.; Huang, J. *Propellants Explos. Pyrotech.* **2013**, 38, 372-378.

198) Kreese, G.; Hafner*, J. Phys. Rev. B.* **1993,** 47, 558-561.

199) Kreese, G.; Furthmuller, J. *Phys. Rev. B* **1996,** 54, 11169-11186.

200) Kreese, G.; Furthmuller, J. *Comput. Mater. Sci.* **1996,** 6, 15-50.

201) Perdew, J. P., Burke, K.; Ernzerhof, M. *Phys. Rev. Lett.* **1996,** 77, 3865-3868.

202) Kreese, G.; Hafner, J. *J. Phys.; Condens. Matter* **1994**, 6, 8245-8258.

203) Blöch, P. E. *Phys. Rev. B.* **1994,** 50, 17953-17979.

204) Kresse, G.; Joubert, D. *Phys. Rev. B.* **1999,** 59, 1758-1775.

205) Kurita, T. Uchida, K.; Oshiyama, A. *Phys Rev. B.* **2010**, 82, 155319.

206) Newnham, R. E.; DeHann, Y. M. *Kristallogr.* **1962,** 117, 235-237.

207) Tepesch, P. D.; Quong, A. A. *Phys. Stat. Sol. (B)* **2000**, 217, 377-387.

208) Lodziana, Z.; Norskov, J. K. *J. Chem. Phys.* **2001**, 115, 11261-11267

209) Hinnemann, B.; Carter, E. A. *J. Phys. Chem. C* **2007,** 111, 7105-7126.

210) Fernández, E. M.; Eglitis, R. I.; Borstel, G.; Balbás, L. C. *Comp. Mat. Sci.* **2007,** 39, 587-592.

211) Wallin, E. Anderson, J. M.; Münger, E. P.; Chirita, V.; Helmersson, U. *Phys. Rev. B.* **2006,** 74, 125409.

212) Rohmann, C.; Metson, J. B.; Idriss, H. *Surf. Sci.* **2011,** 605, 1694-1703.

213) Gautier-Soyer, M.; Jollet, F.; Noguera, C. *Surf. Sci.* **1996**, 352-354, 755-759.

214) Vedozzi, C.; Jennison, D. R.; Schultz, P. A.; Sears, M. P. *Phys. Rev. Lett.* **1999**, 82, 799-803.

215) Jarvis, E. A. A.; Carter, E. A. *J. Phys. Chem. B* **2001**, 105, 4045-4052.

216) Ranea, V. A.; Schneider, W.; Carmichael, I. *Surf. Sci.* **2008**, 602, 268-275.

217) Borck, O.; Schroder, E. *J. Phys. Condens. Matter* **2006**, 18, 1-12

218) Xiao, L.; Schneider, W. F. *Surf. Sci.* **2008**, 602, 3445-3453.